Fall 2013

Numerical Techniques for the Noninvasive Assessment of Material Properties and Stresses in Soft Biomaterials

Kent David Butz
Purdue University

PURDUE UNIVERSITY
GRADUATE SCHOOL
Thesis/Dissertation Acceptance

This is to certify that the thesis/dissertation prepared

By Kent D. Butz

Entitled
NUMERICAL TECHNIQUES FOR THE NONINVASIVE ASSESSMENT OF MATERIAL
PROPERTIES AND STRESSES IN SOFT BIOMATERIALS

For the degree of   Doctor of Philosophy

Is approved by the final examining committee:

Eric A. Nauman
                    Chair

Corey P. Neu

Ganesh Subbarayan-Shastri

Thomas M. Talavage

To the best of my knowledge and as understood by the student in the *Research Integrity and Copyright Disclaimer (Graduate School Form 20)*, this thesis/dissertation adheres to the provisions of Purdue University's "Policy on Integrity in Research" and the use of copyrighted material.

Approved by Major Professor(s): Eric A. Nauman _____

_____

Approved by: David C. Anderson   11/25/2013
                    Head of the Graduate Program   Date

NUMERICAL TECHNIQUES FOR THE NONINVASIVE ASSESSMENT OF
MATERIAL PROPERTIES AND STRESSES IN SOFT BIOMATERIALS

A Dissertation

Submitted to the Faculty

of

Purdue University

by

Kent D. Butz

In Partial Fulfillment of the

Requirements for the Degree

of

Doctor of Philosophy

December 2013

Purdue University

West Lafayette, Indiana

ACKNOWLEDGEMENTS

TABLE OF CONTENTS

LIST OF TABLES

LIST OF FIGURES

ABSTRACT

Butz, Kent D. Ph.D., Purdue University, December 2013. Numerical Techniques for the Noninvasive Assessment of Material Properties and Stresses in Soft Biomaterials. Major Professor: Dr. Eric A. Nauman, School of Mechanical Engineering.

The noninvasive measurement of finite displacements and strains in biomaterials by magnetic resonance imaging (MRI) may be shown to enable mathematical estimates of stress distributions and material properties within structures of the body such as articular cartilage or the intervertebral disc. Such methods will allow for non-contact and patient-specific modeling in a manner not currently possible with traditional mechanical testing or finite element techniques. Therefore, the objective of this thesis was to develop computational methods incorporating imaging-based measures of deformation, composition, and local microstructure to permit nondestructive analysis of a range of complex biomechanical systems.

Finite strain-based models were developed and applied towards the analysis of several biomaterial systems of increasing material complexity. First, a model for the analysis of a homogeneous, single material system was created and applied to juvenile porcine cartilage for both linear and nonlinear material assumptions under plane stress conditions. Through this study, the viability of estimating stresses within a homogeneous material system solely from MRI-based displacement and strain measures could be established. The model was then expanded to encompass single-plane, multi-region structures and applied towards the analysis of regional stresses within a rabbit intervertebral disc degeneration model. This model incorporated imaging-based methods to estimate heterogeneous properties within the disc structure based upon local biochemical composition, and showed that the degeneration state of a tissue system could effectively

be visualized through the use of finite strain-based modeling. A multi-constituent mixture-based material model was next implemented in the analysis of agarose gel constructs. Material parameter estimates from this model were found to agree with those determined by an unconfined compression validation model, establishing physical relevance of noninvasive parameter estimates produced by the models. Finally, the mixture-based material model was applied towards an *in situ* analysis of the human intervertebral disc.

The models implemented here are the first such applications to use MRI-based measures of deformation, composition, and local microstructure to provide a nondestructive, finite strain-based method of characterizing stress and material properties in cartilage and intervertebral discs during applied loading.

CHAPTER 1. INTRODUCTION

Characterization of stress and strain patterns in load-bearing tissues such as articular cartilage or intervertebral discs is key to functionally evaluate the progression of tissue degeneration and treatment strategies for diseases such as osteoarthritis, a disease affecting 27 million people in the United States [1]. Moreover, knowledge of the structure-function relationships in soft tissue provides a more comprehensive understanding of tissue integrity during degeneration and repair. By characterizing the properties of articular joint tissues and stress fields arising from applied loads, it may be further possible to predict failure or identify early markers of disease long before the joint otherwise shows signs of deterioration or declines in performance [2, 3].

In the field of biomechanics, computational models are a powerful tool with which to evaluate and predict physical phenomena that cannot otherwise be directly observed. Such models commonly rely upon physical testing of material properties for the various constituents of the system of interest in order to provide a means of calibrating or verifying the predictions of the model [4-6]. While these methods have contributed significantly towards the understanding of general mechanical characteristics of a wide variety of biomaterials, such information does not necessarily describe patient-specific behavior. Maturity, environment, degeneration, and disease are just some of the factors that may influence the characteristics of tissue from one individual to the next [7, 8].

Currently there is a significant gap in the ability to fully and noninvasively characterize the mechanical response and material properties of tissue *in vivo*. Therefore, the objective of this work is to develop a noninvasive means for characterizing stresses and material properties in a variety of biological tissue types subject to degeneration, such as articular cartilage and intervertebral discs. Towards this goal, MRI-based computational

techniques are proposed in this work such that material properties and mechanical stresses may be accurately estimated within any biomaterial for which displacements are directly measured via MRI when subjected to known loading conditions. A computational framework was developed by addressing four specific aims:

1. <u>To establish and validate a method for estimating stresses and material properties for biological structures consisting of a single homogeneous material.</u> This model will be applied towards the analysis of juvenile porcine knee cartilage using strain fields obtained via displacement-encoded MRI [9]. An optimal material model will be identified and the computational model will be verified using strain and stress fields generated by finite element simulation.

2. <u>To develop a multi-material model for biological systems with heterogeneous and anisotropic material properties.</u> This model will be applied towards the analysis of rabbit intervertebral discs to determine regional stresses and material properties that arise within the nucleus pulposus and annulus fibrosus during axial compression.

3. <u>To incorporate and validate mixture theory material models in the context of noninvasive biomaterial analysis.</u> Application of the model will be the analysis of agarose gels of known composition. Properties of the agarose gels will be experimentally determined and used as verification of the parameter estimates computed by the models.

4. <u>To apply a mixture theory-based model to the analysis of human intervertebral discs.</u> This model will describe the complex behavior of the disc under axial loading conditions, including region-dependent properties and the interactions between both solid and fluid constituents within the system. Displacement and diffusion data obtained via MRI for human intervertebral disc samples will be used as inputs for the computational analysis.

CHAPTER 2. BACKGROUND

2.1. Anatomy & Physiology

In the development of the modeling techniques described in this work, two primary biological systems will be examined, specifically articular cartilage and intervertebral discs. In this section, the anatomy of each of these systems will be described in detail, with specific attention paid to how the various components contribute to the mechanical behavior of their respective systems.

2.1.1. Articular Cartilage Anatomy

Articular cartilage is a complex material with behavior dominated by the interactions of cross-linked collagen networks, proteoglycans, and interstitial fluid. The solid phase is largely comprised of type II collagen, which accounts for 15-22% of the wet weight of cartilage. Individual collagen fibers within the cartilage system form a series of intermolecular and intramolecular covalent cross-links that collectively make up a cohesive network. Though relatively weak in compression, collagen fibers are quite strong in tension and provide a high degree of tensile strength in the tissue [10].

The orientation of the collagen network varies significantly from the articular surface to the base of the cartilage, effectively segmenting the system into three primary zones: the superficial tangential, middle, and deep zone (Figure 2.1) [11]. The superficial tangential zone is characterized by a region of collagen fibrils running parallel to the articular surface and may be observed in the top 10-20% of the cartilage body. This region contains the highest collagen content of the three, with a concentration approximately 15% higher than in lower regions. Below this, and making up between 40-60% of the cartilage, is the middle zone. Here, the collagen fibrils are slightly larger than in the

superficial tangential zone and are arranged in a mostly random fashion with an orientation slightly trending towards a 45-degree angle. Near the base of the cartilage one finds the deep zone. The deep zone makes up the final 30% of the cartilage depth and is characterized by a roughly woven collagen network oriented perpendicular to the surface. Beneath this zone, the collagen fibrils insert into a shallow region of calcified cartilage attached to the subchondral bone. The organization of these zones leads to a complex, depth-dependent behavior with properties highly influenced by the respective fibril orientations of the composite layers [10, 12, 13].
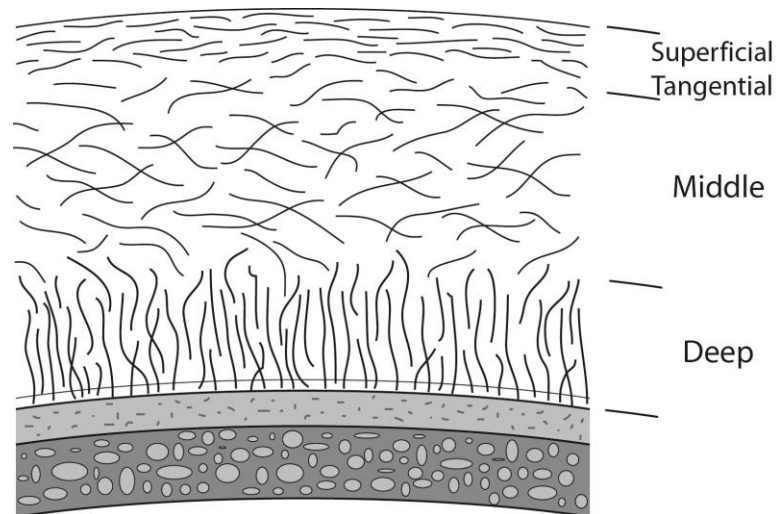
Figure 2.1: Articular cartilage may be separated into three distinct zones (superficial tangential, middle, and deep) distinguished by the organization of the collagen network.

After collagen, the next most prevalent component of the cartilage solid phase is proteoglycans [14]. Proteoglycans are macromolecules with a protein core covalently bound to several glycosaminoglycan (GAG) chains. Whereas the collagen network provides tensile strength, the proteoglycan network provides a strong resistance to compression due to both its bulk strength and to osmotic pressure and electrostatic

repulsion that arise between its fixed negative charges [15]. In addition to its load-bearing qualities, proteoglycan molecules have a direct influence on the permeability of the matrix and thus contribute to the regulation of fluid flow in the structure [16, 17]. The prevalence of proteoglycans in the cartilage is observed to be inversely related to that of collagen as one progresses through the structural zones, with the highest proteoglycans content observed in the middle and deep zones and lowest through the superficial tangential zone [10].

The remaining bulk of articular cartilage is predominantly interstitial water, accounting for 60-85% of the wet weight of articular cartilage. Water content has been found to be highest near the surface at approximately 80% total wet weight of the structure, and decreases to approximately 65% total wet weight in the deep zone [10]. The water associated with articular cartilage serves many functions. While a portion of the water is held by the matrix and contributes to osmotic pressure highly resistant to compression, unbound water within the structure may be exuded through the surface as the cartilage is compressed, only to be replaced following unloading [18]. Thus, regular loading of the cartilage provides an inflow source of fresh fluid and nutrients for the structure. In describing the mechanics of cartilage, an ideal model will ultimately account for both the bound fluid as well as the free water which flows through the structure [10].

When cartilage experiences degeneration, a loss in proteoglycan levels is observed followed by fluid loss and dehydration [19]. The site of first damage within the cartilage may differ between various forms of disease. For example, in the case of osteoarthritis degeneration generally occurs first near the cartilage surface, while early rheumatoid arthritis may incite degradation within the deep zone [11, 20]. The smaller joints of the hands typically see the first signs of arthritic degeneration, followed by the knees and other larger joints [21-24]. In all cases, damage to the structure eventually spreads throughout the entire cartilage body accompanied by severe degradation of the local collagen network [11]. The end result of this degeneration is a severely compromised structure causing pain and weakness when subjected to otherwise normal loading [25].

2.1.2. Intervertebral Disc Anatomy

The intervertebral disc serves primarily to provide a degree of mobility to the spine while also transferring compressive loads and providing a means for absorbing the kinds of impacts to the spine normal in an active individual [26]. The intervertebral disc and articular cartilage, though different in both structure and function, share many of the same basic structural components (collagen, proteoglycans, internal fluid) described in the previous section and therefore have some mechanical aspects in common.

The central region of the intervertebral disc is occupied by the nucleus pulposus. The nucleus pulposus is a viscoelastic gel-like structure consisting of proteoglycans and fluid surrounding a randomized network of small collagen fibrils (Figure 2.2). When subjected to external loading by the body, swelled proteoglycans act in conjunction with fluid trapped by the matrix, resulting in the development of an internal pressure capable of supporting large compressive loads [8, 27, 28].

Surrounding the nucleus pulposus is the annulus fibrosus, which principally acts to support the nucleus as it expands under compressive loading and anchors the disc to the cartilaginous endplates that cap the top and bottom of the disc [26]. The annulus fibrosus consists of multiple concentric layers of lamellae with highly organized collagen fibrils oriented at angles of approximately ±65 degrees from vertical, with the fibril angle alternating in successive layers of the annulus [27]. This arrangement of collagen fibrils within the annulus takes advantage of collagen's natural strength in tension [29]. As the disc is compressed in the axial direction, the nucleus and annulus expand in the radial direction under the applied load. This expansion places the collagen fibrils of the annulus under a tensile load which provides the structural strength necessary to withstand the mounting internal pressure and contain the disc [8, 27].

Water content of the disc varies with region and health. In the nucleus, for example, water may constitute as much as 80-90% of the volume of a healthy disc while occupying 60-70% of the annulus. This volume will fluctuate throughout the course of a day, as

loading cycles push water out of the structure only to be replenished later through unloading and rest [8, 27].
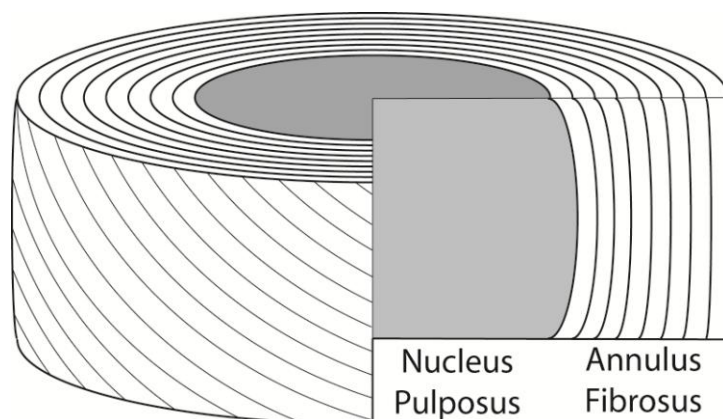
Figure 2.2: The intervertebral disc consists of a central nucleus pulposus surrounded by the annulus fibrosus. The nucleus pulposus is a gel-like structure consisting of proteoglycans and fluid surrounding a randomized network of small collagen fibers. The annulus is a highly organized structure of collagen fibers arranged in several layers of concentric lamellae.

Degeneration of intervertebral discs through damage or disease is a painful process that has a significant transformative effect upon the internal structure and mechanics of the disc [30]. Among the effects that may occur within a degenerated disc are a loss of water and proteoglycan content, leading to loss of disc height, dehydrated tissue and an inability to maintain internal pressures or adequately support external loading [8, 31]. As the degenerative process continues, the integrity of the structure becomes severely compromised and distinctions between the regions of nucleus and annulus become less clear [32]. Meanwhile, the annulus is forced to bear a higher proportion of the load as nucleus pressure decreases [33, 34]. Tearing of the disc tissue may develop, and damage to surrounding areas of the spine may occur as they become subjected to abnormal and excessive loading patterns [7, 33].

2.2. Biomechanical Modeling Techniques

A number of numerical-based methods have been developed in recent years with the goal of more fully describing and characterizing the mechanics of soft tissue interactions in load bearing joints. While computer simulations have typically dominated the field, other methods have been developed recently to model behavior using imaging techniques in combination with numerical methods to describe the deformation of tissue. To date, however, there has been a dearth of alternatives to finite element simulations for describing stresses within a load-bearing tissue or describing behavior beyond that characterized by computed strains.

Finite element analysis has long been a popular means of estimating stress and other physical phenomena in biomechanics. While it was common in years past to use an idealized geometry approximating a joint or system, if proper care is not taken these models have the risk of underestimating joint stresses due to the fact that perfect conformation between mating surfaces rarely occurs naturally within the body [35, 36]. In recent years image-based geometries have become the dominant basis for modeling. By this method, computerized tomography (CT) or magnetic resonance imaging (MRI) is used to create a digital replica of a given joint geometry for use in finite element or mathematical analyses of the loading or contact response, thus providing a patient-specific representation of the anatomy [37-47]. Although typically used in the development of geometry for articular joints, MRI-based geometries have also been used in creating geometries of soft biological systems such as the brain [48, 49]. In some cases, additional data obtained from MRI may be used to provide information regarding the system's internal structure in the development of finite element models [50-52].

A variety of constitutive models may be used in such modeling of joint mechanics. A linear elastic model, for example, provides a simple and straightforward relation between stress, strain, and material properties. Nonlinear models, in contrast, are more complex, yet far more descriptive of biomaterial behavior [53, 54]. However, while the measurement of tissue mechanics *ex vivo* for compression/tension [55, 56], shear [57], or

poroelasticity [58] test conditions are common for determining relevant material parameters for these models, the results may not provide an accurate description of a living tissue's response under normal loading conditions within an intact joint. Consequently, a given simulation may pair a highly accurate and specific geometry with a very broad estimate of material properties in order to model behavior [59]. Such methods may provide an estimate of joint response within a statistical range found in normal individuals, but have little application to diagnose or monitor individual patients.

In the field of cartilage mechanics, biphasic and triphasic mixture theories are perhaps the most widely accepted models of mechanical behavior. The traditional biphasic model considers the loading response of cartilage to be the net result of the mechanical contributions of separate fluid and solid constituents [60]. In these models, the solid constituent is considered as the collagen/proteoglycan/bound water matrix and is typically assumed to behave as an incompressible, porous, hyperelastic solid. Frictional drag resulting from interstitial flow of unbound fluid is assumed to be a dominant factor contributing to a tissue's resistance to compression [10, 14, 61].

The triphasic model is an extension of the biphasic model which takes into account the effects of charge within the tissue [62, 63]. This model is based on the concept that there is an interaction between fixed charges associated with proteoglycan content and the ions within the interstitial fluid that can affect fluid transport and diffusion throughout the interstitium [64, 65]. Regions with a higher fixed charge density are observed to be more resistant to compression, thus resulting in changes to mechanical behavior [61]. Although differences may be observed between the more complex, charge-inclusive models and the simpler biphasic model over an extended period (10 or more seconds), within short loading cycles typical of gait (~1 second) the two models produce very similar results [65].

While the preceding techniques use mathematical models to describe the mechanics of the cartilage system, certain imaging-based methods have been used in recent years to

quantify deformations and mechanical properties of tissue noninvasively. This includes the use of ultrasound waves and a technique known as magnetic resonance elastography [66-68]. Both of these methods rely on the imaging of transient shear waves to obtain a measure of the elastic response of an object and thus determine bulk material properties. While knowledge of the elastic behavior of a material can be valuable, little additional knowledge of the stresses of a system can be directly obtained by these methods. Alternatively, MR tagging techniques may be used to directly track the deformation of a tissue throughout its volume and has found use in cardiovascular as well as cartilage systems [69, 70].

An alternative method whereby the deformation field of a biomaterial may be obtained is referred to as hyperelastic warping. In this method, differences in image intensities between a template (reference) image and a target (loaded) image are used to generate a body force that deforms a finite element representation of the template such that it aligns with the target. To arrive at the final result, an optimization technique is used such that the strain energy function of the model is minimized [71]. While noninvasive, the technique does require some knowledge or estimate of the material properties of the system being analyzed, obtained either experimentally or from the literature [72]. Applications of this technique have included noninvasive measurement of strains in materials as diverse as ligament and the left ventricle [73, 74].

Direct measurement of displacements within tissue has been demonstrated recently using displacement-encoded magnetic resonance imaging (MRI). Displacement-encoded MRI is a method that calculates the displacement of each pixel within an image set during low frequency periodic motion. The technique has been used to noninvasively determine deformations across a range of applications, including the heart [75], brain [76], spine [32], and joint cartilage [77-79]. Displacements calculated by this technique may then be used to directly calculate strain fields in the material associated with the deformation.

Despite the number of models and techniques that have been employed in soft tissue biomechanics, there has been a clear and significant gap in the ability to fully determine patient-specific, noninvasive estimates of soft tissue mechanics *in vivo*. In this work, a modeling technique for simultaneously evaluating stresses and estimating material properties is developed utilizing displacement fields obtained by displacement-encoded MRI. Based on measured deformations in cartilage or other tissue, it is proposed that stress patterns and intrinsic properties may be estimated through computational analysis.

CHAPTER 3. A ONE REGION, HOMOGENEOUS MODEL FOR ESTIMATION OF
STRESSES AND MATERIAL PROPERTIES IN PORCINE TIBIOFEMORAL
CARTILAGE FOR THREE CONSTITUTIVE MODELS

3.1. Introduction

In this chapter, the feasibility of a new and computationally efficient technique is
demonstrated incorporating MRI-based deformations with mathematical modeling to
noninvasively evaluate the mechanical behavior of biological tissues and materials. These
methods were applied to a juvenile porcine tibiofemoral model, which was assumed to
behave as a single, homogeneous material region due to its developing state. Three
constitutive (i.e. linear Hookean, and nonlinear Neo-Hookean and Mooney-Rivlin)
relations with known loading conditions and MRI-based displacement measures were
employed to estimate stress patterns and material properties in the articular cartilage of
these joints.

3.2. Methods

3.2.1. Magnetic Resonance Imaging

Two-dimensional *in situ* displacements and strains were previously determined in
juvenile porcine tibiofemoral joints (*n*=7) using displacement-encoding with stimulated
echoes (DENSE) and a fast spin echo (FSE) [77]. The porcine legs (approximately 4
weeks old) were obtained freshly frozen from a local abattoir and remained frozen until
use. Briefly, the intact joints were intermittently and cyclically compressed at one times
body weight (78 N; 0.3 s and 1.2 s ramp and total loading times, respectively) with a
custom loading apparatus inside a 7.0 Tesla MRI system (Bruker GMBH, Ettlingen,
Germany) until a steady-state load-displacement response was achieved. Loading was

applied to the joints via a double-acting pneumatic cylinder, computer-controlled by an electro-pneumatics system. A steady-state load-displacement response was considered to have been reached when the linearly time-regressed slope of pneumatic cylinder displacement per 10 second cycle fell below a criterion of half the spatial resolution divided by total imaging time, or 0.0163 μm/s with a total imaging time of 128 minutes [80]. For each joint, displacement-encoded phase data from a single sagittal slice through the medial tibiofemoral joint was acquired (3000 ms repetition time, 21.6 ms echo time, 256×256 pixel matrix size, 64×64 mm^2 field of view, 250 μm spatial resolution, 1.5 mm slice thickness). Displacements in the loading (y) and transverse (x) directions within the femoral and tibial cartilage were calculated and smoothed for strain estimation using MATLAB software (The Mathworks, Natick, MA) [81]. Additionally, adjacent sagittal slices were imaged using conventional MRI (i.e. multi-slice two-dimensional FSE acquisitions) to record the anatomy of each joint and estimate the area of contact between the tibial and femoral cartilage.

3.2.2. Computational Analysis of an Intact Joint

Mathematical models of femoral and tibial cartilage representing a range of constitutive relations were developed and implemented in MATLAB. In these models, each pixel in the cartilage region of interest was treated as a separate isotropic unit cell. Stress values were computed at each pixel using stress-strain relations and strain data obtained from MRI.

For this study, stresses were analyzed in a cross section through the medial condyle. The 78 N load at the cartilage interface was assumed to act in proportion to the ratio of the contact area of the medial condyle to the overall contact area of the joint, as estimated by anatomical MRI.

Considering the rapid (0.3 s) loading of the joint and the high water content of the cartilage, nearly incompressible behavior (i.e. Poisson's ratio of 0.49) was assumed [82]. In addition, a plane stress assumption was used for all models. This assumption allows

for deformation in the *z*-direction, a necessity to maintain incompressibility under loading.

A linearly elastic material was considered first in this analysis. Stresses were related to strain data in the *x*, *y*, and *xy*-directions by Hooke's Law relations as follows:

$$\sigma_{xx} = \frac{E}{(1-\nu^2)}\left(E_{xx} + \nu E_{yy}\right),$$ (2.1)

$$\sigma_{yy} = \frac{E}{(1-\nu^2)}\left(E_{yy} + \nu E_{xx}\right),$$ (2.2)

$$\sigma_{xy} = \frac{E}{2(1+\nu)} 2E_{xy},$$ (2.3)

where ν is Poisson's ratio, E is Young's Modulus, and E_{xx}, E_{yy}, and E_{xy} are the strains in the *x*-, *y*-, and *xy*-directions, respectively.

An initial Young's Modulus was estimated and stresses were calculated at each unit cell. To determine whether this estimate was appropriate, the predicted load at the joint contact region was compared to the actual (78 N) value of the applied load. Here the region of contact was defined as the locations along the joint surface where strains normal to the surface curvature were negative (Figure 3.1). The forces along this region were estimated by first finding the component of stress acting in the loading direction at each pixel along the joint surface. The corresponding stress values were multiplied by the cross-sectional area of the unit cell to determine the force acting in the loading direction. The force values were then summed and compared to the known applied load. The value of Young's Modulus was subsequently iterated until the error between calculated surface forces and the known load input fell to within a value of 0.1% of the applied load.
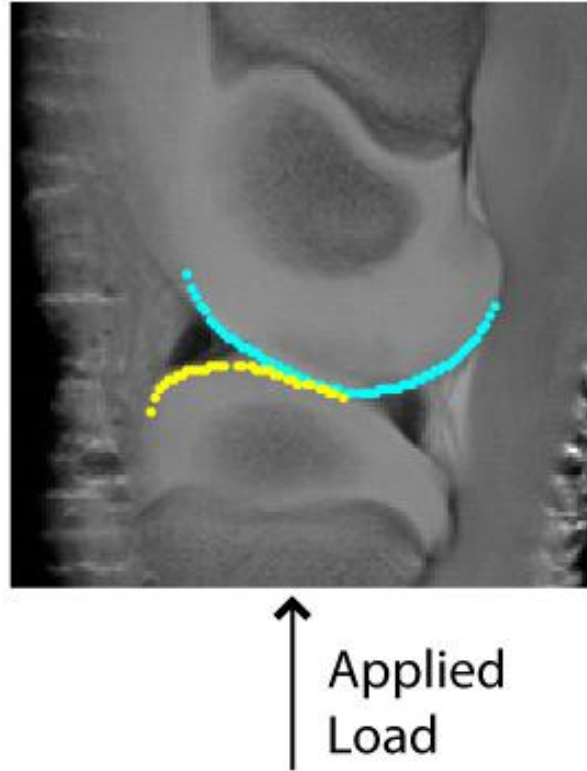
Figure 3.1: Lines of contact along each joint surface were defined as the locations of negative strain normal to the surface curvature. In this representative image, the lines of contact for the femur and tibia are shown by the blue and yellow lines, respectively. These points were then used by the models to compare the calculated boundary force to the known applied load. Material constants were iterated until the boundary condition was satisfied to within 0.1% of the load value [9].

Second, an incompressible Neo-Hookean model was considered. Here, the strain energy density function was given by

$$W = \frac{c_1}{\beta}\left(J^{-2\beta} - 1\right) + c_1(I_1 - 3) - p(J - 1), \tag{2.4}$$

where I_1 is the first invariant of the right Cauchy-Green tensor, C, J is the determinant of the deformation gradient, c_1 and β are material parameters, and p represents a hydrostatic

pressure term included to enforce incompressibility. The Second Piola-Kirchoff stress tensor, S, with the identity tensor, I, was then determined by

$$S = 2c_1\left(I - J^{-2\beta}C^{-1}\right) - \tfrac{p}{2}(det C)^{-1}. \tag{2.5}$$

Imposing the incompressibility assumption and neglecting the stress in the z-direction, consistent with the plane stress assumption, yields a relationship for the hydrostatic pressure:

$$p = \frac{2\left\{c_1\left[1-(C^{-1})_{33}\right]\right\}}{(det C)(C^{-1})_{33}}. \tag{2.6}$$

An initial value of c_1 was estimated and iterated as before, until the error between estimated and known applied load fell to within 0.1%.

The final model examined the case of an incompressible Mooney-Rivlin hyperelastic solid, given as

$$W = c_1(I_1 - 3) + c_2(I_2 - 3) - p(J - 1), \tag{2.7}$$

where c_1 and c_2 are material parameters, I_2 is the second invariant of the Cauchy-Green tensor, and p is hydrostatic pressure. The Second Piola-Kirchoff stress was calculated as

$$S = 2\left\{c_1 I + c_2[(tr C)I - C] - \tfrac{p}{2}(det C)C^{-1}\right\}. \tag{2.8}$$

Neo-Hookean solids are a specialized case of the Mooney-Rivlin model, and as such the same assumptions used in the incompressible Neo-Hookean model were repeated (i.e. a plane stress model with isotropic behavior). With stress in the z-direction assumed to be zero, the term for hydrostatic pressure can be written in terms of the parameters c_1 and c_2 as

$$p = \frac{2[c_1 + c_2(tr\boldsymbol{C} - \boldsymbol{C}_{33})]}{(det\boldsymbol{C})(\boldsymbol{C}^{-1})_{33}}.$$

(2.9)

An initial estimate for c_1 was determined from the value estimated in the incompressible Neo-Hookean case. This parameter was then varied across a range of ±10% of the initial estimate of c_1, with a value of c_2 iterated for each increment of c_1. The combination of c_1 and c_2 that resulted in a minimum error between calculated and known load was then used as estimates for the next iteration. For each subsequent iteration, the range and increment step was decreased to 10% that of the previous loop. This procedure was done to consecutively smaller ranges until the desired error of 0.1% was reached. Further, for each model, First Piola-Kirchoff stresses, $\boldsymbol{P}$, were calculated and plotted in accordance to the relation $\boldsymbol{P}=\boldsymbol{FS}$, where $\boldsymbol{F}$ is the deformation gradient and $\boldsymbol{S}$ is the Second Piola-Kirchoff stress tensor.

For each material parameter, the mean across all joints and standard error of the mean was calculated. Shear forces along the surface of the articular region were also calculated and summed for each model. Because a healthy joint typically exhibits a low coefficient of friction at the surface to enable smooth articulation, we reasoned that a calculated lower surface shear implies a more realistic and physiologically-relevant model. Consequently, the shear forces calculated along the contact surface were used as a method to directly compare relations.

3.2.3. Model Verification by Finite Element Simulation

The mathematical formulations implemented in the finite strain-based model were verified by comparison to a finite element simulation of a material with known stress and strain fields. Three models were created, representing material behavior governed by each of the aforementioned constitutive relations. A simple two-dimensional block measuring 5 cm square was created using the COMSOL Multiphysics software package (3.2 COMSOL AB, Stockholm, Sweden). Plane stress models with rectangular mesh elements arranged in a 256×256 grid were used, resulting in 65,536 total mesh elements

and 526,338 degrees of freedom. The first model simulated material behavior in accordance with linearly elastic relations, with a Young's modulus of 12.5 MPa and Poisson's ratio of 0.49. The second model used Neo-Hookean constitutive relations and a material parameter, c_1, of 12.5 MPa. The final model was a Mooney-Rivlin model with material parameters of 12.5 MPa for c_1, and 3.5 GPa for c_2. Homogeneous material assumptions were used for each model.

In each model, the bottom boundary of the block was subjected to a distributed load of 39 N in the *y*-direction, and 7.8 N in the *x*-direction, similar to values estimated from *in situ* cartilage loading. Constraints in the *x*- and *y*-directions were imposed on the top boundary of the block to restrict motion. After solutions for the simulation models were generated, the resulting strain fields and compressive load in the *y*-direction were used as inputs for the mathematical models. Error between the calculated stresses and those generated by finite element analysis was subsequently calculated as a means of evaluating mathematical error in the finite strain-based model. For each analysis, the root mean squared error was calculated between estimated and known stress fields, and was further normalized by the maximum value of the known stress field.

3.3.   Results

3.3.1. Magnetic Resonance Imaging

Based on the proportion of medial to total contact area determined by conventional MRI, the load applied to the medial compartment of each joint varied among samples (Table 3.1). Displacements from DENSE-FSE and computed strain patterns were heterogeneous (Figure 3.2).

Table 3.1: The fraction of total load applied to the medial condyle in this analysis was estimated for each joint as the ratio of medial contact area to total contact area of the joint, as determined by conventional MRI. The total load applied to each joint was 78 N.

Joint	Medial Contact Area (mm2)	Total Contact Area (mm2)	Est. Medial Load (N)
1	16.50	44.63	28.84
2	29.25	54.94	41.53
3	11.63	32.63	27.79
4	16.13	37.50	33.54
5	15.19	30.00	39.49
6	19.31	43.88	34.33
7	21.19	46.88	35.26
ALL	18.46 ± 2.13	41.49 ± 3.28	34.40 ± 1.91
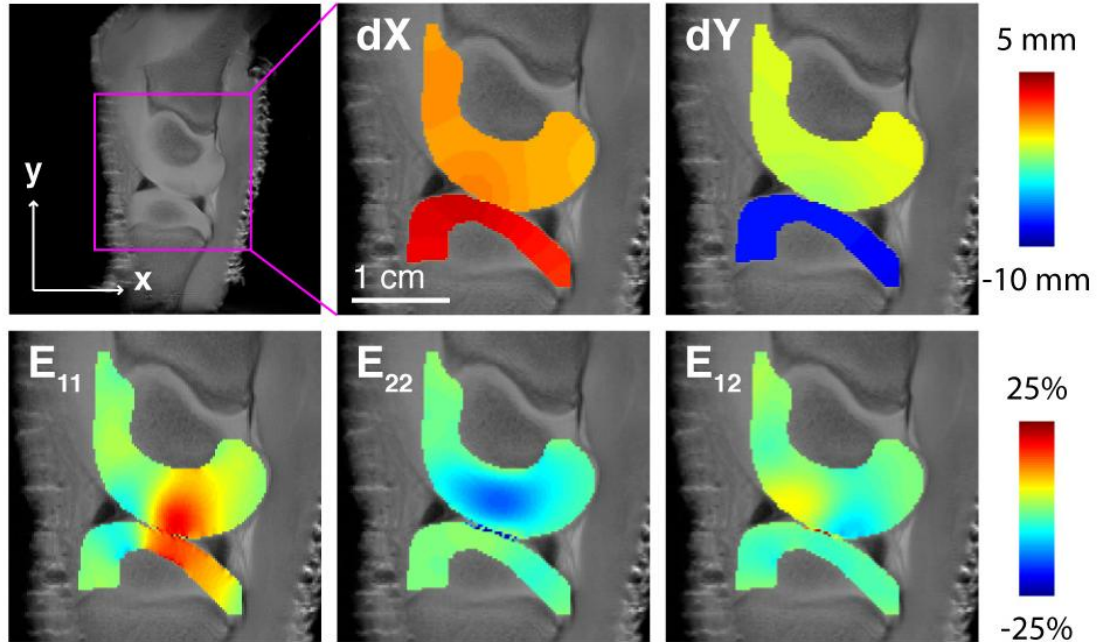
Figure 3.2: Displacements determined by displacement-encoded MRI (dX and dY) and the corresponding heterogeneous strain fields were used as inputs to the models. In this representative image, areas of high tensile strain in the x-direction and high compressive strain in the y-direction can be seen in the central region of the joint [9].

3.3.2. Computational Analysis of an Intact Joint

As expected, the models produced non-uniform stress distributions throughout the tibiofemoral cartilage. The calculated distributions for the linear elastic, Neo-Hookean, and Mooney-Rivlin relations showed similar stress patterns but differed in magnitude (Figure 3.3). In these models, compressive stresses developed in the direction of loading, with a region of positive stress in the loading direction at the cartilage-cartilage interface. A second tensile-stress region in the loading direction was also observed at the bone-cartilage interface.

The lowest mean surface shear values were found with the application of linear Hookean relations, followed closely by the Neo-Hookean and Mooney-Rivlin models. The mean Young's Modulus for the seven joints was estimated by the linear model as 5.83 ± 2.44 MPa. Material constants for nonlinear relations varied for the femur and tibia (Table 3.2).
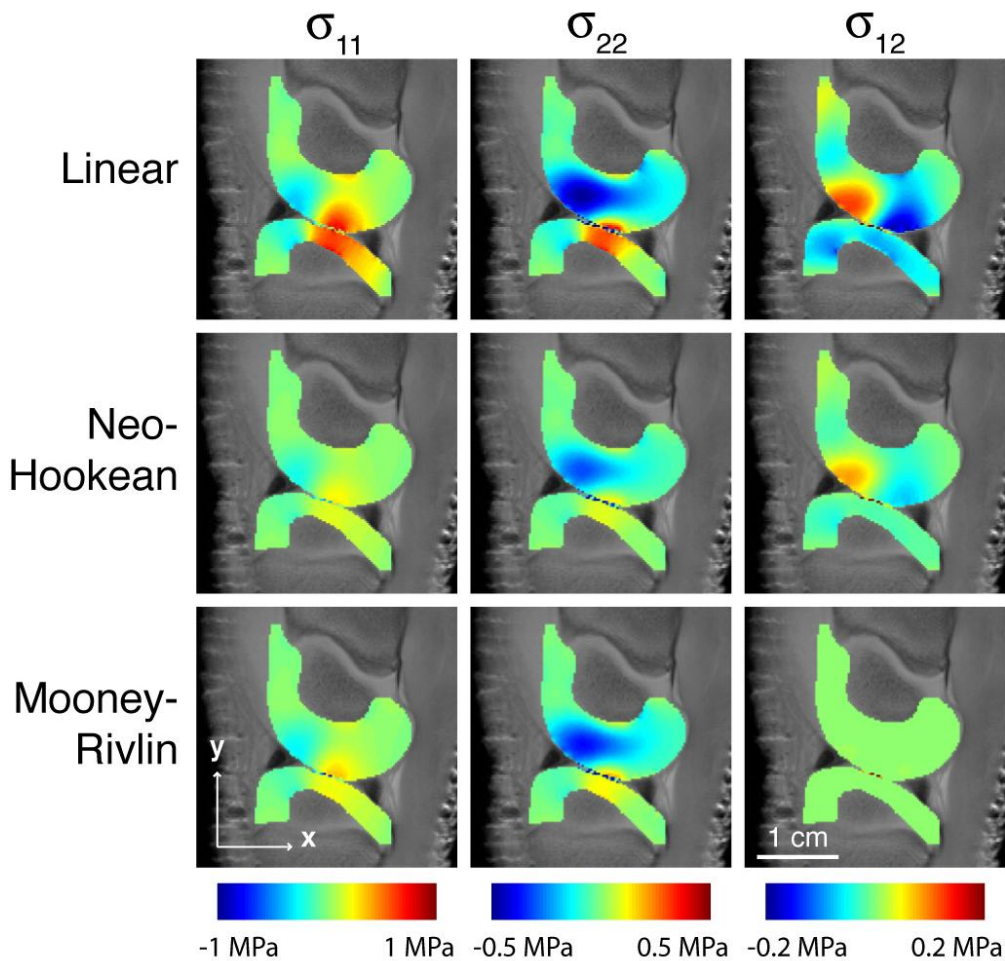
Figure 3.3: Heterogeneous stress fields were estimated and plotted for each computational model. For the joint in this representative image, the linear model estimated Young's Modulus values of 3.54 MPa and 4.21 MPa for the femur and tibia, respectively. Similarly, the Neo-Hookean model estimated c1 parameter values of 0.27 MPa and 0.27 MPa at the femur and tibia. The Mooney-Rivlin model estimated c1 parameter values of 0.25 MPa and 0.25 MPa, and c2 values of 15.52 kPa and 5.00 kPa, for the femur and tibia, respectively. Stresses estimated by modeling the joint with nonlinear Neo-Hookean relations are similar in distribution to that of the linear case, but exhibit lower peak stresses. Although stresses produced by the model developed with Mooney-Rivlin relations showed similar distributions to the other models in the loading and transverse directions, shear stresses were substantially lower throughout the cartilage regions [9].

Table 3.2: Forces and model parameters (mean ± standard error of the mean) were calculated at the joint surface for each set of constitutive relations. Here, surface shear force was the calculated force along the contact surface tangential to the joint curvature.

		Linear			Neo-Hookean			Mooney-Rivlin		
Total Surface Shear Force (N)	Femur	13.25	±	7.67	9.90	±	5.08	12.21	±	1.25
	Tibia	8.46	±	6.58	12.15	±	4.69	15.71	±	3.15
	Mean	10.85	±	6.93	11.03	±	4.72	13.96	±	2.40
E (MPa)	Femur	5.99	±	2.67						
	Tibia	5.66	±	2.41						
	Mean	5.83	±	2.44						
c_1 (MPa)	Femur				0.68	±	0.40	0.66	±	0.42
	Tibia				0.66	±	0.42	0.67	±	0.46
	Mean				0.67	±	0.39	0.66	±	0.42
c_2 (MPa)	Femur							0.32	±	0.29
	Tibia							0.18	±	0.14
	Mean							0.25	±	0.22

3.3.3. Model Verification by Finite Element Simulation

The linear mathematical model correctly estimated a Young's Modulus of 12.5 MPa for the linearly elastic finite element simulation, exactly matching the simulation input. Similarly, the Neo-Hookean model converged to a value of 12.54 MPa for the parameter c_1, which was within 0.3% of the finite element simulation input of 12.5 MPa. The Mooney-Rivlin model exhibited the largest discrepancy in estimates when compared to the parameter inputs of the finite element simulation. The Mooney-Rivlin model estimated values of 10.3 MPa and 2.39 GPa for c_1 and c_2, respectively, which resulted in an estimation error of 17.5% for c_1 (model input: 12.5 MPa) and 31.8% for c_2 (model input: 3.5 GPa).

In the *y*-direction, the linear elastic and Neo-Hookean models produced errors in stress estimation averaging 0.00% and 2.25%, respectively, while the Mooney-Rivlin model produced the largest error at 8.67% (Table 3.3). In the *x*-direction, errors of 0.00% and 0.60% were calculated for the linear and Neo-Hookean models, and the Mooney-Rivlin model again produced the largest error of 102%. Estimates of error in the shear direction were 0.00%, 0.33%, and 201% for the linear, Neo-Hookean, and Mooney-Rivlin models, respectively (Figure 3.4).

Table 3.3: Strain fields were generated with finite element analysis simulations that modeled a material using linearly elastic, Neo-Hookean, and Mooney-Rivlin constitutive relations. These strains were then used as inputs to their respective mathematical models. The stresses calculated by the models for each set of strains were then compared to the known simulated stresses. The error between the stress values estimated by the models and the known stress field was calculated for each set as the root mean square deviation, normalized by the value of maximum stress of the known stress field.

	Linear Model Error (%)	Neo-Hookean Model Error (%)	Mooney-Rivlin Model Error (%)
σ_{xx}	0.00	0.60	102.01
σ_{yy}	0.00	2.25	8.67
σ_{xy}	0.00	0.33	201.10
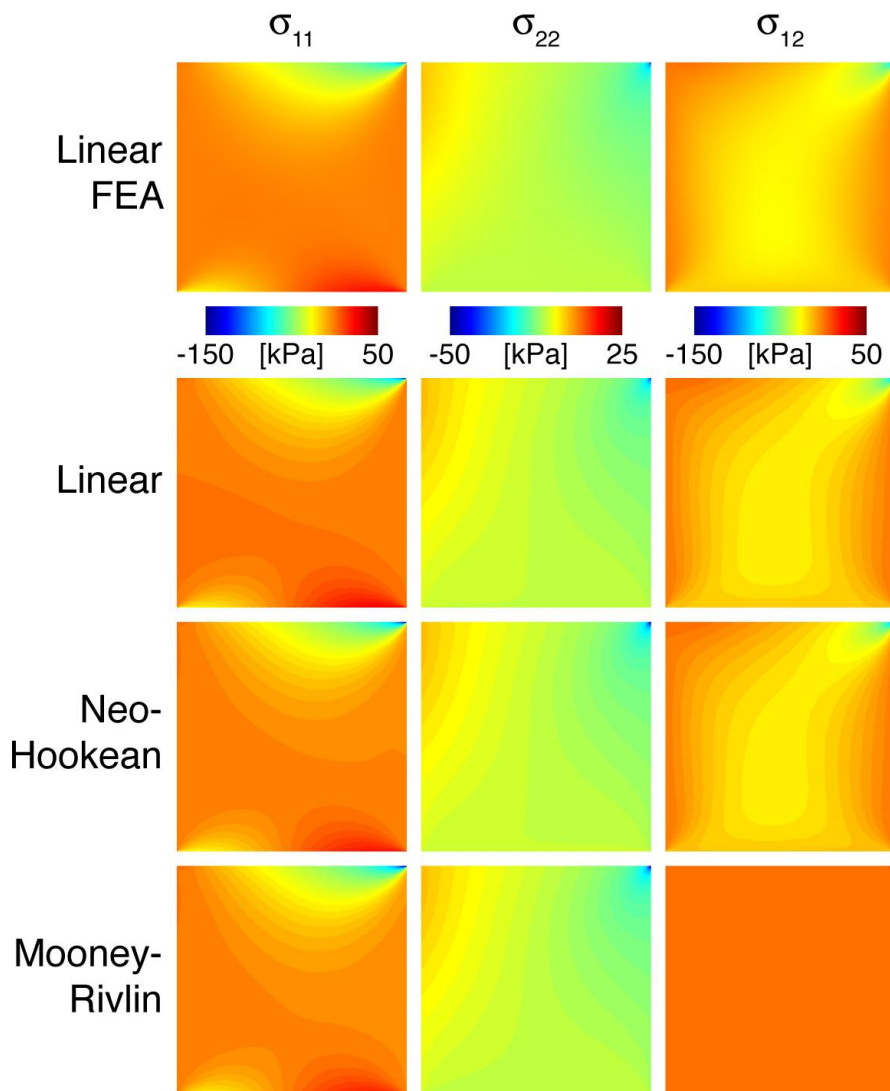
Figure 3.4: Simulated stress fields were generated by finite element analysis for a linearly elastic, Neo-Hookean, and Mooney-Rivlin solid subjected to a compressive vertical load of 39 N and a positive shear load of 7.8 N. The corresponding strains were then used as inputs to the computational models. Here, the linearly elastic model correctly estimated a Young's Modulus value of 12.5 MPa. Similarly, the Neo-Hookean model estimated a value of 12.54 MPa for the parameter c1, which compared well to the actual simulation value of 12.5 MPa. The Mooney-Rivlin model estimated parameter values of 10.3 MPa and 2.39 GPa for model parameters c1 and c2, respectively, while the true simulation values were 12.5 MPa and 3.5 GPa [9].

3.4. Discussion

The work of this chapter developed and verified a mathematical method to characterize the mechanical behavior of articular cartilage non-invasively using MRI-based strains, and to identify the set of constitutive relations that produced the most consistent results. When the methods were applied to intact joints under known (e.g. cyclic compressive) loading conditions, there was good inter-model agreement of stress distributions, and modulus values estimated were within published ranges. Further, the methods described here were found to produce estimates of material properties that agreed closely with controlled finite element simulations.

The stress distribution estimates for the porcine tibiofemoral joint were largely consistent across models. Further, the mean modulus values determined from the linear analysis (5.99 MPa and 5.66 MPa for the femur and tibia, respectfully) both fall within the range reported for dynamic modulus of porcine cartilage [83]. Given the cyclic nature and rapid application of the load experienced by the joints, it is reasonable that estimates would approach dynamic, rather than equilibrium, values as the analysis essentially considers one section of a dynamic loading cycle in a nonlinear material. Interestingly, the mathematical models predicted tensile stresses in the loading (y) direction in the cartilage contact region. This may be explained by the fact that y strains found with DENSE-FSE in these regions were near zero, causing the constitutive relations to be dominated by the larger tensile strains in the transverse (x) direction.

When the models were implemented using finite element-based strain fields, material parameters were correctly estimated within 1% for the linear and Neo-Hookean models, and within 32% for the Mooney-Rivlin model. Further, all models were found to closely approximate the stress distributions and magnitudes in the y-direction, or the direction of primary loading. Here, the linear and Neo-Hookean models were within 2.5% of the known stresses, and the Mooney-Rivlin model correctly predicted stresses to within 9%. The linear and Neo-Hookean models also performed well in the estimation of stresses in the x-direction and in shear, where errors were within 1% for both models. In contrast,

the Mooney-Rivlin model produced errors of 102% and 201% in the *x*-direction and in shear, respectively. It is possible that the larger errors seen in the Mooney-Rivlin model may be contributed to the number of simplifying assumptions necessary here to reach a determinate system. Additional knowledge of system boundary interactions or deformations out of plane may be sufficient to constrain a higher order model such as the Mooney-Rivlin.

Based on a comparison of the overall stress distributions, shear values developed along the contact surface of the joint for each model, as well as a comparison of the models using finite element-based strain fields, we concluded that the incompressible Neo-Hookean relation provided the best estimates of the stress state of the tissue. Both the linear model and Neo-Hookean model resulted in near-identical shear forces at the surface of the joints, with values lower than those estimated using Mooney-Rivlin relations. However, the linear model consistently predicted large peaks in stress that did not occur in either nonlinear method. It is accepted that cartilage behaves as a nonlinear viscoelastic solid [10], and it is likely that the dramatic shifts in stress predicted by the linear model are a result of the limitations of a purely elastic assumption with the large strains calculated at the joints. From this, it follows that the Neo-Hookean hyperelastic relations with incompressibility assumptions provided the most appropriate model for the characterization of stresses using two-dimensional MRI-based displacements.

Assumptions necessary in this analysis may introduce error in the models. Isotropic, homogeneous behavior of the cartilage, for example, was assumed in order to arrive at a determinate system for the cartilage based upon the available knowledge of deformation and loading conditions. The inclusion of anisotropic constitutive relations [84], depth-dependent properties [85], or mixture theory [86] may further enhance the accuracy of the method in cartilage. In addition, expansion of the analysis to include three-dimensional displacement data should provide sufficient information to completely characterize the hyperelastic behavior of the tissue across a broad range of models with additional degrees

of complexity. Estimation of load distribution throughout the volume of the joint may lead to additional refinement of results [87, 88].

In conclusion, the work presented in this chapter represents the first steps towards a new and novel method for assessing stresses and material properties of intact articular cartilage non-invasively through the use of displacement-encoded imaging and mathematical modeling. Of the models developed here, the utilization of Neo-Hookean relations with known two-dimensional strains was found to produce the best estimation of stresses within a body under an applied load. As a result, Neo-Hookean relationships would serve as the basis for solid modeling of biomaterials in the succeeding chapters.

CHAPTER 4. DEVELOPMENT OF A HETEROGENEOUS, MULTI-MATERIAL MODEL WITH APPLICATION TO THE RABBIT INTERVERTEBRAL DISC SYSTEM

4.1. Introduction

With the groundwork laid for a modeling technique to estimate stresses and material properties noninvasively in soft tissue using known strain fields, it is possible to expand the complexity of the material of interest. Intervertebral discs present an ideal subject for the expansion of these techniques. The intervertebral disc consists of two distinct material types that exhibit disparate location- and direction-dependent properties which together must satisfy known boundary conditions and displacements. In this chapter, stress fields and material parameters will be investigated for rabbit intervertebral discs using a nonlinear, multi-material model.

4.2. Methods

4.2.1. Magnetic Resonance Imaging

Displacement and strain fields from the intervertebral discs of skeletally mature New Zealand white rabbits were determined previously using dualMRI in a 9.4 Tesla scanner [32]. Briefly, eight rabbits were treated in an annular puncture degeneration model between the fourth and fifth vertebrae (L4-L5) using a 16-gauge needle under aseptic conditions, and three were used as controls. Four weeks post-operation the rabbits were sacrificed and lumbar spine sections were isolated for imaging analysis. Both the punctured (L4-L5) discs and the untreated adjacent (L3-L4) discs were analyzed in the study, as were L3-L4 and L4-L5 discs from the controls.

The discs were subjected to a cyclic compressive load of 30 N for a period of 1.5 seconds, with a total cycle length of 3.0 seconds (Figure 4.1). Displacements were then measured in the axial and radial directions of a coronal imaging plane taken through the center of the IVD (Figure 4.2). A steady-state load-displacement response was achieved after 200 cycles, following which imaging commenced. Imaging parameters were: repetition time = 3000 milliseconds, echo time = 24.7 milliseconds, field of view = $16 \times$ 16 mm^2, matrix size = 128×128 pixels, and slice thickness = 1.0 mm. The deformation gradient and strains were then computed from the discrete displacement fields (Figure 4.3).

In addition to strain, the same study [32] evaluated GAG concentrations within the discs using delayed gadolinium-enhanced MRI (dGEMRIC). Gd-DTPA^{2-} was allowed to penetrate the discs over a period in excess of 9 hours, with image acquisitions taking place before and after exposure to the contrast agent. Relevant imaging parameters for this portion of the study were as follows: repetition time = 100, 200, 300, 500, 900, and 4000 milliseconds, echo time = 7.2 milliseconds, field of view = 16×16 mm^2, matrix size = 128×128 pixels, and slice thickness = 1.0 mm. This experiment permitted calculation of both longitudinal relaxation time constant (T_1) values before contrast and GAG concentration (Bashir, 1999) throughout the unloaded IVD.
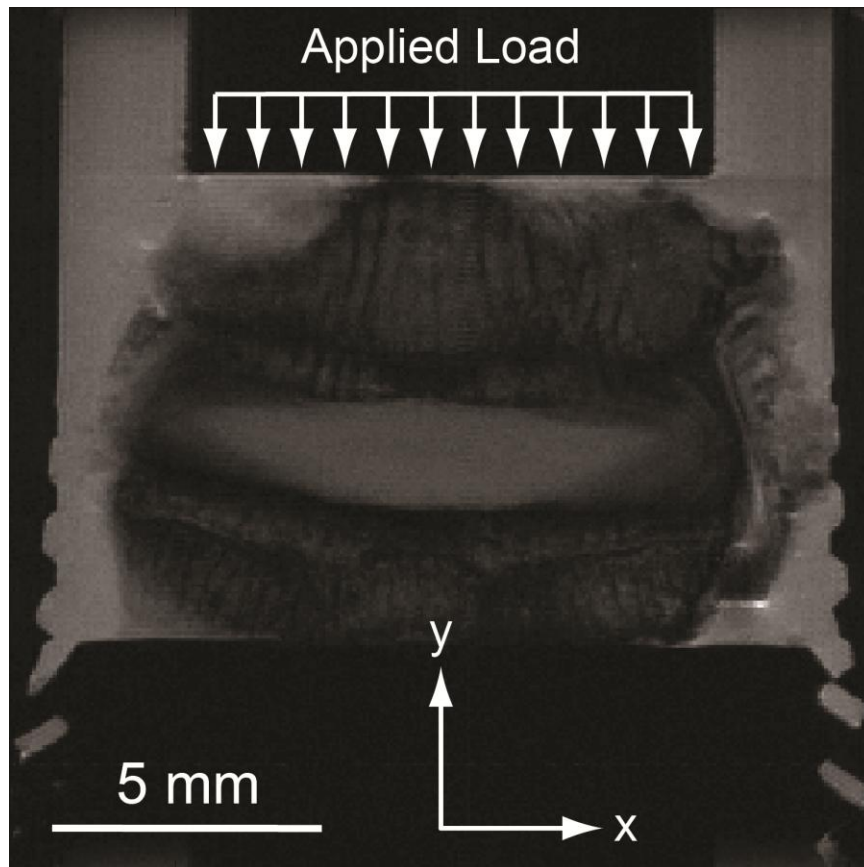
Figure 4.1: Two-dimensional displacements and strains were obtained with displacement-encoded MRI for rabbit intervertebral discs subjected to a cyclic 30 N load in the axial (y) direction.
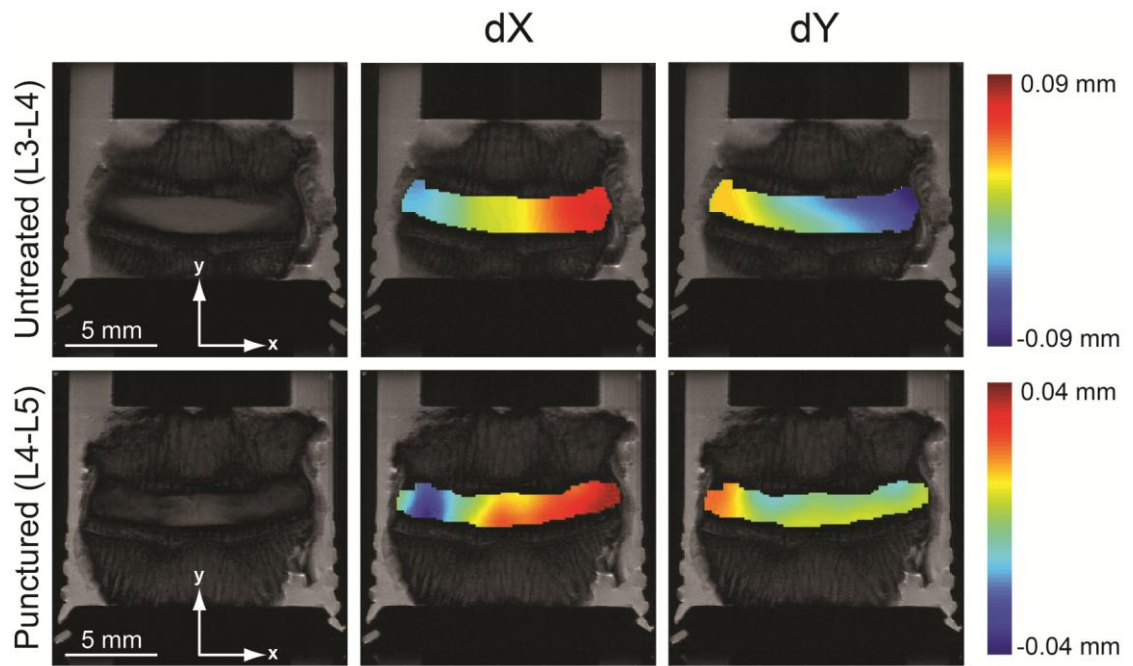
Figure 4.2: Displacements were measured within a coronal imaging plane oriented through the center of the disc for both punctured, degenerated discs as well as adjacent, unaltered discs, as shown in this representative pair.
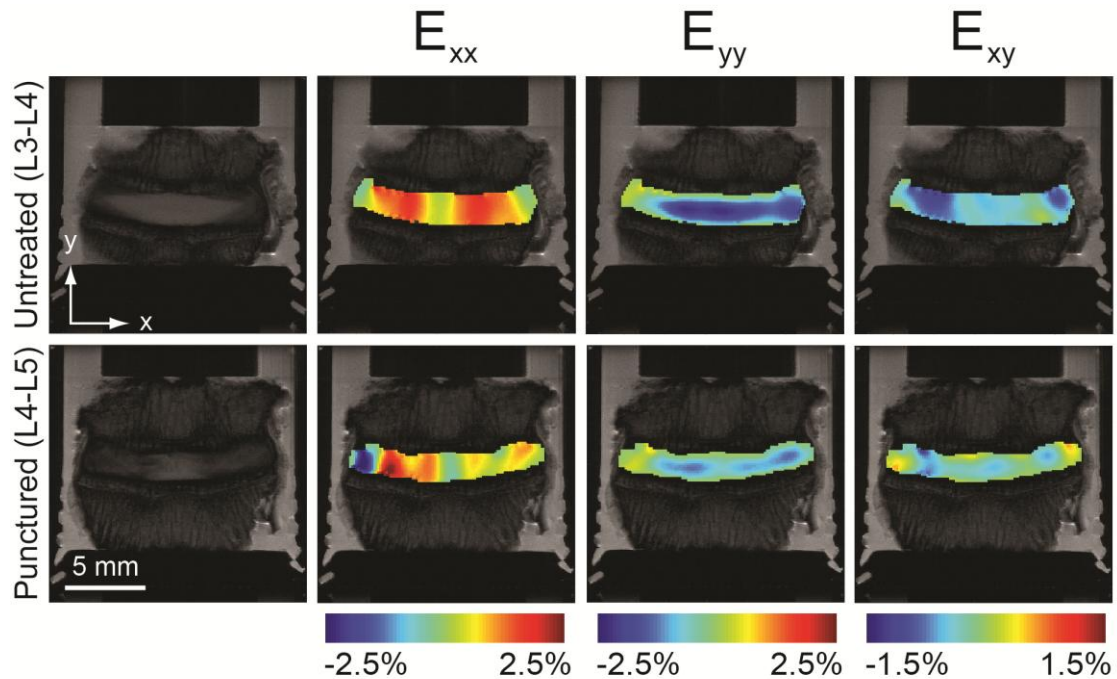
Figure 4.3: Strains were determined by dualMRI in paired samples of untreated (L3-L4) discs and adjacent (L4-L5) discs treated with an annular puncture to induce degeneration. In this representative pair, compressive strains in the loading (y) direction developed throughout the disc. In contrast, symmetric regions of tensile strain are observed to occur in the transverse (x) direction.

4.2.2. Computational Analysis of Intervertebral Disc

Stress distributions and material relations were determined in the IVD using a finite strain-based (FSB) computational model. MRI-based strains, describing the two-dimensional load-displacement response of a plane oriented through the center of the disc, were coupled with assumed material relations in this model. As such, a two-dimensional model with plane stress assumptions was used for the analysis. Importantly, the FSB model accounted for material composites, and the NP and AF were identified using a combination of histology and T_1 value maps acquired with MRI prior to exposure to the contrast agent. Histological slices were taken in the coronal plane through the center of the IVD and stained with hematoxylin and eosin. T_1 mapping provides an indication of relative bound water content, and therefore regions associated with the NP

and AF presented differing T_1 values in accordance with their differing biochemical composition (Figure 4.4). A minimum threshold of T_1 intensity was determined for each disc individually such that the area of each image with a T_1 value above the threshold corresponded to NP as observed with histology.
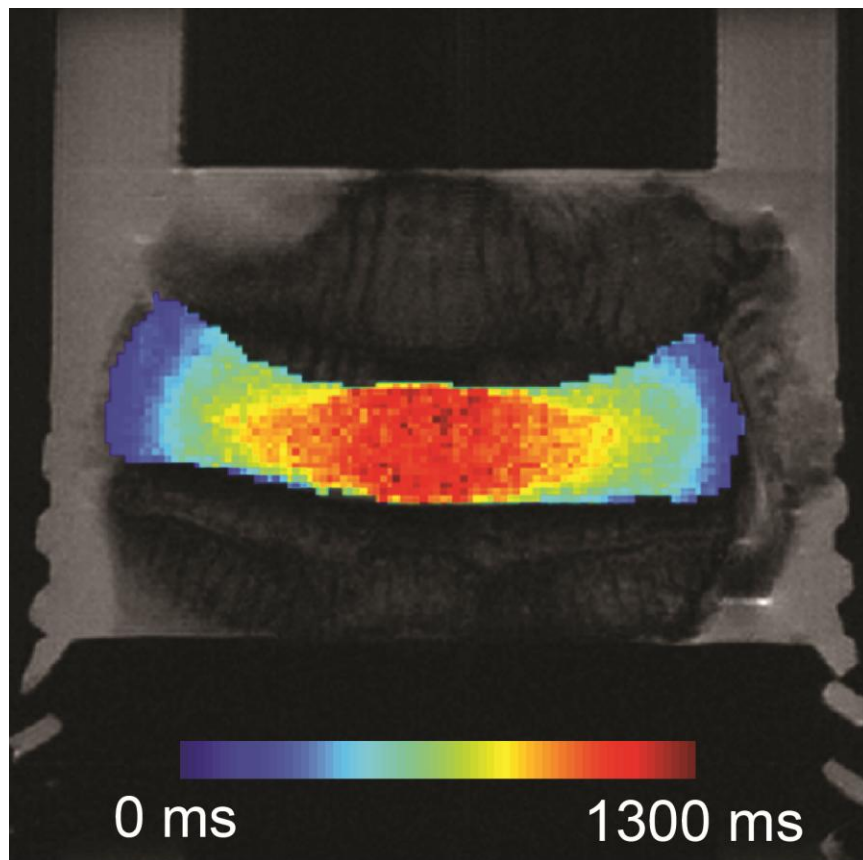
Figure 4.4: T_1 intensity was used to identify the nucleus pulposus and annulus fibrosus, with identifications confirmed by histology.

Because both the NP and AF exhibit large strains and nonlinear stress-strain behaviors, similar to the previous chapter both the NP and AF were modeled separately as incompressible Neo-Hookean materials [9], represented by the strain energy density function

$$W = \frac{c_1}{\beta}\left(J^{-2\beta} - 1\right) + c_1(I_1 - 3) - p(J - 1),$$ (4.1)

where I_1 is the first invariant of the right Cauchy-Green tensor, $\boldsymbol{C}$, J is the determinant of the deformation gradient, c_1 and β are material parameters, and p represents a hydrostatic pressure term included to enforce incompressibility [54]. The Second Piola-Kirchoff stress tensor, $\boldsymbol{S}$, was then determined by

$$\boldsymbol{S} = 2\left[c_1\left(\boldsymbol{I} - J^{-2\beta}\boldsymbol{C}^{-1}\right) - \frac{p}{2}(det\boldsymbol{C})\boldsymbol{C}^{-1}\right],$$ (4.2)

where $\boldsymbol{I}$ is the identity tensor.

Imposing the incompressibility assumption and neglecting the stress in the z-direction, consistent with the plane stress assumption, yields a relationship for the hydrostatic pressure:

$$p = \frac{2\left\{c_1\left[1 - (\boldsymbol{C}^{-1})_{33}\right]\right\}}{(det\boldsymbol{C})(\boldsymbol{C}^{-1})_{33}}.$$ (4.3)

Material behavior during compression is known to be related to proteoglycan content and, subsequently, GAG content [89, 90]. High proteoglycan content is typically accompanied by larger amounts of fluid associated with the surrounding matrix, and thus a higher resistance to compression may be observed [10, 15]. For example, a linear correlation between Gd-DTPA^{2-} and Young's modulus has been reported to occur in bovine articular cartilage [90]. In the model developed here, the Neo-Hookean material parameter c_1, which is linked to material stiffness, and proteoglycan content as measured

by dGEMRIC were assumed to exhibit a similar linear relationship [90]. This relationship may be represented by

$$c_1 = \gamma C, \tag{4.4}$$

where γ is the local GAG content in units of μg/mL, and C is a constant to be calculated by the model. By these means, heterogeneous properties that are dependent upon biochemical composition may be estimated within the system.

Two sets of conditions were imposed upon the model. The first was an equilibrium condition for the entire system in the loading direction. For this condition to be satisfied, the net force acting in the loading direction across an arbitrary plane must equal the external load applied to the system (Figure 4.5). The condition was tested at multiple planes across the disc, and the average result across the thickness of the disc was used in order to compensate for any discontinuities that may occur in the strain data.

The second condition applied to the system was the enforcement of a continuity condition across the boundaries separating the NP and AF. In essence, this condition states that, at any given point along the boundary between the NP and AF, forces normal to the boundary on either side must be equal to maintain equilibrium. This condition also allows for the determination of the relationship between material constants of the two regions relative to each other.

In order for the assumptions of the two-dimensional plane stress analysis to remain valid, it is necessary that the system of interest did not experience unbalanced or out-of-plane loading. As such, only specimens with strains indicating balanced loading conditions in the direction of loading were evaluated. A total of three matched pairs of punctured and adjacent discs met this criteria and were included in the stress analysis.
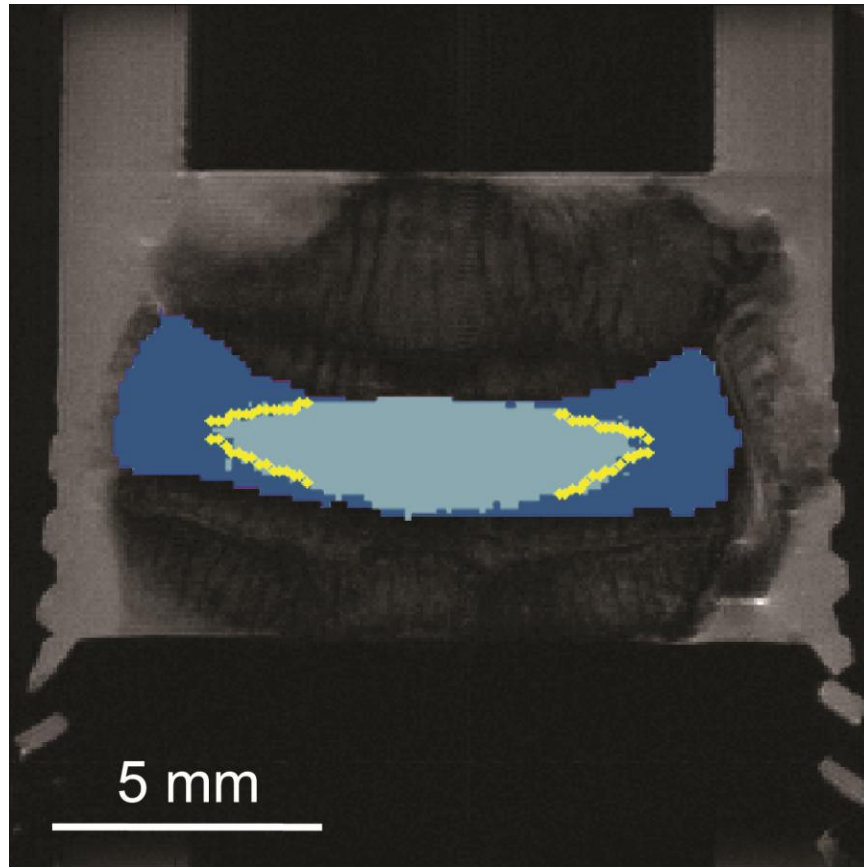
Figure 4.5: Regions corresponding to the nucleus pulposus (light blue) and annulus fibrosus (dark blue) were then isolated for analysis. An equilibrium condition was imposed upon the model such that the net force in the axial direction across an arbitrary plane through the disc (dashed white line) equaled the externally applied load. A secondary condition was imposed enforcing equilibrium of forces normal to the boundaries separating nucleus pulposus from annulus fibrosus (dotted yellow lines).

4.2.3. Model Verification by Finite Element Simulation

The predictive capabilities of the model were tested using a simplified finite element model generated in COMSOL (v3.2; COMSOL, Inc; Burlington, MA) with two-dimensional, Neo-Hookean plane stress assumptions. The simplified geometry consisted of an interior with a Neo-Hookean constant value of 40 MPa surrounded by an outer region with a Neo-Hookean constant of 4 MPa. The material parameters of this model were not necessarily of the same scale as those existing within a true intervertebral disc, but rather chosen such that a large difference in material behavior would be observed

across the two regions. By these means, a more rigorous test of the predictive capabilities of the model could be observed. Two thin regions analogous to the placement of cartilaginous plates were positioned at the top and bottom of the geometry to transfer an externally applied load and restrict motion in the transverse direction. A compressive load of 1000 N/m was then applied across the endplates. The model utilized a mesh consisting of 55,272 total elements with 310,979 degrees of freedom.

The resulting strain fields generated by the finite element simulation were exported as 128×128 grids and used as inputs for the computational model. The resulting estimates for the stress fields computed by the FSB model were then compared to the known stress fields of the finite element simulation. Error in stress estimation in each direction was then evaluated using the normalized root mean square error (NRMSE). Similarly, estimates of the material constants of the system computed by the strain-based model were compared to the known material parameters used as inputs to the finite element simulation.

4.3. <u>Results</u>

4.3.1. Computational Analysis of Intervertebral Disc

Heterogeneous stress fields were calculated for each of the six discs. As expected, dominant compressive stresses were calculated in the direction of loading for each disc, while both tensile and compressive stresses were observed in the transverse direction (Figure 4.6). Stresses were consistent in scale across specimens, with stresses computed within the range of ±1.5 MPa.
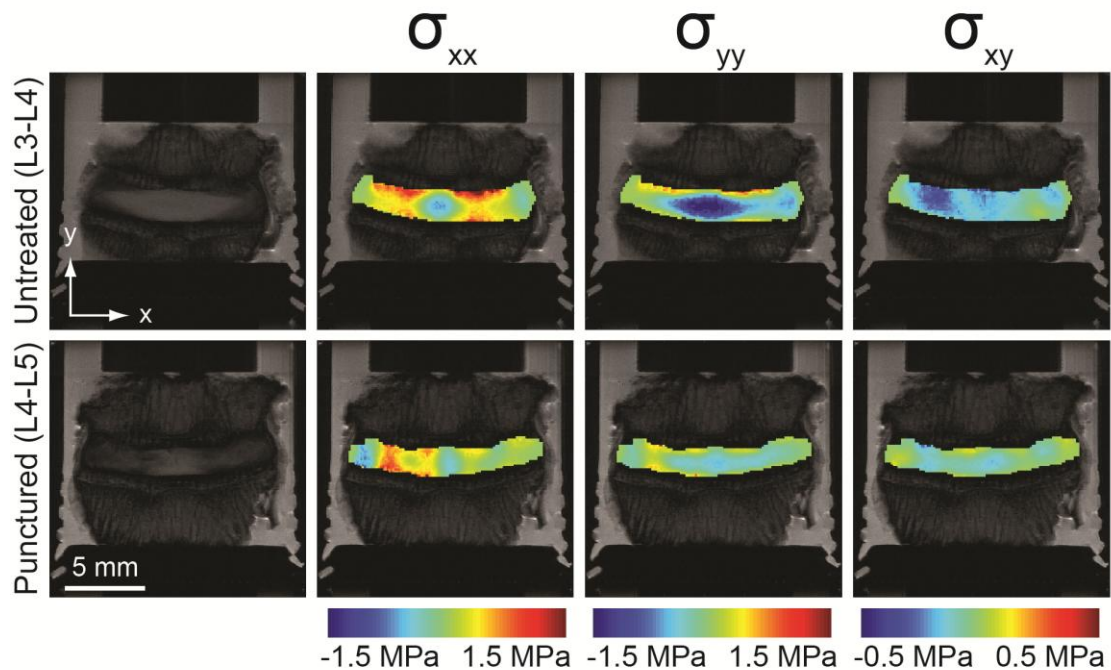
Figure 4.6: Stress fields were computed by a strain-based model as shown in these representative images. A large, defined central region of compressive stress was found to occur in both the loading and transverse directions of the untreated (L3-L4) disc, indicative of a healthy nucleus pulposus. A similar, but smaller, region was observed in the degenerated disc with compressive stresses more dispersed throughout the disc in the loading direction.

Two of the three untreated discs exhibited areas of axial and radial stress of similar distribution and magnitude at the center of the disc indicative of a large central nucleus region (Figure 4.7). In these instances the matching punctured discs exhibited either a smaller and less well defined central region of stress or no such region at all (Figure 4.8). Stress patterns in the remaining disc pair were not as well defined and as such did not allow for a direct comparison of disc structure or health from stress results alone.
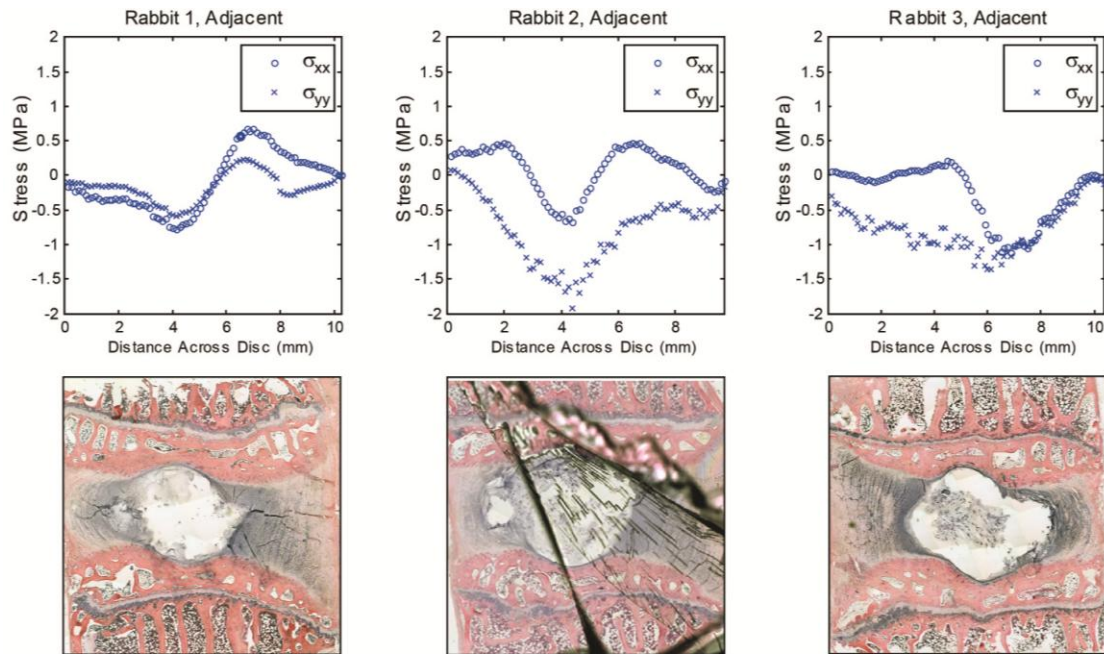
Figure 4.7: Stresses in the axial and transverse directions were plotted as a function of transverse distance across a middle plane of the disc for each of the adjacent, unaltered specimens (top). These stress profiles were then compared to histology of each disc (bottom) to compare local stress behavior to the disc anatomy. In each of these adjacent discs, a large nucleus region was observed in the histology where a noticeable increase in compressive stress may be observed in both the axial and transverse directions.
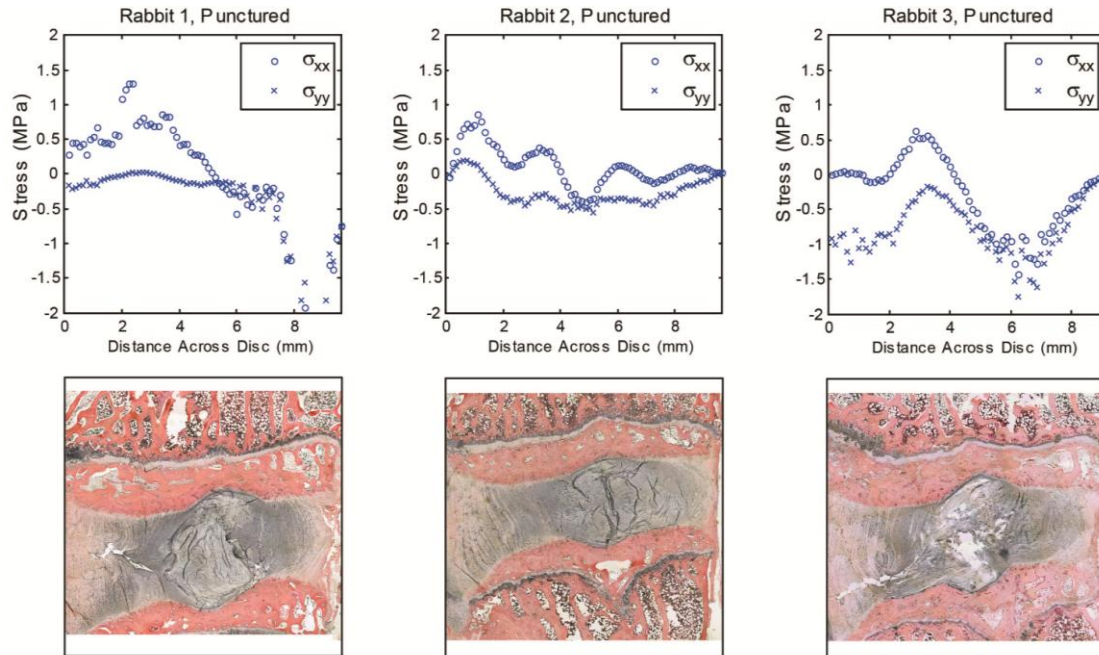
Figure 4.8: Stresses in the axial and transverse directions were plotted as a function of transverse distance across a middle plane of the disc for each of the punctured specimens (top). These profiles were then compared to histology of each disc (bottom) to compare local stress behavior to the disc anatomy. In the punctured discs, the nucleus regions were observed to be more fibrous than in the paired, adjacent discs, and the associated stress profiles did not demonstrate consistent patterns indicative of clearly defined nucleus and annulus regions.

Material parameter estimates calculated by the model were typically highest at the center of the disc and decreased with radial distance (Figure 4.9). Estimates of the Neo-Hookean material parameter c_1 at the center of the untreated discs were between 1.5 and 2 times that of the value estimated in the AF, however there was no such discernible pattern in the punctured discs (Table 4.1). In addition, punctured discs tended to have lower peak material constant values in the NP than were estimated in the paired adjacent discs. The specimen displaying the highest degree of degeneration, as well as large tears in the NP evident in histology, produced material parameter estimates that were lower in the region of the NP than in the surrounding AF.
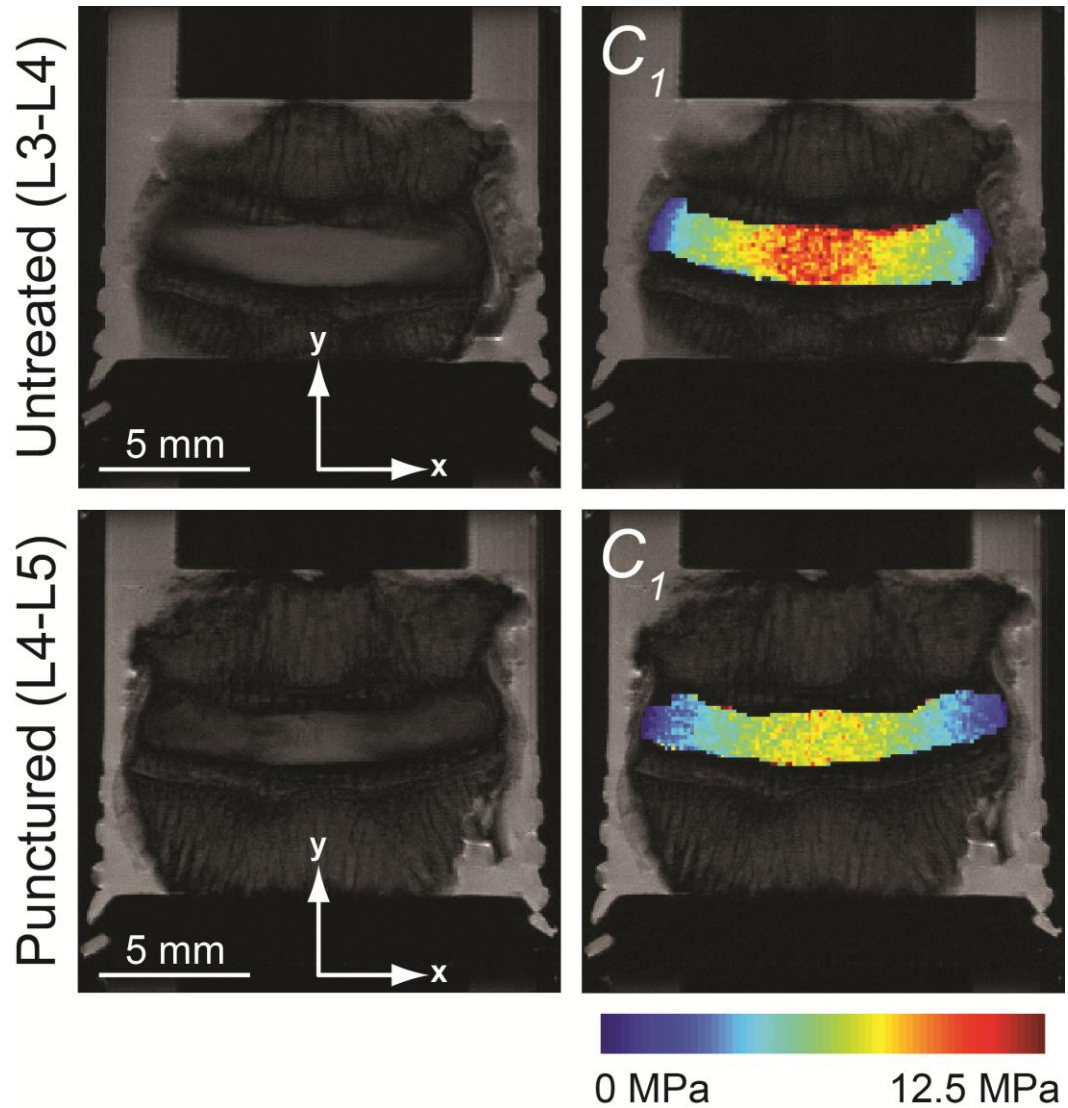
Figure 4.9: The Neo-Hookean material parameter c_1 was assumed to have a linear relationship to local glycosaminoglycan (GAG) content, measured by dGEMRIC. The parameter c_1, which is associated with material stiffness, was related to GAG with a scaling factor computed by the model such that all boundary and equilibrium conditions were satisfied. Neo-Hookean c_1 values were lower in two of the three discs subjected to annular puncture than in their matched, untreated discs, corresponding accordingly to a decrease in GAG content observed in the degenerated discs.

Table 4.1: The mean value of the Neo-Hookean constant, c_1, was calculated within the regions representing the nucleus pulposus (NP) and annulus fibrosus (AF) for each specimen. Values for the Neo-Hookean constant in both the NP and AF were lower in the punctured disc for two of the three rabbits.

	Rabbit 1		Rabbit 2		Rabbit 3	
	Untreated	Punctured	Untreated	Punctured	Untreated	Punctured
$c_{1,NP}$	1.34E+06	1.85E+06	9.27E+06	7.63E+06	5.46E+06	2.56E+06
$c_{1,AF}$	6.36E+05	2.90E+06	4.98E+06	4.37E+06	3.61E+06	2.20E+06

4.3.2. Model Verification by Finite Element Simulation

The computational model performed well in the estimation of material parameters, with estimates of 40.13 MPa for the interior region and 3.85 MPa for the exterior, as compared to the actual values of 40 MPa and 4 MPa input to the finite element simulation, respectively (Figure 4.10). Accordingly, errors in parameter estimation for the interior and exterior were 0.325% and 3.68%, respectively. NRMSE in stress estimates were below 1% across the entire interior region and below 2.1% across the exterior region (Table 4.2).

Table 4.2: Normalized root mean square error (NRMSE) was calculated in each direction to evaluate the accuracy of stress estimation between the predicted stresses of the FSD model and those generated by finite element simulation for both the interior and exterior regions of the validation model.

	NRMSE (%)	
	Interior	Exterior
σ_{11}	0.91	2.09
σ_{22}	0.45	1.61
σ_{12}	0.04	0.62
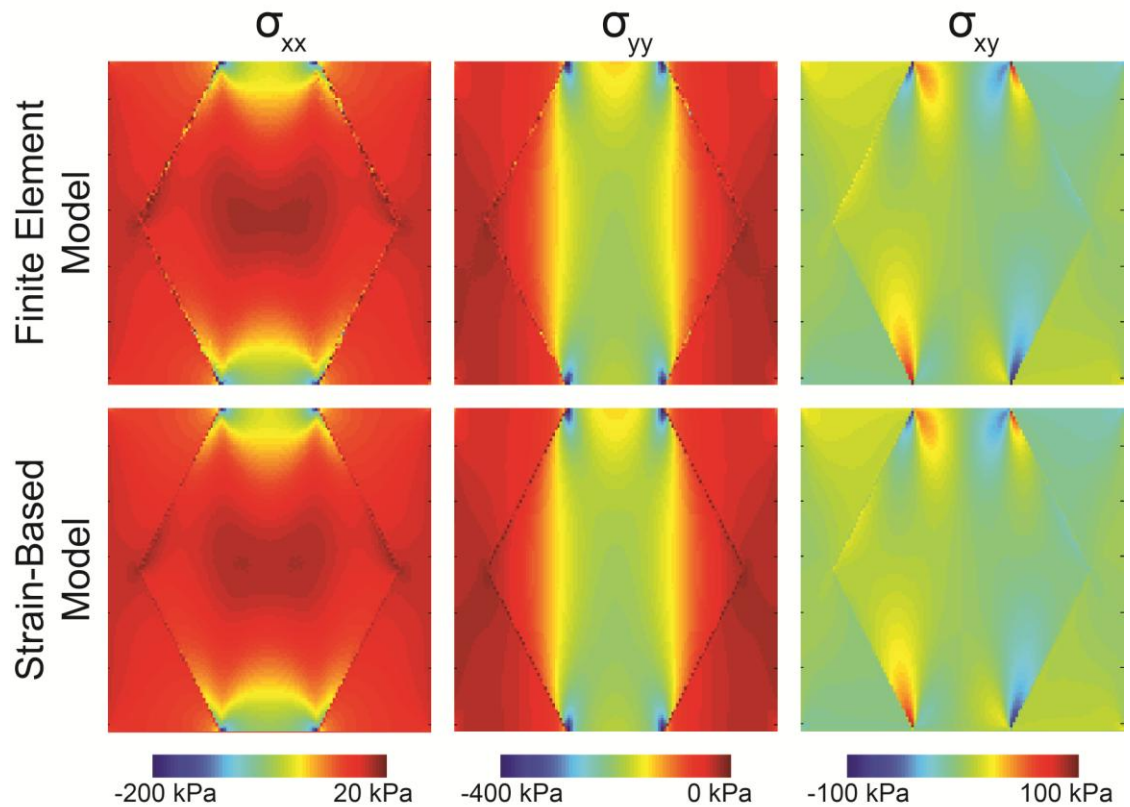
Figure 4.10: The FSB model was validated using finite element analysis simulations. Stress fields were generated by finite element analysis for a two-material body subjected to a compressive vertical load of 1000 N/m. The corresponding strains were then used as inputs to the FSB model used in the intervertebral disc analysis. Here, the simulated and computed stress fields are shown. The strain-based model estimated material parameters of 40.13 MPa for the interior region and 3.85 MPa for the exterior, while the true values input to the finite element simulatoin were 40.00 MPa and 4.00 MPa, respectively.

4.4. <u>Discussion</u>

In this chapter, a computational method for the noninvasive mechanical analysis of the IVD was developed. Stresses were estimated for both the AF and NP, as were material parameters for each region as a function of local biochemical composition. Stresses were within a range reasonable for the magnitude of loading and size of the discs. Strong agreement in results was found in the validation study comparing model predictions to known stress fields produced by finite element simulation, confirming proper implementation of the modeling methods.

A well-defined region with behavior similar to that expected of the NP was observed in the majority of untreated discs, characterized by a central region of compressive stress of the same shape and size in both the axial and radial directions. This region was observed to be less well-defined or nonexistent in the punctured discs. These results corresponded well with observations of NP size and integrity made from histological images of the discs. Estimates for material constants within the NP of the untreated discs were higher than those of the punctured discs, a result that agrees well with direct measurements of healthy and degenerated NP in other studies [91].

A potential limitation of the models is the use of a single plane, two-dimensional model for the system, which requires minimal out-of-plane motion. If a disc were to experience out-of-plane loading, the assumptions of the model would be violated and make it difficult to reach any conclusions about the state of degeneration or material properties associated with the system. Only discs with displacements indicating near-uniform compression were analyzed in this study in order to minimize such difficulties, but such influences are difficult to entirely eliminate. The consideration of multiple planes and measures of out-of-plane displacements in future work will require three dimensional dualMRI-based displacement measurements. While these are time consuming, they are likely to decrease errors in measured and modeled data.

The incorporation of a linear relationship between GAG content and local mechanical stiffness could potentially be further improved upon for a refinement in the model. However, the relationship allows for a reasonable approximation of heterogeneous and biochemically-dependent properties and relates well to linear correlations in the literature [90]. Given the fibrous and highly oriented nature of the AF, the addition of anisotropic constitutive relations in the AF may lead to further advancement in future work [5].

The methods developed in this chapter demonstrate the ability to noninvasively assess the mechanics of the IVD and, consequently, the physical health of the disc through visualization of the stress state during a known applied load. The techniques demonstrated here show potential towards the analysis of disc degeneration in a clinical setting, where the evaluation of stress distributions and concentrations may lead to improved early diagnostic capabilities not possible with current techniques.

CHAPTER 5. PRINCIPLES OF MIXTURE THEORY

5.1. Introduction

In order to more fully describe the complex interactions of biomaterials with distinct solid and fluid constituents, such as cartilage and intervertebral discs, the modeling techniques previously described will be extended by the incorporation of mixture theory principles. While nonlinear models for a single continuum provide a good approximation for many biological materials, mixture theory allows for a more complete description of the interactions within solid-fluid composites, including motion of free water within the system and effects due to the permeability and diffusivity of the solid.

5.2. Theory

In the following equations, a material structure is defined in terms of a solid component (s) and fluid component (f). Both components have an associated true density, ρ_T^α, and volume fraction, ϕ^α, where α refers to components s or f. The volume fraction of each may be defined in terms of the volume of the component, V^α, and the total volume of the mixture, V_T, by

$$\phi^\alpha = \frac{V^\alpha}{V_T}. \tag{5.1}$$

From this relation it follows that

$$\phi^s + \phi^f = 1. \tag{5.2}$$

The total mixture density, ρ, may be represented as the sum of the apparent densities of each component by

$$\rho = \rho^s + \rho^f, \tag{5.3}$$

where apparent density is defined by

$$\rho^\alpha = \rho_T^\alpha \phi^\alpha. \tag{5.4}$$

The principal of conservation of mass may be applied to the mixture, giving the relation

$$\sum_{\alpha=1}^{N} \left(\frac{D^\alpha \rho^\alpha}{Dt} + \rho^\alpha div \mathbf{v}^\alpha \right) = \sum_{\alpha=1}^{N} \hat{c}^\alpha = 0, \tag{5.5}$$

where $\mathbf{v}^\alpha$ is the velocity vector and $\hat{c}^\alpha$ is the rate of mass production for each component. As indicated by the above equation, the rate of mass production within the closed system is assumed to be negligible. Expanding the material derivative, $\frac{D^\alpha \rho^\alpha}{Dt}$, (5.5) becomes

$$\sum_{\alpha=1}^{N} \left(\frac{\partial \rho^\alpha}{\partial t} + \sum_{i=1}^{3} \frac{\partial \rho^\alpha}{\partial x_i} v_i^\alpha + \rho^\alpha div \mathbf{v}^\alpha \right) = 0. \tag{5.6}$$

Conservation of linear momentum for the mixture can be represented as

$$\sum_{\alpha=1}^{N} \rho^\alpha \frac{D^\alpha \mathbf{v}^\alpha}{Dt} = \sum_{\alpha=1}^{N} div \mathbf{T}^\alpha + \sum_{\alpha=1}^{N} (\rho^\alpha \mathbf{b}^\alpha + \boldsymbol{\pi}^\alpha), \tag{5.7}$$

where $\mathbf{T}^\alpha$ is a stress tensor, $\mathbf{b}^\alpha$ is the body force vector acting on the component, and $\boldsymbol{\pi}^\alpha$ represents an interaction force between components resulting from momentum transfer. This final term is given for the fluid component as

$$\boldsymbol{\pi}^f = -A_{f/s} \boldsymbol{\nabla} \frac{\phi^f}{\phi^s} + C_{f/s}(\mathbf{v}^s - \mathbf{v}^f), \tag{5.8}$$

where $A_{f/s}$ is a material constant that describes the motive force caused by diffusion and $C_{f/s}$ represents resistance due to drag. The relationship between the interaction force between the solid and fluid components is:

$$\pi^s = -\pi^f. \tag{5.9}$$

The balance of linear momentum for the individual components then becomes

$$\rho^s \frac{D^s \mathbf{v}^s}{Dt} = div\mathbf{T}^s + \phi^s \rho_T^s \mathbf{b}^s + A_{f/s} \nabla \frac{\phi^f}{\phi^s} + C_{f/s}(\mathbf{v}^f - \mathbf{v}^s), \tag{5.10}$$

$$\rho^f \frac{D^f \mathbf{v}^f}{Dt} = div\mathbf{T}^f + \phi^f \rho_T^f \mathbf{b}^f - A_{f/s} \nabla \frac{\phi^f}{\phi^s} - C_{f/s}(\mathbf{v}^f - \mathbf{v}^s). \tag{5.11}$$

Finally, the stress tensor for the mixture is the sum result of the stress tensors for each component. In symbolic form,

$$\mathbf{T} = \sum_{\alpha=1}^{N} \mathbf{T}^\alpha = \mathbf{T}^s + \mathbf{T}^f. \tag{5.12}$$

CHAPTER 6. APPLICATION AND VALIDATION OF A MIXTURE THEORY,
FINITE STRAIN-BASED MODEL OF AXISYMMETRIC AGAROSE GELS

6.1. Introduction

Effective analysis of soft, porous biomaterials is a central concept towards the development of an imaging-based modeling methodology to fully describe the complex mechanics of soft biological tissue during applied loading. In this chapter, methods are implemented for estimating stresses and material properties for a nonlinear material under mixture material assumptions. The implementation of these methods is verified by comparison to finite element simulation. Model material parameter estimates are then compared to those determined by unconfined compression measures. For the development and validation of this model, agarose gels were chosen as the material of interest. Agarose is a linear polymer that, in combination with water, can be used to form a porous gel structure that is most commonly used in gel electrophoresis [92, 93]. The porous solid and fluid structure, repeatable composition, and wide availability make it an ideal material for a first application of the mixture theory-based model.

6.2. Methods

6.2.1 Agarose Gel Preparation

Agarose gels of 2% concentration were prepared one day prior to data acquisition by thoroughly mixing 0.5 g of low melt agarose powder (Bio-Rad Laboratories, Inc; Hercules, CA) with 25 mL of 1X phosphate buffered saline (PBS). The solution was heated in a microwave in 5 second increments for approximately 20 seconds, or until the powder was fully dissolved, with the fluid gently swirled at each increment to ensure

uniformity. The heated solution was then poured into Petri dishes with a pipette to a final gel height of 5 mm. The gels were then allowed to cool to room temperature, then sealed and refrigerated until testing commenced to minimize fluid loss from the gel. A punch with inner diameter of 1 cm was used to slice the gels into uniform cylindrical samples just prior to testing.

6.2.2. Magnetic Resonance Imaging

Displacements and strain fields for 2% agarose gels were determined using dualMRI in a 14.0 Tesla MRI (Bruker GMBH, Ettlingen, Germany). The cylindrical samples were fixed to the Delrin base of the loading apparatus sample chamber with one drop of cyanoacrylate, and kept submerged in 1X PBS throughout the duration of loading. The gels were subjected to a cyclic compressive load of approximately 0.125 N with a 1.27 cm diameter spherical Delrin indenter for a period of 1.5 seconds, with a total cycle length of 3.0 seconds. Displacements were then measured in the axial and radial directions of an imaging plane through the center of the gel. A steady-state load-displacement response was achieved after 50 cycles, following which imaging commenced. Imaging parameters were: repetition time = 3000 milliseconds, echo time = 1.85 milliseconds, field of view = 25.6×25.6 mm^2, matrix size = 256×256, slice thickness = 1.5 mm. The deformation gradient and strains were then computed as before.

6.2.3. Computational Analysis of Agarose Gels

Due to the symmetry of the geometry and loading conditions, knowledge of the in-plane loading deformation response is adequate to describe the stress state of the sample volume. Therefore, a cylindrical coordinate system was employed in this analysis with axial symmetry assumptions. With this change of coordinates, the deformation gradient is now written as

$$\mathbf{F} = \begin{bmatrix} \frac{\partial u_r}{\partial r} + 1 & \frac{1}{r}\frac{\partial u_r}{\partial \theta} - \frac{u_\theta}{r} & \frac{\partial u_r}{\partial z} \\ \frac{\partial u_\theta}{\partial r} & \frac{1}{r}\frac{\partial u_\theta}{\partial \theta} + \frac{u_r}{r} + 1 & \frac{\partial u_\theta}{\partial z} \\ \frac{\partial u_z}{\partial r} & \frac{1}{r}\frac{\partial u_z}{\partial \theta} & \frac{\partial u_z}{\partial z} + 1 \end{bmatrix}. \tag{6.1}$$

Next, the equation for conservation of mass, given by

$$\sum_{\alpha=1}^{N} \left(\frac{\partial \rho^\alpha}{\partial t} + \sum_{i=1}^{3} \frac{\partial \rho^\alpha}{\partial x_i} v_i^\alpha + \rho^\alpha div\mathbf{v}^\alpha \right) = 0, \tag{6.2}$$

may be expanded and written in cylindrical coordinates as

$$\sum_{\alpha=1}^{N} \left(\frac{\partial \rho^\alpha}{\partial r} v_r^\alpha + \frac{1}{r}\frac{\partial \rho^\alpha}{\partial \theta} v_\theta^\alpha + \frac{\partial \rho^\alpha}{\partial z} v_z^\alpha + \rho^\alpha \frac{\partial v_r^\alpha}{\partial r} + \rho^\alpha \frac{v_r^\alpha}{r} + \frac{1}{r}\rho^\alpha \frac{\partial v_\theta^\alpha}{\partial \theta} + \rho^\alpha \frac{\partial v_z^\alpha}{\partial z} \right) = 0. \tag{6.3}$$

The time-dependent term $\frac{\partial \rho^\alpha}{\partial t}$ is assumed negligible here due to the quasi-static loading condition.

Similarly, assuming negligible acceleration due to the quasi-static loading state, negligible effects due to diffusion, and limited effects of gravity or other body forces, the equations for conservation of linear momentum,

$$\rho^s \frac{D^s \mathbf{v}^s}{Dt} = div\mathbf{T}^s + \phi^s \rho_T^s \mathbf{b}^s + A_{f/s}\boldsymbol{\nabla}\frac{\phi^f}{\phi^s} + C_{f/s}(\mathbf{v}^f - \mathbf{v}^s), \tag{6.4}$$

$$\rho^f \frac{D^f \mathbf{v}^f}{Dt} = div\mathbf{T}^f + \phi^f \rho_T^f \mathbf{b}^f - A_{f/s}\boldsymbol{\nabla}\frac{\phi^f}{\phi^s} - C_{f/s}(\mathbf{v}^f - \mathbf{v}^s), \tag{6.5}$$

may be expanded in cylindrical coordinate form for the solid component as

$$\frac{\partial T_{rr}^s}{\partial r} + \frac{1}{r}\frac{\partial T_{r\theta}^s}{\partial \theta} + \frac{\partial T_{rz}^s}{\partial z} + \frac{T_{rr}^s - T_{\theta\theta}^s}{r} + C_{f/s}(v_r^f - v_r^s) = 0, \tag{6.6}$$

$$\frac{\partial T_{r\theta}^s}{\partial r} + \frac{1}{r}\frac{\partial T_{\theta\theta}^s}{\partial \theta} + \frac{\partial T_{\theta z}^s}{\partial z} + \frac{2T_{r\theta}^s}{r} + C_{f/s}(v_\theta^f - v_\theta^s) = 0, \tag{6.7}$$

$$\frac{\partial T_{rz}^s}{\partial r} + \frac{1}{r}\frac{\partial T_{\theta z}^s}{\partial \theta} + \frac{\partial T_{zz}^s}{\partial z} + \frac{T_{rz}^s}{r} + C_{f/s}\left(v_z^f - v_z^s\right) = 0. \tag{6.8}$$

Similarly, for the fluid component,

$$\frac{\partial T_{rr}^f}{\partial r} + \frac{1}{r}\frac{\partial T_{r\theta}^f}{\partial \theta} + \frac{\partial T_{rz}^f}{\partial z} + \frac{T_{rr}^f - T_{\theta\theta}^f}{r} - C_{f/s}\left(v_r^f - v_r^s\right) = 0, \tag{6.9}$$

$$\frac{\partial T_{r\theta}^f}{\partial r} + \frac{1}{r}\frac{\partial T_{\theta\theta}^f}{\partial \theta} + \frac{\partial T_{\theta z}^f}{\partial z} + \frac{2T_{r\theta}^f}{r} - C_{f/s}\left(v_\theta^f - v_\theta^s\right) = 0, \tag{6.10}$$

$$\frac{\partial T_{rz}^f}{\partial r} + \frac{1}{r}\frac{\partial T_{\theta z}^f}{\partial \theta} + \frac{\partial T_{zz}^f}{\partial z} + \frac{T_{rz}^f}{r} - C_{f/s}\left(v_z^f - v_z^s\right) = 0. \tag{6.11}$$

The solid component is modeled here as a homogeneous, compressible Neo-Hookean solid, described by the strain energy density function

$$W = c_1\left(J^{-2/3}I_1 - 3\right) + c_2(J-1)^2, \tag{6.12}$$

where c_1 and c_2 are Neo-Hookean material parameters, J is the determinant of the deformation gradient $\boldsymbol{F}$, and I_1 is the first invariant given by

$$I_1 = \text{tr}\boldsymbol{C}. \tag{6.13}$$

The Second Piola-Kirchhoff stress is:

$$\boldsymbol{S} = 2\sum_i \frac{\delta W}{\delta I_i}\frac{\delta I_i}{\delta \boldsymbol{C}} = 2\left[c_1 J^{-2/3}\left(\boldsymbol{I} - \frac{1}{3}(\text{tr}\boldsymbol{C})\boldsymbol{C}^{-1}\right) + c_2 J(J-1)\boldsymbol{C}^{-1}\right], \tag{6.14}$$

where $\boldsymbol{I}$ is the identity tensor.

The first Piola Kirchoff stress, $\boldsymbol{P}$, is then determined by the relation $\boldsymbol{P}=\boldsymbol{FS}$.

The fluid component at each voxel is modeled as a hydrostatic pressure, given by

$$\mathbf{T}^f = -p\mathbf{I} = \begin{bmatrix} -p & 0 & 0 \\ 0 & -p & 0 \\ 0 & 0 & -p \end{bmatrix},$$

(6.15)

where $\mathbf{I}$ is the identity tensor. Due to the quasi-static nature of the load-displacement response, the fluid pressure was assumed to be near constant throughout the volume of the samples.

The precise fluid volume fraction of the gels was unknown. For the purposes of the model, the volume fraction was varied from 0.86 to 0.94 in 0.02 increments [94]. The unknown material parameters c_1, c_2, and p were solved for each half plane system using a nonlinear least squares fit of the parameters to the equilibrium equations of the system with a solution convergence tolerance of 1e-7.

6.2.4. Model Verification by Finite Element Simulation

Similar to previous chapters, the mathematical implementation of the axially symmetric model was verified using displacement fields artificially generated by finite element simulation as inputs to the model. This in turn allowed for a direct assessment of mathematical error in material property estimation. COMSOL was used once again to generate an axially symmetric simulation of a cylinder 5 mm high and with radius of 5 mm – identical to the geometry of the agarose samples.

A compressible Neo-Hookean material model was implemented for the simulation, with arbitrary material parameters of $c_1 = 2.5$ MPa and $c_2 = 43$ MPa selected as simulation inputs. The simulated material was subjected to a compressive strain of 5% by applying a displacement of 0.25 mm to the top boundary in the negative z-direction. The left boundary was constrained by an axial symmetry condition, the bottom boundary was constrained to zero displacement in the z-direction, and the right boundary was free to deform in the r-direction. A tetrahedral mesh was used in the simulation with 3920 elements and 23883 degrees of freedom.

Displacement fields generated by the simulation as a result of the loading condition were exported as 256×256 grids and used as inputs to the computational finite strain-based model. The error in material parameter estimates computed by the finite strain-based model to the actual parameter values used in the COMSOL simulation was then calculated.

6.2.5. Experimental Fitting of Agarose Gel Material Parameters

Material parameters of the agarose gels were calibrated from experimental measurements as a means of evaluating the accuracy of parameter estimation by the finite strain-based model. Unconfined compression tests were performed on the 2% agarose gel samples. The gels were compressed in increments of 2.5% nominal strain to 30% nominal compression, with a hold time of 5 minutes between increments [95].

The gels were compressed with a 1.27 cm diameter, flat cylindrical indenter attached to a linear motor. The forces experienced by the gels during compression were measured with a 1000 g load cell. Cylindrical gel samples of 2% agarose were made for the experiments as previously described, except in this case two drops of India ink was added to the solution. The addition of the dye was employed to improve the visibility of the gel for purposes of tracking radial expansion. The samples were centered on a Delrin platform directly beneath the cylindrical indenter (Figure 6.1), and mineral oil was used to lubricate both the Delrin platform and indenter to reduce friction between the surfaces and the gel. Prior to testing, the indenter was lowered until just touching the top surface of the gel. Displacement of the gels in the z-direction was measured by the displacement of the indenter, while strain in the r-direction was monitored using photos taken at multiple time points during the test. Changes in sample diameter were then determined after testing by measuring the change in dimensions in Photoshop.
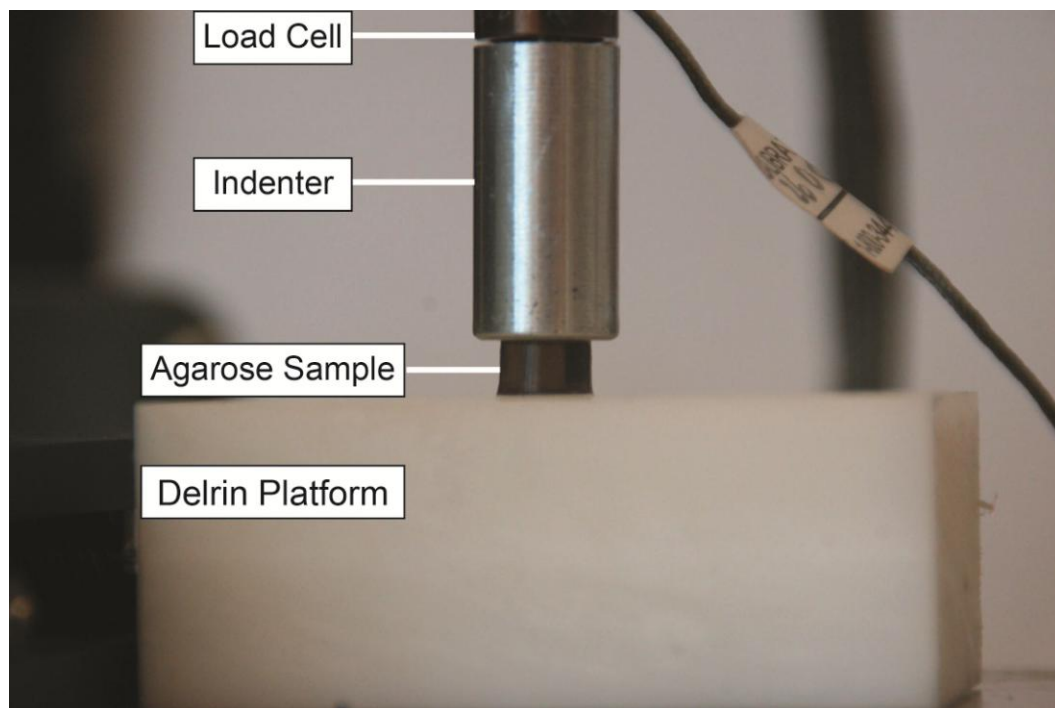
Figure 6.1: Unconfined compression tests were performed on 2% agarose gel samples. The gels were compressed in increments of 2.5% nominal strain to 30% nominal compression, with a hold time of 5 minutes between increments. A 1000 g load cell measured the force-displacement response of the gels over time.

Prior to measurement, the gels were cyclically compressed to 10% nominal strain for 50 cycles to approximate the conditions required to meet a steady-state load-displacement response during the MRI experiments. The cycle duration was the same as that during MRI acquisition, with a 1.5 second load duration and total cycle length of 3.0 seconds. Stress parameters were evaluated for the gels using displacement and force measurements 1.5 seconds after initial compression to correspond to the 1.5 second loading time of the gels during MRI acquisition. As before, the solid components of the gels were assumed to behave as compressible Neo-Hookean materials. Under uniaxial compression assumptions, the deformation gradient of the sample experiencing loading may be written as

$$F = \begin{bmatrix} \lambda_1 & 0 & 0 \\ 0 & \lambda_2 & 0 \\ 0 & 0 & \lambda_3 \end{bmatrix}, \tag{6.16}$$

where λ_1, λ_2, and λ_3 are the principal stretches in each direction. The determinant of the deformation gradient is then $\det F = J = \lambda_1 \lambda_2 \lambda_3$. As a result, the right Cauchy-Green deformation tensor becomes

$$C = \begin{bmatrix} \lambda_1^2 & 0 & 0 \\ 0 & \lambda_2^2 & 0 \\ 0 & 0 & \lambda_3^2 \end{bmatrix}. \tag{6.17}$$

The inverse of the right Cauchy-Green deformation tensor is then

$$C^{-1} = \begin{bmatrix} \lambda_1^{-2} & 0 & 0 \\ 0 & \lambda_2^{-2} & 0 \\ 0 & 0 & \lambda_3^{-2} \end{bmatrix}, \tag{6.18}$$

and the trace is

$$\text{tr}C = \lambda_1^2 + \lambda_2^2 + \lambda_3^2. \tag{6.19}$$

Solving for the Second Piola-Kirchhoff stress of equation (6.14), the non-zero stress components become:

$$S_{11} = \frac{2}{3} c_1 (\lambda_1 \lambda_2 \lambda_3)^{-2/3} (2 - \lambda_1^{-2} \lambda_2^2 - \lambda_1^{-2} \lambda_3^2) + 2c_2 (\lambda_2^2 \lambda_3^2 - \lambda_1^{-1} \lambda_2 \lambda_3), \tag{6.20}$$

$$S_{22} = \frac{2}{3} c_1 (\lambda_1 \lambda_2 \lambda_3)^{-2/3} (2 - \lambda_1^2 \lambda_2^{-2} - \lambda_2^{-2} \lambda_3^2) + 2c_2 (\lambda_1^2 \lambda_3^2 - \lambda_1 \lambda_2^{-1} \lambda_3), \tag{6.21}$$

$$S_{33} = \frac{2}{3} c_1 (\lambda_1 \lambda_2 \lambda_3)^{-2/3} (2 - \lambda_1^2 \lambda_3^{-2} - \lambda_2^2 \lambda_3^{-2}) + 2c_2 (\lambda_1^2 \lambda_2^2 - \lambda_1 \lambda_2 \lambda_3^{-1}). \tag{6.22}$$

Using the relation **P=FS,** the First Piola-Kirchhoff stresses for the solid are then determined from (6.20), (6.21), and (6.22) to be:

$$P_{11} = \phi^s \left(\frac{2}{3} c_1 (\lambda_1 \lambda_2 \lambda_3)^{-2/3} (2\lambda_1 - \lambda_1^{-1}\lambda_2^2 - \lambda_1^{-1}\lambda_3^2) + 2c_2(\lambda_1\lambda_2^2\lambda_3^2 - \lambda_2\lambda_3) \right), \qquad (6.23)$$

$$P_{22} = \phi^s \left(\frac{2}{3} c_1 (\lambda_1 \lambda_2 \lambda_3)^{-2/3} (2\lambda_2 - \lambda_1^2\lambda_2^{-1} - \lambda_2^{-1}\lambda_3^2) + 2c_2(\lambda_1^2\lambda_2\lambda_3^2 - \lambda_1\lambda_3) \right), \qquad (6.24)$$

$$P_{33} = \phi^s \left(\frac{2}{3} c_1 (\lambda_1 \lambda_2 \lambda_3)^{-2/3} (2\lambda_3 - \lambda_1^2\lambda_3^{-1} - \lambda_2^2\lambda_3^{-1}) + 2c_2(\lambda_1^2\lambda_2^2\lambda_3 - \lambda_1\lambda_2) \right). \qquad (6.25)$$

The fluid component was again modeled as a hydrostatic pressure term as given in (6.15).

The coordinate axes were oriented with the 3-direction aligning with the direction of loading. The First Piola-Kirchhoff stresses relate forces in the deformed configuration to areas in the reference configuration. From this, P_{33} could be determined using the measured forces and the reference area of the samples. A least squares fit was used to determine the parameters c_1 and c_2 that minimized error between the experimental force data and the loading conditions calculated by the compressible Neo-Hookean stress-strain model to within a tolerance of 1e-7. Error between these values and those predicted by the finite strain-based model were then calculated.

6.2.6. Sensitivity Analysis

The sensitivity of the model to variations in inputs was tested using Cotter's Method. In this design, input parameters that may influence the output of the model are identified, with a low value and a high value considered for each parameter. The simulation is then run once with all factors at their upper levels, once with all factors at their lower levels, once for each factor at its upper level while the other factors are maintained at their lower levels, and finally once with each factor at its lower level while the other factors are

maintained at their higher levels. The impact of each factor was then calculated by comparing the sensitivity factor, S_c, for each parameter, given by

$$S_c(j) = \frac{M(j)}{\sum_{j=1}^{n_p} M(j)},$$

(6.26)

where n_p is the number of independent variables, and $M(j)$ is

$$M(j) = |C_o(j)| + |C_e(j)|.$$

(6.27)

The terms $C_o(j)$ and $C_e(j)$ are then:

$$C_o(j) = \frac{1}{4}[(y_H - y_{j,L}) + (y_{j,H} - y_L)],$$

(6.28)

$$C_e(j) = \frac{1}{4}[(y_H - y_{j,L}) - (y_{j,H} - y_L)],$$

(6.29)

where y_H is the output with all parameters high, $y_{j,L}$ is the output with parameter j low and all others high, $y_{j,H}$ is the output with parameter j high and all others low, and y_L is the output with all parameters low.

The primary inputs to the MRI-based model are the applied loading condition, the measured displacements, and the assumed volume fraction. Therefore, the sensitivity analysis focused on possible variations in these three parameters. The influence of potential variation in load was investigated by varying the loading condition to the model by ±5%. Meanwhile, variation in the displacement fields used as inputs is primarily affected by the number of smoothing cycles implemented during processing of the raw MRI data. In the primary model, 25 smoothing cycles was used to process the displacement data. For the purposes of the sensitivity analysis, displacements processed with 10 and 25 smoothing cycles were used for the low and high parameter values, respectively. Finally, the volume fraction of the fluid input to the model was varied by

±4% to span a common range reported for similar gels [94]. These factors and the sequence of evaluation are summarized in Table 6.1 and Table 6.2.

Table 6.1: Cotter's Method was used to evaluate the sensitivity of the finite strain-based model outputs to changes in model inputs. The inputs evaluated were the applied loading condition, the number of smoothing cycles used during processing of the displacement data, and the fluid volume fraction of the gel (ϕ^f). Sensitivity was evaluated by running the model at alternately low- and high-end values for the inputs identified.

	FSB Model Value	Low Value	High Value
Load (N)	0.125	0.119	0.131
Smoothing Cycles	25	10	25
ϕ^f	0.9	0.86	0.94

Table 6.2: Summary of the model evaluations performed in the Cotter's sensitivity analysis. In this table, (ϕ^f) is the fluid volume fraction of the gel, "H" indicates that the high-end value of the given input was used in the model, and "L" indicates that the low-end value was used.

Test Number	1	2	3	4	5	6	7	8
Load	H	L	H	H	H	L	L	L
Smoothing Cycles	H	H	L	H	L	H	L	L
ϕ^f	H	H	H	L	L	L	H	L

6.3. <u>Results</u>

6.3.1 Magnetic Resonance Imaging

Displacements in the agarose gels appeared roughly symmetric with respect to the axis of loading. As expected, the largest displacement occurred in the region adjacent to the indenter and decreased with radial distance (Figure 6.2).
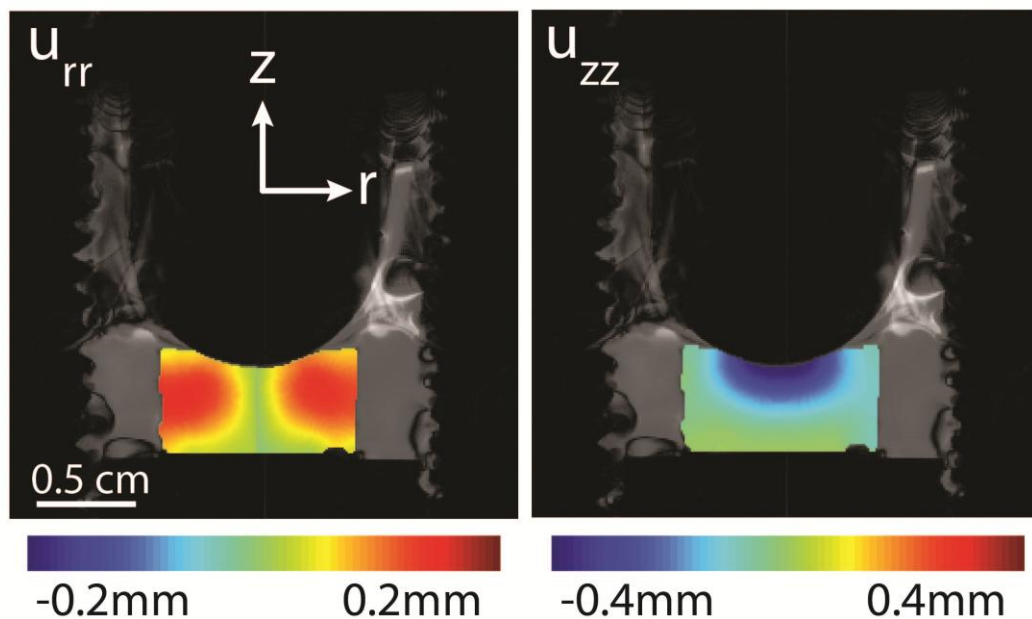
Figure 6.2: Displacements were measured within 2% agarose gels subjected to axial compression by a spherical indenter. Displacements in the loading (z) and radial (r) directions were approximately symmetric about the central axis, with some small off-axis deformation observed in the radial direction for a portion of the samples.

The gels exhibited regions of large compressive strains in the direction of loading below the area of surface contact with the indenter (Figure 6.3). Maximum compressive strain in the gels was found to be 14%. These regions are complemented by areas of positive

strains in the radial direction. Strains in the radial direction typically peaked at a value of approximately 7%. Shear strains were also exhibited throughout the gel during the loading phase. The highest shear strain was found to occur at the gel interface with the indenter, indicating the presence of surface friction at the area of contact.
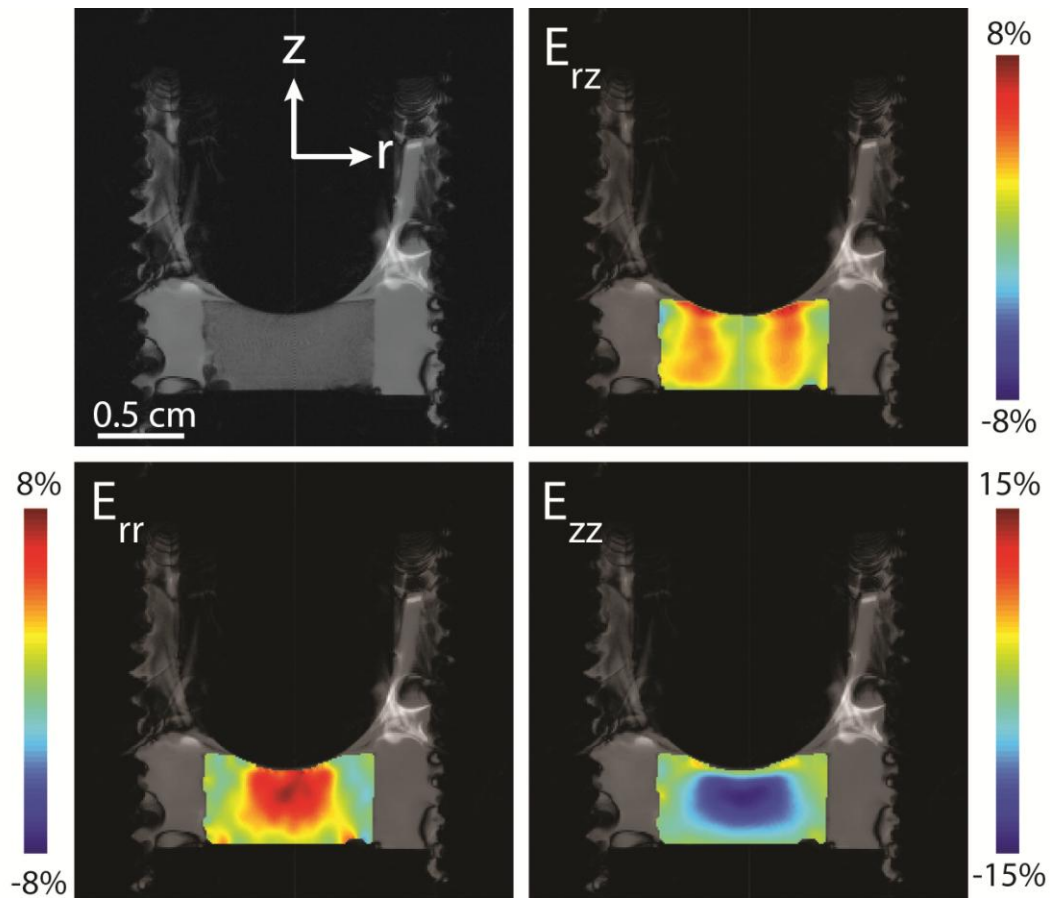
Figure 6.3: Strain fields were calculated for each sample. The largest strains in the loading (*z*) direction were 14% compression. Highest strain was observed in the region of the gel directly beneath the applied load. Shear strains were at a maximum at the indenter surface interface, indicating the presence of friction shear forces at the surface.

6.3.2 Computational Analysis of Agarose Gels

Neo-Hookean parameters estimated by the finite strain-based model ranged from 23.4 kPa to 48.4 kPa for parameter c_1, and from 59.4 kPa to 110.0 kPa for parameter c_2 (Table 6.3). For both parameters, the results increased with the value of assumed fluid volume fraction. Parameter c_2 had the largest variance in results across samples, with the standard deviation reaching as high as 42% of the mean for a given fluid volume fraction. Parameter c_1 was slightly more consistent across samples, with the highest standard deviation found to be 27% of the mean value.

Table 6.3: Neo-Hookean parameters calculated for a range of agarose gel fluid volume fractions (mean ± standard deviation). Parameter estimates were found to increase with increasing fluid content.

ϕ^f	0.86	0.88	0.9	0.92	0.94
c_1 (kPa)	23.4 ± 5.6	27.5 ± 7.4	32.2 ± 8.0	38.0 ± 6.6	48.4 ± 9.7
c_2 (kPa)	59.4 ± 22.5	69.7 ± 29.3	77.9 ± 24.6	87.2 ± 25.9	110.0 ± 30.3

Unsurprisingly, the region of highest stress within the gels was found to occur in the direction of loading, with compressive stresses developing in the region of the gel below the indenter contact region (Figure 6.4). These compressive stresses peaked at a value of approximately 5 kPa. Stresses in the radial and out of plane directions were similar in shape and magnitude, with compressive stresses reaching a maximum value of approximately 2 kPa. Shear stresses within the gel were highest near the indenter contact surface where stresses reached 0.7 kPa. Half of the samples exhibited stresses that were slightly higher towards one half of the sample, suggesting that loading was not purely in the z-direction for those samples.
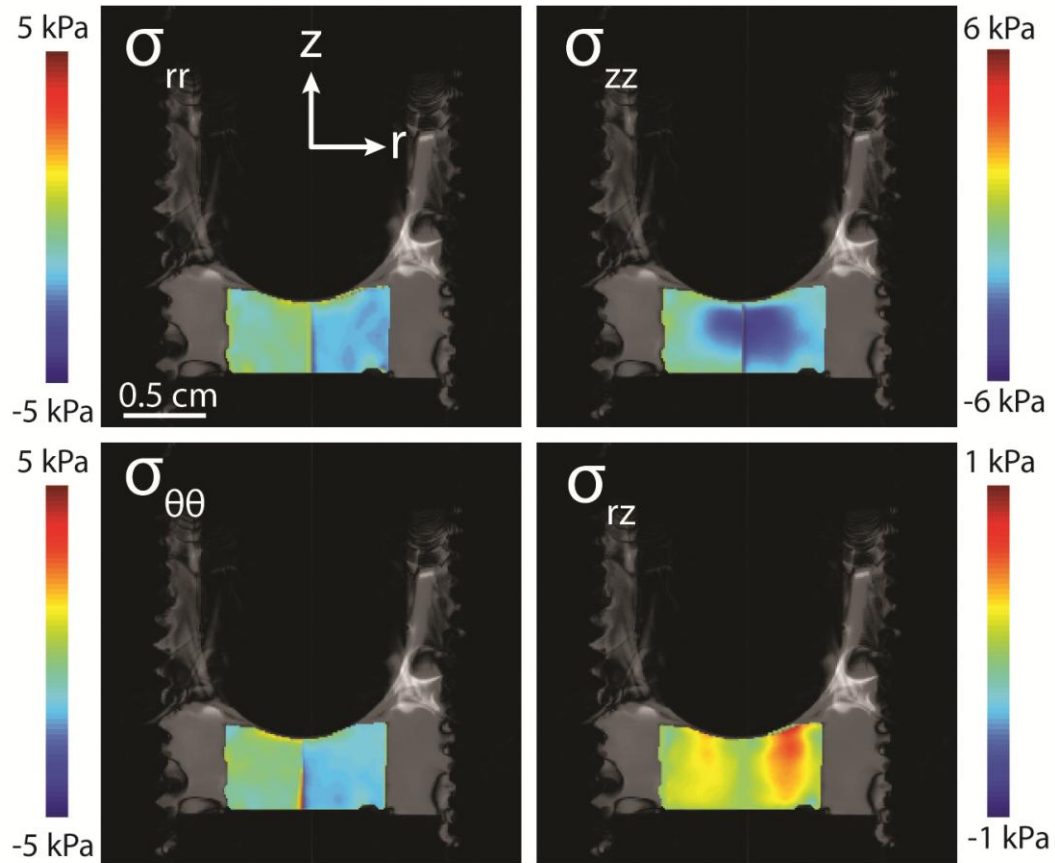
Figure 6.4: Stress fields were calculated for the axisymmetric model. Compressive stresses as high as 5 kPa were estimated in the loading direction. Shear stresses were found to be highest in the gel near the indenter surface interface.

6.3.3. Model Verification by Finite Element Simulation

The finite strain-based model did well in estimating the material parameters that were used in the finite element simulation. The strain-based model estimated that parameters of 2.52 MPa for c_1, and 43.34 MPa had been used as inputs to the simulation, as compared to the actual values of 2.5 MPa and 43 MPa. The resulting error in these parameter estimates to the known values of the finite element simulation was therefore 0.80% and 0.79%, respectively.

6.3.4. Experimental Fitting of Agarose Gel Material Parameters

A time-dependent stress response was measured in the agarose gels, as compressive forces decreased over the period of applied loading and approached a steady response over time (Figure 6.5). Damage to the gel structure was observed to occur in the gels after 20% nominal strain. As such, compression data at 15% nominal strain and below was used for the purposes of parameter fitting.
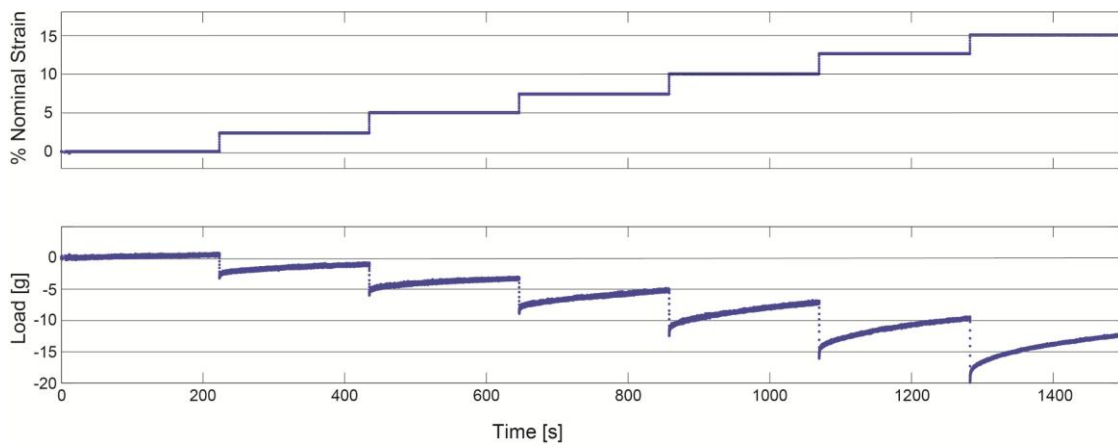
Figure 6.5: Preconditioned agarose gels were compressed in increments of 2.5% nominal strain over periods of 5 minutes per increment. The load response is shown here for nominal strain values from 0-15%, similar in magnitude to the strains measured in the gels.

The curve-fit Neo-Hookean parameters for the gels ranged from 21.7 kPa to 50.6 kPa for parameter c_1, and from 40.9 kPa to 95.5 kPa for parameter c_2 (Table 6.4). As with the finite strain-based model, the results increased with increasing assumed fluid volume fraction.

Table 6.4: Neo-Hookean parameter fitting results in 2% agarose gels in unconfined compression for varying fluid volume fraction.

ϕ^f	0.86	0.88	0.9	0.92	0.94
c_1 (kPa)	21.7	25.3	30.4	38.0	50.6
c_2 (kPa)	40.9	47.7	57.3	71.6	95.5

Percent error was calculated between the parameters determined by the finite strain-based model and those determined by fitting to unconfined compression measures. Calculations of c_1 matched most closely, with a high error of 8.65% and a low error of 0.01%. Calculations of c_2 were more disparate, with a high error of 46.07% and a low error of 14.77% (Table 6.5).

Table 6.5: Percent error in parameter estimation between the finite strain-based model and parameter fitting to unconfined compression measures.

ϕ^f	0.86	0.88	0.9	0.92	0.94
c_1 (%)	8.03	8.65	5.95	0.01	4.33
c_2 (%)	45.07	46.07	35.96	21.72	14.77

6.3.5. Sensitivity Analysis

Results of the sensitivity model showed a similar degree of sensitivity in the model to both the loading condition input to the model and to the number of smoothing cycles used in the processing of the displacement data (Table 6.6). The sensitivity factors for parameter c_1 were 0.38 and 0.44 for the loading condition and smoothing, respectively.

Similarly, for parameter c_2 the sensitivity factors were 0.42 and 0.43 for loading and smoothing, respectively. Little sensitivity was found to the fluid volume fraction for the range of values input to the model, with sensitivity factors of 0.18 for c_1 and 0.14 for c_2.

Table 6.6: Summary of sensitivity of output parameters to model inputs (mean ± standard deviation).

	Output Parameters	
	c_1	c_2
S_{Load}	0.38 ± 0.07	0.42 ± 0.06
$S_{Smoothing}$	0.44 ± 0.10	0.43 ± 0.06
$S_{\phi f}$	0.18 ± 0.04	0.14 ± 0.12

6.4. Discussion

In this chapter, material parameters and stresses were estimated in agarose gels experiencing an applied axial load. The resulting stress fields indicated behavior expected of spherical indentation, with a region of high compressive stress in the center of the gels below the indenter. Shear stresses at the interface between gel and indenter indicated the presence of surface friction during the loading process.

Non-symmetry within the samples indicates that a small radial load may have occurred during cyclic loading. A slight bend was found to exist in the pushrod, which may have resulted in a small radial force being exerted on the samples as the rod passed through the sleeve bearing of the loading apparatus. This imperfection might explain some of the variation in model results, particularly between halves of the same sample.

The results of the validation study suggest reasonable agreement between model parameter estimations and those determined by curve fitting to experimental compression

data. The error between the two methods was within 10% for Neo-Hookean parameter c_1, and within 50% for parameter c_2. While parameter estimations agree well over the experimental period of applied loading, the quasi-static assumptions necessary from the conditions of the MR data acquisition do not necessarily provide a description of the entire time-dependent relaxation response. For systems where, for example, a predictive model at varying strain rates is desired, it may be useful in some systems to acquire additional data sets under varying, prolonged loading conditions.

A potential source for error in results lies in the loading condition input to the model. Because of the level of relatively low force applied in the MRI experiments, and with the discovery of the slight bend in the pushrod, influences due to friction or other factors have the potential for greater impact. Because of this, forces required to achieve the observed displacement of the samples with a spherical indenter were measured again after experimentation to ensure the loading condition used in the models was as accurate as possible.

The sensitivity analysis performed on the models resulted in the conclusion that the model was equally sensitive to both changes in the applied load input to the model, and to the number of smoothing cycles. Variation in the third parameter, fluid volume fraction, was not found to have as large an impact on results for the range of values used. This reinforces the conclusion that fluctuation in the applied loading condition could lead to a potential source of error in results.

CHAPTER 7. FINITE STRAIN-BASED MODELING OF THE HUMAN
INTERVERTEBRAL DISC WITH MIXTURE THEORY MATERIAL
ASSUMPTIONS

7.1. Introduction

The primary goal of noninvasive, finite strain-based modeling techniques is the
nondestructive analysis of soft biological systems, both solid and porous. The previous
chapter detailed the analysis of uniform materials using MRI-based displacement
measures and a modeling framework rooted in a two component mixture theory. In this
chapter, the mixture theory-based model will be applied toward the *in situ* analysis of
human intervertebral discs. This model advances the intervertebral disc model developed
in Chapter 4 with the inclusion of a more advanced material model accounting for three
distinct regions within the discs. In addition, this model will demonstrate the
incorporation of diffusion tensor imaging in the evaluation of disc microstructure and
material modeling. A sensitivity analysis of the model will also be performed to evaluate
which factors have the largest impact on the outcome of the models, and how uncertainty
in model inputs may affect a generated solution.

7.2. Methods

7.2.1. Magnetic Resonance Imaging

Displacements in three human cadaveric L4-L5 intervertebral discs were measured using
dualMRI in a 9.4 Tesla scanner Biospec (Bruker Medical GMBH, Ettlington, Germany).
The intact discs and surrounding vertebral bodies were isolated from three fresh-frozen
cadaveric lumbar spines obtained from a tissue and organ donation center (Unyts,
Buffalo, NY). The ends of the disc segments were potted in a fiberglass resin to be

fastened in a MRI-compatible loading device. Prior to loading the discs were wrapped in gauze soaked with PBS to help prevent breakdown of the disc tissue during loading. The discs were then subjected to a cyclic compressive axial load of 445 N (Figure 7.1). A steady state load-displacement response was achieved after 500 cycles, following which imaging began. Imaging parameters were: echo time = 1.6 milliseconds, field of view = 64 mm × 64 mm, slice thickness = 2 mm.
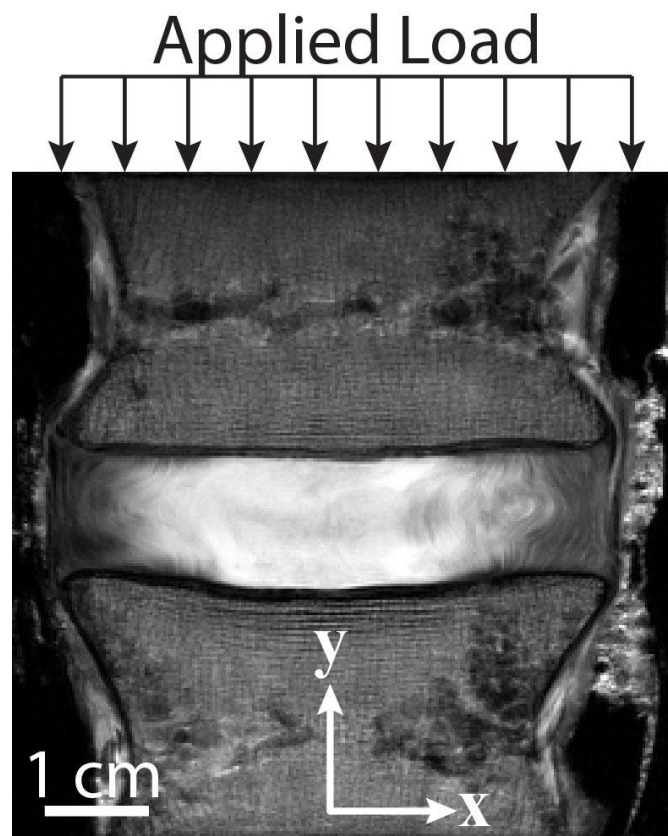
Figure 7.1: Displacements and strains were obtained with dualMRI for human intervertebral discs subjected to a cyclic 445 N load in the axial (z) direction.

In contrast to the previous models, where two-dimensional displacements were known for a single plane, displacements were measured for two central orthogonal imaging planes. In addition, both in- and out-of-plane displacements were measured within the disc. The addition of a second plane and out-of-plane displacement allows for much greater knowledge of deformations within the discs during applied loading. Deformation gradients and strains were computed as described previously.

Diffusion tensor imaging (DTI) data was acquired for each disc, which provided a method for the measurement of diffusion magnitude and direction for each sample. One way in which the directionality of diffusion within a region may be used is to provide greater knowledge of local microstructure. For example, regions where diffusion is highly anisotropic typically indicate the presence of a highly oriented or fibrous microstructure, with fiber orientation aligning with the direction of highest diffusion [96]. In this way, local organization of the disc microstructure could be inferred and used to provide a more detailed material model of the discs.

7.2.2. Computational Analysis of Human Intervertebral Disc

Stress distributions and model parameters were determined in the discs using MRI-based displacement measures, as before. In addition, calculations of mean diffusion, as well as fractional anisotropy and direction were calculated from the DTI data to provide greater insight into local diffusion and disc microstructure. First, mean diffusion was calculated as

$$\frac{tr(\boldsymbol{D})}{3} = D_{11} + D_{22} + D_{33}, \tag{7.1}$$

where $\boldsymbol{D}$ is the diffusion tensor.

Next, the local fractional anisotropy of diffusion throughout the disc was determined by

$$FA = \sqrt{\frac{1}{2} \frac{\sqrt{(\lambda_1 - \lambda_2)^2 + (\lambda_2 - \lambda_3)^2 + (\lambda_3 - \lambda_1)^2}}{\sqrt{\lambda_1^2 + \lambda_2^2 + \lambda_3^2}}}, \tag{7.2}$$

where λ_1, λ_2, and λ_3 are the eigenvalues of the diffusion tensor.

Finally, the direction of highest diffusion was calculated. This was determined at each point within the region of interest by calculating the eigenvector associated with the largest eigenvalue of the diffusion tensor. Combining the knowledge provided by these calculations permits the determination of regional differences by local anisotropy as well as preferred fiber orientations within the disc.

Using this information, the discs were manually segmented into three computational regions: nucleus pulposus, outer annulus fibrosus, and inner annulus fibrosus. The separation of the annulus fibrosus into outer and inner regions allows for the presence of a transition zone where the inner region of the annulus contains more fluid and fiber orientations are less distinct than in the outer zone [27].

The external shape of the disc volume was reconstructed for each sample by manually defining the external boundaries in Photoshop for multiple image slices acquired in both the sagittal and coronal planes throughout the thickness of the disc. An array was then constructed of the intersecting images, and volumetric profiles of the discs were generated by fitting polynomial curves to these defined boundaries in MATLAB (Figure 7.2). T_2 and DTI image intensity was similarly used to manually define internal boundaries of the nucleus and both inner and outer annulus regions. These regions, as well as deformations throughout the reconstructed disc profile were then estimated by linearly interpolating between planes along the defined profile curves. By approximating displacements throughout an estimated volume in this manner, it was hoped that a more physiologically relevant estimation of the stress state could be achieved than would be possible with either the plane stress or axially symmetric assumptions used previously.
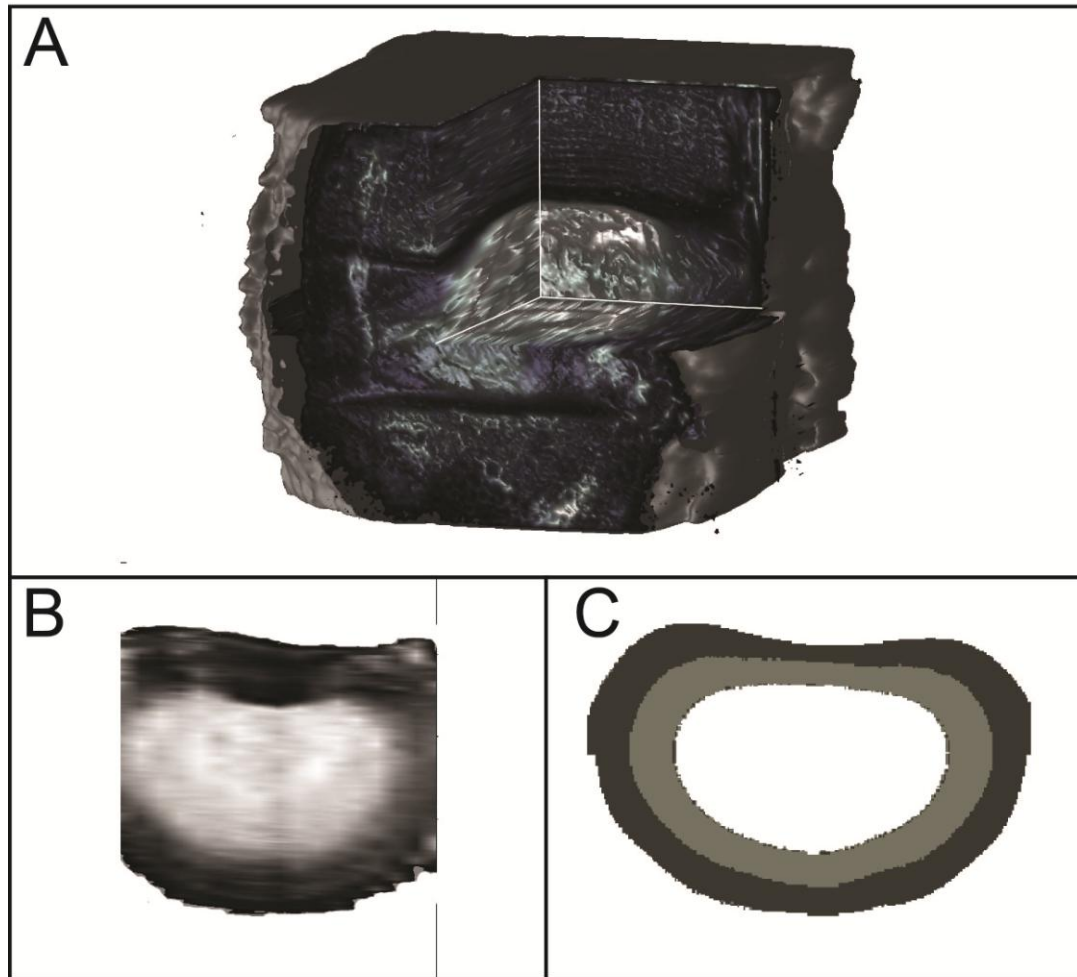
Figure 7.2: A) A partial reconstruction of a disc volume created from RARE cross-sectional images and the isosurface function in MATLAB provides a visualization of the internal geometry of a representative disc. B) A transverse view of the extrapolated image volume demonstrates the curvature of a portion of the disc geometry. C) External and internal boundaries of the discs were manually defined from T_2 and DTI image intensity. Polynomial curves fit to these boundaries defined the outer boundaries as well as the nucleus (white), inner annulus (light gray), and outer annulus (dark gray) regions, as seen in this representative transverse slice of the estimated volume.

Both the nucleus pulposus and the inner annulus fibrosus regions were modeled as isotropic, two-component mixtures with the solid component modeled as a compressible Neo-Hookean solid, as described in (6.12-6.14).

A transversely isotropic, fiber-reinforced Neo-Hookean model was employed in the outer annulus fibrosus region [97]. In this form, the strain energy density function is represented as

$$W = c_1 \left(J^{-2/3} I_1 - 3 \right) + c_2 (J - 1)^2 + \frac{\alpha}{2} (I_4 - 1)^2. \tag{7.3}$$

In this equation, c_1 and c_2 are Neo-Hookean material parameters, α is a material parameter associated with the fiber reinforcing function, J is the determinant of the deformation gradient F, and I_1 is the first invariant given by

$$I_1 = \mathrm{tr} C, \tag{7.4}$$

where C is the right Cauchy-Green tensor. I_4 is the fourth invariant,

$$I_4 = a_o C a_o, \tag{7.5}$$

where a_o is a unit vector in the direction of fiber orientation, determined by the DTI data and the direction of highest diffusion.

The second Piola Kirchoff stress is then given by

$$S = 2 \left[c_1 J^{-2/3} \left(I - \frac{1}{3} (\mathrm{tr} C) C^{-1} \right) + c_2 J (J - 1) C^{-1} + \alpha (a_o C a_o - 1)(a_o \otimes a_o) \right], \tag{7.6}$$

where I is the identity tensor. As before, the first Piola Kirchoff stress, P, is determined by the relation $P=FS$.

A direct measure of local fluid volume fraction was not possible for the discs, and so fluid content was estimated for each region. Here the discs were considered to have unbound water content approximate to that of a fresh disc sample, with fluid volume fractions of 0.8, 0.7, and 0.65 assumed for the nucleus, inner annulus, and outer annulus regions, respectively [98]. A nonlinear least squares fit was then used to fit material parameter values to the equilibrium equations to within a function tolerance of 1e-7.

7.2.3. Sensitivity Analysis

The sensitivity of the model to variations in inputs was investigated using Cotter's Method in the same manner as in the previous chapter. As with the agarose gel model, the primary inputs to the MRI-based IVD model are the applied loading condition, the measured displacements, and the assumed fluid volume fractions of each region. Therefore, the sensitivity analysis focused on possible variations in these parameters.

The influence of potential variation in the applied load was investigated by varying the loading condition to the model by ±5%. Meanwhile, variation in the displacement fields used as inputs is primarily affected by the number of smoothing cycles implemented during processing of the raw MRI data. In the primary model, 50 smoothing cycles was used to process the displacement data. For the purposes of the sensitivity analysis, displacements processed with 10 and 100 smoothing cycles were used for the low and high parameter values, respectively. The fluid volume fractions of the outer annulus, inner annulus, and the nucleus were each varied by ±10% [99]. These factors and the sequence of evaluation are summarized in Table 7.1 and Table 7.2.

Table 7.1: Cotter's Method was used to evaluate the sensitivity of the finite strain-based model outputs to changes in model inputs. The inputs evaluated were the applied loading condition, the number of smoothing cycles used during processing of the displacement data, and the fluid volume fraction of the nucleus (ϕ_N^f), inner annulus (ϕ_{AI}^f), and outer annulus (ϕ_{AO}^f). Sensitivity was evaluated by running the model at alternately low- and high-end values for the inputs identified.

	FSB Model Value	Low Value	High Value
Load (N)	445	422.75	467.25
Smoothing Cycles	50	10	100
ϕ_N^f	0.8	0.7	0.9
ϕ_{AI}^f	0.7	0.6	0.8
ϕ_{AO}^f	0.65	0.55	0.75

Table 7.2: Summary of the model evaluations performed in the Cotter's sensitivity analysis. In this table, "H" indicates that the high-end value of the given input was used in the model and "L" indicates that the low-end value was used. The test was performed for all three disc samples.

Test Number	1	2	3	4	5	6	7	8	9	10	11	12
Load	H	L	H	H	H	H	H	L	L	L	L	L
Smoothing Cycles	H	H	L	H	H	H	L	H	L	L	L	L
ϕ_N^f	H	H	H	L	H	H	L	L	H	L	L	L
ϕ_{AI}^f	H	H	H	H	L	H	L	L	L	H	L	L
ϕ_{AO}^f	H	H	H	H	H	L	L	L	L	L	H	L

7.3. Results

7.3.1. Magnetic Resonance Imaging

Heterogeneous displacements and strains were observed within the three discs. The nucleus regions of the discs were found to exhibit large transverse displacements in response to applied loading (Figure 7.3). In contrast, displacements near the outer edge of the discs did not typically display large displacements orthogonal to the direction of loading, suggesting little radial expansion of the annulus.
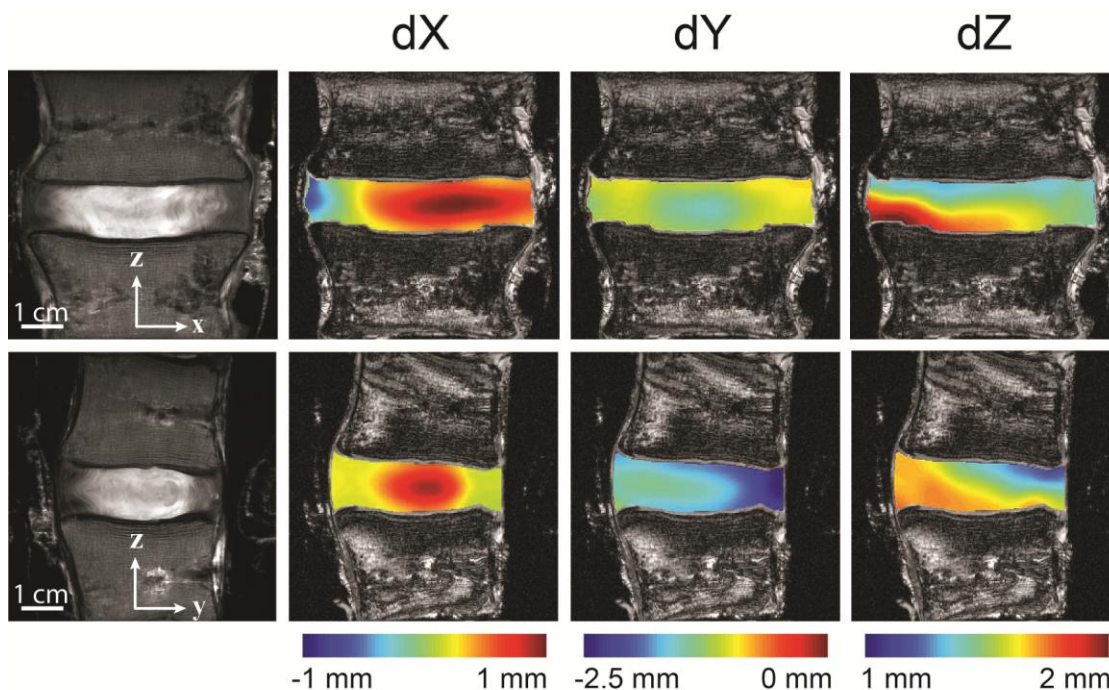
Figure 7.3: Heterogeneous displacement fields were measured in three human intervertebral discs subjected to an axial load of 445 N. High displacements may be seen occurring in the transverse directions at the center of the discs. In contrast, very small transverse displacement is observed in the outer regions of the discs, indicating little radial expansion of the disc as a whole to compression.

Non-symmetric strains and shear behavior evident in the discs indicate that deformation was not purely in the axial direction and that a degree of non-uniform bending took place within the discs during the period of applied load (Figure 7.4).
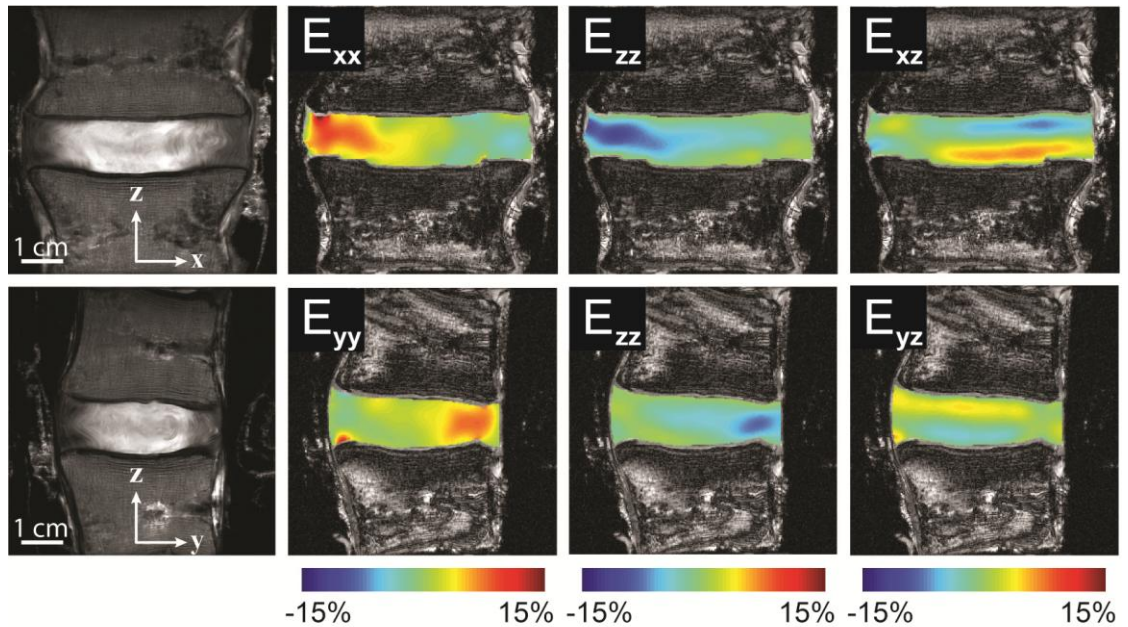
Figure 7.4: Strain fields in the coronal and sagittal planes were determined for each disc. In this representative disc, higher strains to one side of the disc indicate some bending behavior in the disc in response to the axial load. High shear strains in this disc also indicate shearing of the structure occurred during the applied load.

DTI results of the mean diffusion within the discs show mean diffusion values of 1.8e-3 mm^2/s within the central region of the disc, with values decreasing to values of 1.0e-3 mm^2/s near the outer boundaries (Figure 7.5). Calculations of fractional anisotropy within the discs showed large central regions of low anisotropy (Figure 7.6). This is typical of an isotropic nucleus, as well as a transition zone of low structural organization between the nucleus and outer annulus region. In regions of high anisotropy, the direction

of highest diffusion tended to align with the axial and out-of-plane directions (Figure 7.7). This indicates similarly oriented fibril alignment within the outer annulus, which would agree with typical fibril orientations observed in the anatomy.
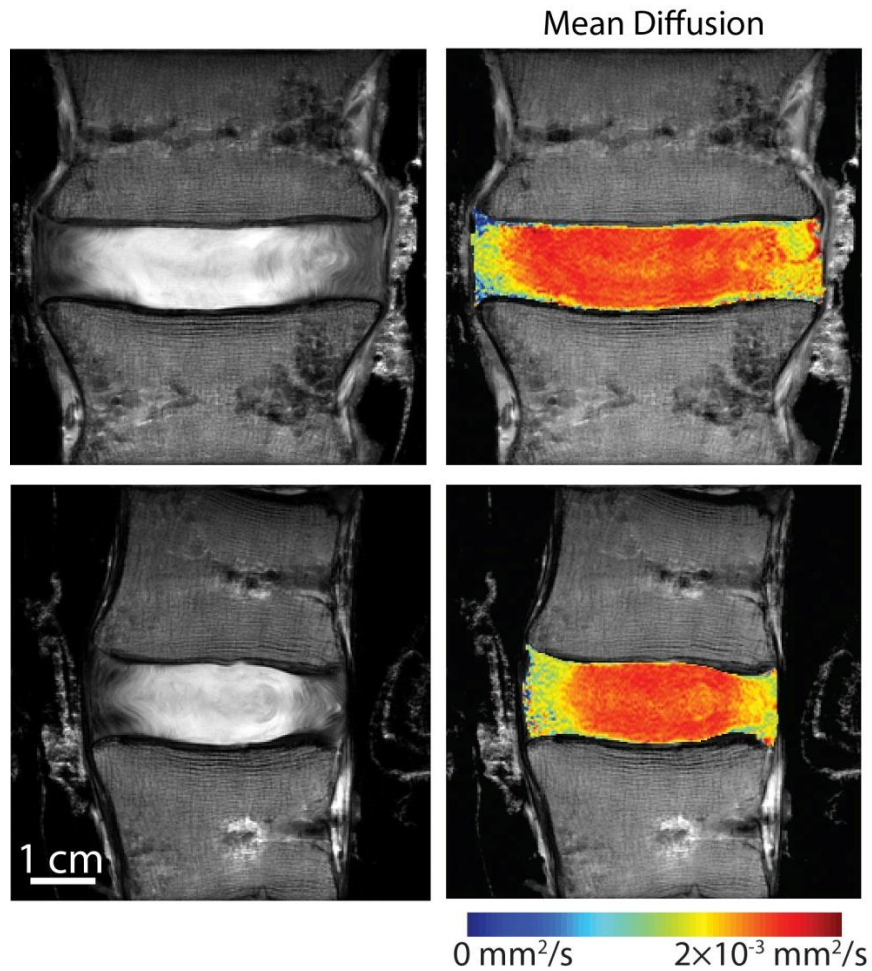
Figure 7.5: Mean diffusion values were calculated for each disc from DTI. These results show the highest diffusion occurring in the center of the disc, with values decreasing with radial distance from the center.
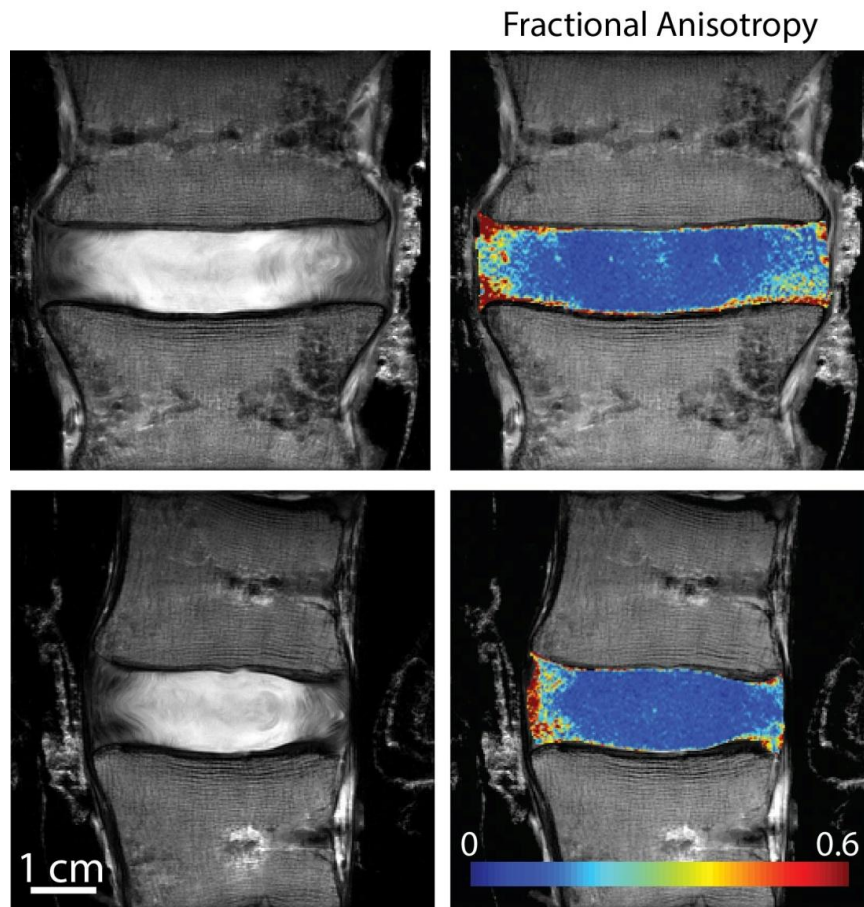
Figure 7.6: The fractional anisotropy of diffusion was calculated for each disc. These calculations show diffusion was highly isotropic in the center of the disc. The fractional anisotropy was highest near the outer edges of the discs, where fibrils in the annulus are highly oriented.
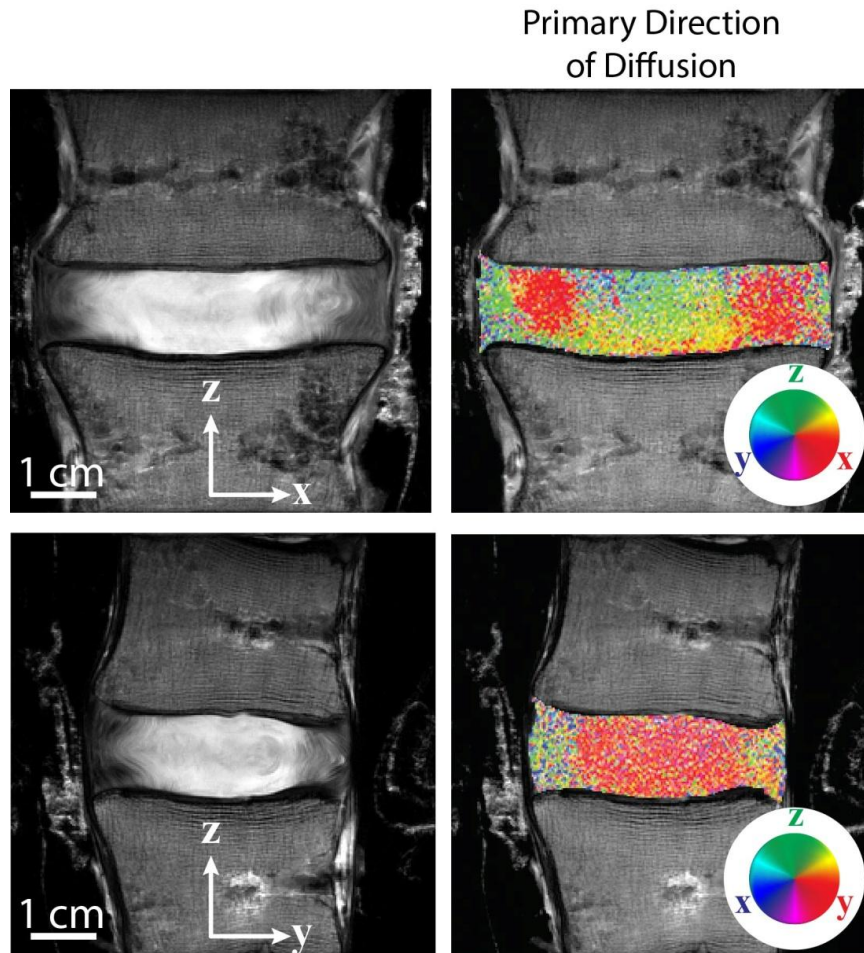
Figure 7.7: The direction of highest diffusion was calculated from the DTI data to provide an indication of collagen fibril alignment in the discs. In the outer region, where fractional anisotropy was highest, diffusion was found to occur primarily in the axial and out of plane directions consistent with typical alignment of collagen fibrils in the annulus of a normal intervertebral disc.

7.3.2. Computational Analysis of Human Intervertebral Disc

Neo-Hookean parameters determined by the finite strain-based model for the three discs are summarized in Table 7.3. Mean values for c_1 were 8.60 MPa, 1.18 MPa, and 1.48 MPa for the nucleus, inner annulus, and outer annulus regions, respectively. Similarly, mean values for c_2 were 3.74 MPa, 4.20 MPa, and 0.72 MPa for the nucleus, inner annulus, and outer annulus, respectively. Large variations in parameter estimates were found to occur between discs for the three sub-regions.

Table 7.3: Mean and STD values of constants of the three discs and mean results.

		Nucleus	Inner Annulus	Outer Annulus
	c_1 (Pa)	7.93e6	4.28e-2	1.27e-4
Disc 1	c_2 (Pa)	9.67e6	1.26e7	1.49e-10
	α (Pa)	-	-	2.22e-14
	c_1 (Pa)	1.29e7	2.47e-14	2.88e-4
Disc 2	c_2 (Pa)	1.01e-6	1.19e-9	2.16e6
	α (Pa)	-	-	0
	c_1 (Pa)	4.97e6	3.54e6	4.43e6
Disc 3	c_2 (Pa)	9.67e6	1.01e-6	1.56e6
	α (Pa)	-	-	1.05e-4
	c_1 (Pa)	8.60e6 ± 3.27e6	1.18e6 ± 1.67e6	1.48e6 ± 2.09e6
Mean ± STD	c_2 (Pa)	3.74e6 ± 4.24e6	4.20e6 ± 5.94e6	7.21e5 ± 1.02e6
	α (Pa)	-	-	3.51e-5 ± 4.96e-5

Principal stresses (Figures 7.8-7.10) and the components σ_{ij} of the stress tensor (Appendix A) were calculated for all discs. Compressive normal stresses in the range of 2-3 MPa were calculated throughout the majority of the nucleus and inner annulus regions, with significantly lower stresses estimated throughout the outer annulus region. Concentrations in stress were found to occur at the center axis of the discs, which also coincides with the intersection line of the imaging planes in which displacements were measured.
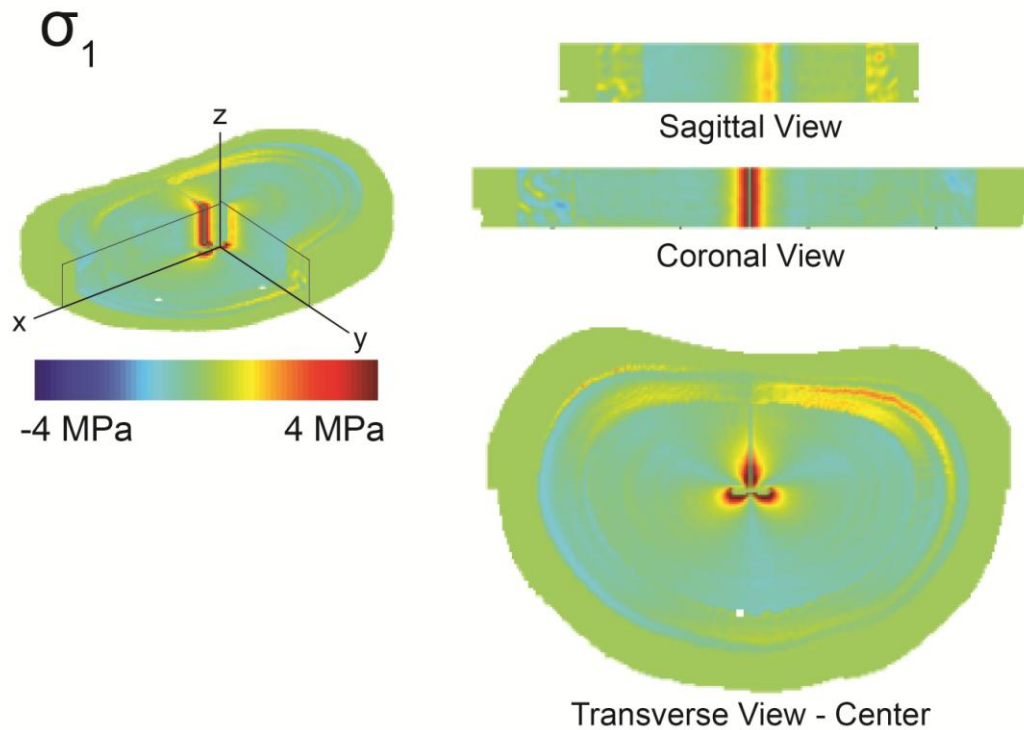
Figure 7.8: Isometric, sagittal (*y-z* plane), coronal plane (*x-z*), and transverse (*x-y*) plane views of principal stress σ_1 for a representative disc.
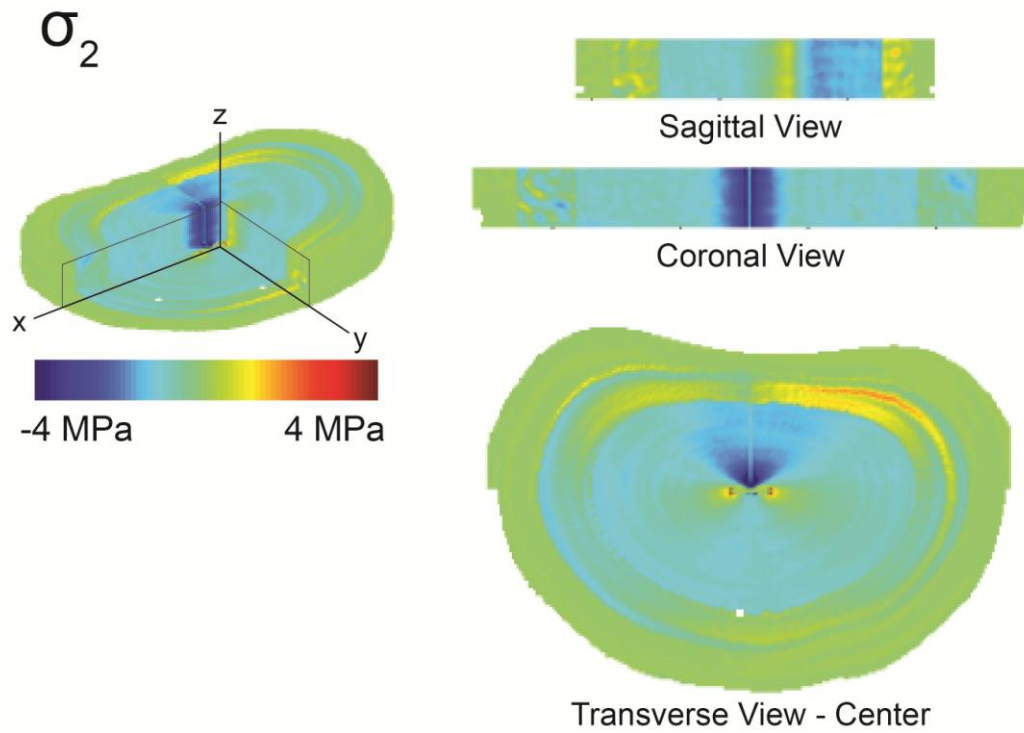
Figure 7.9: Isometric, sagittal (*y-z* plane), coronal plane (*x-z*), and transverse (*x-y*) plane views of principal stress σ_2 for a representative disc.
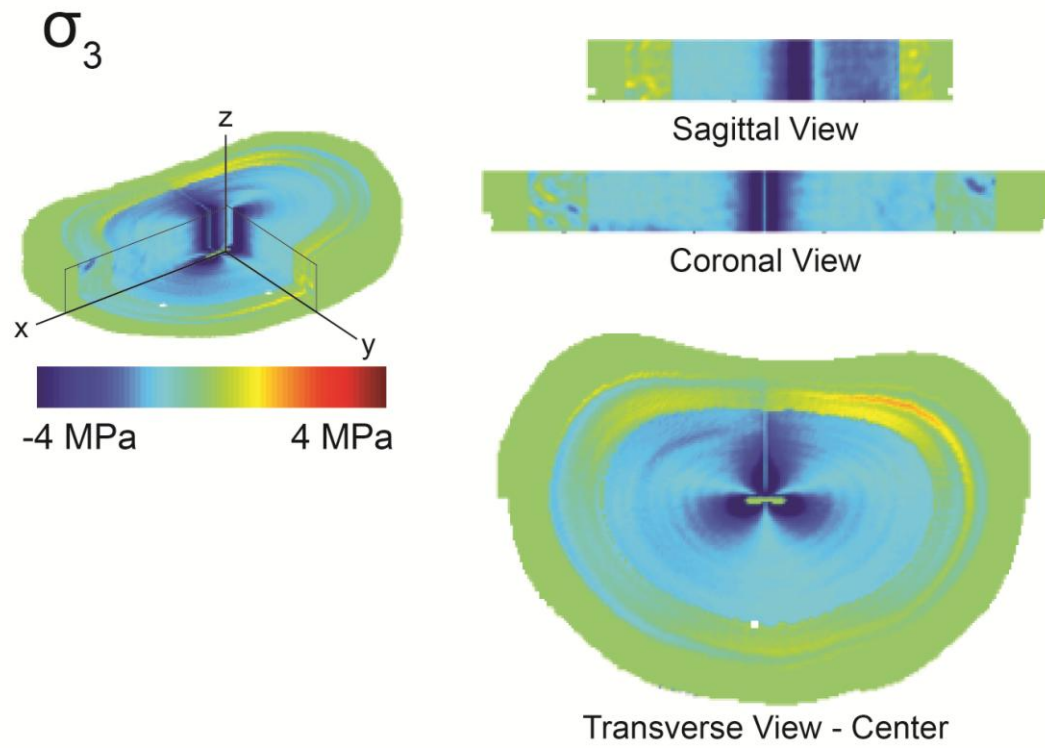
Figure 7.10: Isometric, sagittal (*y-z* plane), coronal plane (*x-z*), and transverse (*x-y*) plane views of principal stress σ_3 for a representative disc.

7.3.3. Sensitivity Analysis

Evaluation of the sensitivity of the model Neo-Hookean material parameters showed that the applied loading condition input to the model was the most consistently sensitive parameter, resulting in the highest sensitivity factor for six of the seven outputs. The exception was parameter c_2 in the outer annulus, which was most sensitive to changes in the nucleus fluid volume fraction (Table 7.4).

Table 7.4: Results of the Cotter's sensitivity analysis for Neo-Hookean parameters c_1 and c_2 at each disc sub-region (mean $\pm$ standard deviation).

	Nucleus		Inner Annulus		Outer Annulus		
	c_1	c_2	c_1	c_2	c_1	c_2	α
S_{Load}	0.84 ± 0.17	0.24 ± 0.13	0.49 ± 0.19	0.39 ± 0.05	0.27 ± 0.11	0.18 ± 0.12	0.63 ± 0.26
$S_{Smoothing}$	0.03 ± 0.05	0.20 ± 0.03	0.07 ± 0.07	0.07 ± 0.07	0.17 ± 0.01	0.17 ± 0.02	0.04 ± 0.06
$S_{\phi_N^f}$	0.07 ± 0.08	0.18 ± 0.03	0.15 ± 0.05	0.20 ± 0.04	0.22 ± 0.00	0.28 ± 0.02	0.10 ± 0.05
$S_{\phi_{AI}^f}$	0.02 ± 0.03	0.19 ± 0.02	0.15 ± 0.06	0.17 ± 0.02	0.14 ± 0.03	0.20 ± 0.03	0.13 ± 0.09
$S_{\phi_{AO}^f}$	0.03 ± 0.03	0.19 ± 0.02	0.15 ± 0.06	0.17 ± 0.03	0.20 ± 0.06	0.17 ± 0.04	0.10 ± 0.08

7.4. Discussion

Compressive stresses throughout the disc structure were highest in the nucleus region for all discs, with lesser compressive stresses observed in the inner annulus and minimal stresses demonstrated in the outer annulus. This result as well as the overall magnitude of stress in the nucleus was consistent with measures by other studies of internal disc pressure during physiologically relevant loading [98, 100-102]. As a result of the low stress state within the outer annulus, the fiber-reinforced model did not play a significant role in the results. This may be largely due to the discs showing little evidence of either radial expansion or axial tension due to bending. In scenarios where the dominate

deformation state of the annulus is compression, the annulus has been found to demonstrate little direction dependency [34]. Controlled torsion or disc bulging loading scenarios would likely result in a greater importance for the inclusion of a fiber-reinforced model.

Parameter estimates were found to vary dramatically between samples. These results may be due in part to the effect of unbalanced loading conditions in the discs. Such conditions may result in a material response that is a combination of axial, shear, and bending loading behavior rather than simply the assumed axial loading condition. As a result, more knowledge of the loading distribution or the analysis of alternate loading scenarios that place a more consistent deformation across the disc may produce more consistent and repeatable model results. Future work towards the optimization of loading conditions for the modeling of IVD mechanics may also be useful towards the development of *in vivo* studies.

Small areas of concentrated stress were observed in the stress fields near the center of each disc. This appears to be due to slight discontinuities in the displacement fields at the intersection point of the two imaging planes. When displacements are interpolated between the two planes, discontinuities near the intersection point may cause spikes in the deformation gradient. It is possible that the process of smoothing the raw displacement data during processing may be the source of these discrepancies.

The sensitivity analysis of the model indicated that load was the most sensitive input parameter to the model outputs. For six of the seven material outputs, the loading condition was the most sensitive input parameter. Surprisingly, the parameter c_2 in the outer annulus region was most sensitive to fluid volume fraction of the nucleus. The inner annulus region parameter c_2 also showed some sensitivity to this parameter. It is possible this may be due in part to the effect fluid content has on the load-bearing qualities of the nucleus region. Physically, this is somewhat analogous to observations during the degeneration process when the nucleus suffers a loss in water content or becomes

otherwise compromised. The loss of fluid content in the nucleus often shifts load distribution outward, causing increased compressive loading on the annulus and, subsequently, further deterioration of the annulus structure [34].

The methods presented in this chapter represent a significant step forward towards the three-dimensional *in vivo* mathematical analysis of intervertebral disc mechanics solely from MRI-based measures of displacement and composition. With further future development, such models may eventually permit diagnostic, image-based stress analysis of tissue in clinical settings, where traditional finite element methods would otherwise not be feasible.

CHAPTER 8. SUMMARY AND FUTURE WORK

The primary objective of this work was to develop a computational framework for the noninvasive analysis of soft tissue stresses and material parameters using MRI-based measures.

The first step towards this goal was the modeling of a two-dimensional stress response of a homogeneous material using only knowledge of in-plane deformations and loading state. This model was applied to the analysis of juvenile porcine cartilage experiencing a cyclic applied load. Material properties of the cartilage were estimated for three constitutive relations. The relations investigated were linear elastic, incompressible Neo-Hookean, and incompressible Mooney-Rivlin material models. The incompressible Neo-Hookean relationship was found to be the most appropriate model for characterizing the nonlinear, large strain behavior of the cartilage when only in-plane deformations and loading condition are known.

The modeling methods were then expanded to perform analyses of multi-region, heterogeneous systems. Stresses and material parameters were estimated for a rabbit intervertebral disc system. Measures of local biochemical composition were used in the development of the material models, allowing for the inclusion of heterogeneous material behavior. Both degenerated and non-degenerated disc states were analyzed in the model. The stress response of the discs were found to agree well with behavior characteristic of both healthy and degenerated states, suggesting future potential for noninvasive analysis of degeneration.

Further expansion of the imaging-based model was focused on allowing for the analysis of porous biomaterials. This model was subsequently created and validated for an agarose

gel system. An axisymmetric model accounting for the presence of an unbound fluid constituent within a porous solid matrix was used in the analysis. The force-displacement response of the gels was measured in unconfined compression as a means of evaluating the accuracy of material parameter estimates. Results for the solid constituent parameters calculated by the finite strain-based model were found to agree well with those fit to the unconfined compression force-displacement curve.

Finally, the multi-constituent mixture model was applied towards the analysis of an *in situ* stress response of human intervertebral discs subjected to axial loading. Magnetic resonance imaging measures of diffusion magnitude and direction were used to identify material sub-regions within the discs and to provide an indication of local microstructure. Stress behavior characteristic of the loading response of typical intervertebral discs was observed. A large variance in material parameter estimates across the sample size suggests that measures of the disc response during more highly controlled deformations may be necessary to better constrain parameter estimates in similarly complex models.

Under the conditions of the current models, where a given system is assumed to be in a quasi-steady state and the influence of time-dependent behavior is assumed negligible, a compressible solid material model may be sufficient for estimating the stress state for certain systems. To maximize the application of a multi-constituent model, it may be desirable to repeat data acquisition for a system after varying periods of extended relaxation under applied loading. This would allow for longer periods of fluid exudation from the system. In turn, this could potentially lead to an enhanced capability of predicting the time-dependent response of the tissue or the influence of permeability and diffusion to the load response. Due to the time requirements, such experiments would lend themselves more readily in the short term to research applications investigating tissue mechanics and load response than to clinical applications.

The next step for this work is the application of the modeling methods described here to *in vivo* systems. Other short-term extensions of these methods may focus on extending

the results of the finite strain-based models to allow for the prediction of behavior under high strain rate loading conditions. Under these conditions, the fluid motion and drag force terms of the porous mixture model will become significant and a time-dependent stress response will have a larger influence. Such applications would open possibilities to a number of potential research directions, including tissue impact modeling.

The work performed herein presents a new and novel methodology for the analysis of soft tissue biomechanics, and is the first to use displacement-encoded MRI as the foundation for noninvasive cartilage and intervertebral disc stress analysis. This work represents a significant step forward in noninvasive techniques for the quantification of material behavior in soft biomaterials. Development and enhancement of the methods presented here may allow for valuable insight into long term tissue degeneration models, or open pathways towards noninvasive diagnostic stress modeling in clinical settings. Ultimately, it is hoped that future advancement of MRI-based stress and material analysis will permit wide-ranging insights into the mechanics of a number of soft biomaterial systems that are otherwise not possible with current modeling and measurement techniques.

LIST OF REFERENCES

LIST OF REFERENCES

[1] Lawrence, R. C., Felson, D. T., Helmick, C. G., Arnold, L. M., Choi, H., Deyo, R. A., Gabriel, S., Hirsch, R., Hochberg, M. C., Hunder, G. G., Jordan, J. M., Katz, J. N., Kremers, H. M., and Wolfe, F., 2008, "Estimates of the prevalence of arthritis and other rheumatic conditions in the United States. Part II," Arthritis & Rheumatism, 58(1), pp. 26-35.

[2] Ea, H., Nguyen, C., Bazin, D., Bianchi, A., Guicheux, J., Reboul, P., Daudon, M., and Liote, F., 2011, "Articular cartilage calcification in osteoarthritis: Insights into crystal-induced stress," Arthritis & Rheumatism, 63(1), pp. 10-18.

[3] Shirazi, R., and Shirazi-Adl, A., 2009, "Computational biomechanics of articular cartilage of human knee joint: Effect of osteochondral defects," Journal of Biomechanics, 42, pp. 2458-2465.

[4] Mow, V. C., Kuei, S. C., Lai, W. M., and Armstrong, C. G., 1980, "Biphasic creep and stress relaxation of articular cartilage in compression: Theory and experiments," J Biomech Eng, 102(1), pp. 73-84.

[5] Elliott, D. M., and Setton, L. A., 2001, "Anisotropic and inhomogeneous tensile behavior of the human anulus fibrosus: experimental measurement and material model predictions," J Biomech Eng, 123(3), pp. 256-263.

[6] Federico, S., and Herzog, W., 2008, "Towards an analytical model of soft biological tissues," J Biomech, 41(16), pp. 3309-3313.

[7] Adams, M. A., and Roughley, P. J., 2006, "What is intervertebral disc degeneration, and what causes it?," Spine (Phila Pa 1976), 31(18), pp. 2151-2161.

[8] An, H. S., Masuda, K., and Inoue, N., 2006, "Intervertebral disc degeneration: biological and biomechanical factors," J Orthop Sci, 11(5), pp. 541-552.

[9] Butz, K. D., Chan, D. D., Nauman, E. A., and Neu, C. P., 2011, "Stress distributions and material properties determined in articular cartilage from MRI-based finite strains," J Biomech, 44(15), pp. 2667-2672.

[10]   Mow, V. C., Ratcliffe, A., and Poole, A. R., 1992, "Cartilage and diarthrodial joints as paradigms for hierarchical materials and structures," Biomaterials, 13(2), pp. 67-97.

[11]   Weiss, E., and Jurmain, R., 2007, "Osteoarthritis Revisited: A Contemporary Review of Aetiology," International Journal of Osteoarchaeology, 17, p. 13.

[12]   Huang, C. Y., Stankiewicz, A., Ateshian, G. A., and Mow, V. C., 2005, "Anisotropy, inhomogeneity, and tension-compression nonlinearity of human glenohumeral cartilage in finite deformation," J Biomech, 38(4), pp. 799-809.

[13]   Jurvelin, J. S., Buschmann, M. D., and Hunziker, E. B., 2003, "Mechanical anisotropy of the human knee articular cartilage in compression," Proc Inst Mech Eng H, 217(3), pp. 215-219.

[14]   Kuo, J., Zhang, L., Bacro, T., and Yao, H., 2010, "The region-dependent biphasic viscoelastic properties of human temporomandibular joint discs under confined compression," J Biomech, 43(7), pp. 1316-1321.

[15]   Samosky, J. T., Burstein, D., Eric Grimson, W., Howe, R., Martin, S., and Gray, M. L., 2005, "Spatially-localized correlation of dGEMRIC-measured GAG distribution and mechanical stiffness in the human tibial plateau," J Orthop Res, 23(1), pp. 93-101.

[16]   Quinn, T. M., Dierickx, P., and Grodzinsky, A. J., 2001, "Glycosaminoglycan network geometry may contribute to anisotropic hydraulic permeability in cartilage under compression," J Biomech, 34(11), pp. 1483-1490.

[17]   Weiss, J. A., and Maakestad, B. J., 2006, "Permeability of human medial collateral ligament in compression transverse to the collagen fiber direction," J Biomech, 39(2), pp. 276-283.

[18]   Nguyen, A. M., and Levenston, M. E., 2012, "Comparison of osmotic swelling influences on meniscal fibrocartilage and articular cartilage tissue mechanics in compression and shear," J Orthop Res, 30(1), pp. 95-102.

[19]   Tang, S. Y., Souza, R. B., Ries, M., Hansma, P. K., Alliston, T., and Li, X., 2011, "Local tissue properties of human osteoarthritic cartilage correlate with magnetic resonance T(1) rho relaxation times," J Orthop Res, 29(9), pp. 1312-1319.

[20]   Ralphs, J. R., and Benjamin, M., 1994, "The joint capsule: structure, composition, ageing and disease," J Anat, 184 (Pt 3), pp. 503-509.

[21]   Tanaka, E., Saito, A., Kamitsuji, S., Yamada, T., Nakajima, A., Taniguchi, A., Hara, M., Tomatsu, T., Yamanaka, H., and Kamatani, N., 2005, "Impact of shoulder, elbow, and knee joint involvement on assessment of rheumatoid arthritis using the American College of Rheumatology Core Data Set," Arthritis Rheum, 53(6), pp. 864-871.

[22]   Helliwell, P. S., Hetthen, J., Sokoll, K., Green, M., Marchesoni, A., Lubrano, E., Veale, D., and Emery, P., 2000, "Joint symmetry in early and late rheumatoid and psoriatic arthritis: comparison with a mathematical model," Arthritis Rheum, 43(4), pp. 865-871.

[23]   Chapple, C. M., Nicholson, H., Baxter, G. D., and Abbott, J. H., 2011, "Patient characteristics that predict progression of knee osteoarthritis: a systematic review of prognostic studies," Arthritis Care Res (Hoboken), 63(8), pp. 1115-1125.

[24]   Tanamas, S., Hanna, F. S., Cicuttini, F. M., Wluka, A. E., Berry, P., and Urquhart, D. M., 2009, "Does knee malalignment increase the risk of development and progression of knee osteoarthritis? A systematic review," Arthritis Rheum, 61(4), pp. 459-467.

[25]   Escalante, A., Haas, R. W., and del Rincon, I., 2005, "A model of impairment and functional limitation in rheumatoid arthritis," BMC Musculoskelet Disord, 6, p. 16.

[26]   Mirza, S. K., and White, A. A., 3rd, 1995, "Anatomy of intervertebral disc and pathophysiology of herniated disc disease," J Clin Laser Med Surg, 13(3), pp. 131-142.

[27]   Urban, J. P., and Winlove, C. P., 2007, "Pathophysiology of the intervertebral disc and the challenges for MRI," J Magn Reson Imaging, 25(2), pp. 419-432.

[28]   Perie, D., Korda, D., and Iatridis, J. C., 2005, "Confined compression experiments on bovine nucleus pulposus and annulus fibrosus: sensitivity of the experiment in the determination of compressive modulus and hydraulic permeability," J Biomech, 38(11), pp. 2164-2171.

[29]   Lotz, J. C., Hadi, T., Bratton, C., Reiser, K. M., and Hsieh, A. H., 2008, "Anulus fibrosus tension inhibits degenerative structural changes in lamellar collagen," Eur Spine J, 17(9), pp. 1149-1159.

[30]   Zhao, C. Q., Wang, L. M., Jiang, L. S., and Dai, L. Y., 2007, "The cell biology of intervertebral disc aging and degeneration," Ageing Res Rev, 6(3), pp. 247-261.

[31]   Hristova, G. I., Jarzem, P., Ouellet, J. A., Roughley, P. J., Epure, L. M., Antoniou, J., and Mwale, F., 2011, "Calcification in human intervertebral disc degeneration and scoliosis," J Orthop Res, 29(12), pp. 1888-1895.

[32]   Chan, D. D., Khan, S. N., Ye, X., Curtiss, S. B., Gupta, M. C., Klineberg, E. O., and Neu, C. P., 2011, "Mechanical deformation and glycosaminoglycan content changes in a rabbit annular puncture disc degeneration model," Spine (Phila Pa 1976), 36(18), pp. 1438-1445.

[33]   O'Connell, G. D., Vresilovic, E. J., and Elliott, D. M., 2011, "Human intervertebral disc internal strain in compression: the effect of disc region, loading position, and degeneration," J Orthop Res, 29(4), pp. 547-555.

[34]   Iatridis, J. C., Setton, L. A., Foster, R. J., Rawlins, B. A., Weidenbaum, M., and Mow, V. C., 1998, "Degeneration affects the anisotropic and nonlinear behaviors of human anulus fibrosus in compression," J Biomech, 31(6), pp. 535-544.

[35]   Anderson, A. E., Ellis, B. J., Maas, S. A., and Weiss, J. A., 2010, "Effects of idealized joint geometry on finite element predictions of cartilage contact stresses in the hip," J Biomech, 43(7), pp. 1351-1357.

[36]   Massey, C. J., van Donkelaar, C. C., Vresilovic, E., Zavaliangos, A., and Marcolongo, M., 2012, "Effects of aging and degeneration on the human intervertebral disc during the diurnal cycle: a finite element study," J Orthop Res, 30(1), pp. 122-128.

[37]   Pillai, R. P., Thoomukuntla, B., Ateshian, G. A., and Fischer, K. J., 2007, "MRI-based modeling for evaluation of in vivo contact mechanics in the human wrist during active light grasp," Journal of Biomechanics, 40, pp. 2781-2787.

[38]   Fitzpatrick, C. K., Baldwin, M. A., and Rullkoetter, P. J., 2010, "Computationally efficient finite element evaluation of natural patellofemoral mechanics," Journal of Biomechanical Engineering, 132(December), p. 8.

[39]   Gislason, M. K., Stansfield, B., and Nash, D. H., 2010, "Finite element model creation and stability considerations of complex biological articulation: The human wrist joint," Medical Engineering & Physics, 32, pp. 523-531.

[40]   Anderson, A. E., Peters, C. L., Tuttle, B. D., and Weiss, J. A., 2005, "Subject-specific finite element model of the pelvis: development, validation and sensitivity studies," J Biomech Eng, 127(3), pp. 364-373.

[41]   Koo, S., Giori, N. J., Gold, G. E., Dyrby, C. O., and Andriacchi, T. P., 2009, "Accuracy of 3D cartilage models generated from MR images is dependent on cartilage thickness: laser scanner based validation of in vivo cartilage," J Biomech Eng, 131(12), p. 121004.

[42]   DeFrate, L. E., Sun, H., Gill, T. J., Rubash, H. E., and Li, G., 2004, "In vivo tibiofemoral contact analysis using 3D MRI-based knee models," J Biomech, 37(10), pp. 1499-1504.

[43]   Borotikar, B. S., Sipprell, W. H., 3rd, Wible, E. E., and Sheehan, F. T., 2012, "A methodology to accurately quantify patellofemoral cartilage contact kinematics by combining 3D image shape registration and cine-PC MRI velocity data," J Biomech.

[44]   Gold, G. E., Besier, T. F., Draper, C. E., Asakawa, D. S., Delp, S. L., and Beaupre, G. S., 2004, "Weight-bearing MRI of patellofemoral joint cartilage contact area," J Magn Reson Imaging, 20(3), pp. 526-530.

[45]   Pillai, R. R., Thoomukuntla, B., Ateshian, G. A., and Fischer, K. J., 2007, "MRI-based modeling for evaluation of in vivo contact mechanics in the human wrist during active light grasp," J Biomech, 40(12), pp. 2781-2787.

[46]   Yang, N. H., Nayeb-Hashemi, H., Canavan, P. K., and Vaziri, A., 2010, "Effect of frontal plane tibiofemoral angle on the stress and strain at the knee cartilage during the stance phase of gait," J Orthop Res, 28(12), pp. 1539-1547.

[47]   Vaverka, M., Navrat, T. S., Vrbka, M., Florian, Z., and Fuis, V., 2006, "Stress and strain analysis of the hip joint using FEM," Technol Health Care, 14(4-5), pp. 271-279.

[48]   Chen, Y., and Ostoja-Starzewski, M., 2010, "MRI-based finite element modeling of head trauma: spherically focusing shear waves " Acta Mechanica, 213, pp. 155-167.

[49]   Post, A., Hoshizaki, B., and Gilchrist, M. D., 2012, "Finite element analysis of the effect of loading curve shape on brain injury predictors," J Biomech, 45(4), pp. 679-683.

[50]   Pierce, D. M., Trobin, W., and Holzapfel, G. A., 2009, "A Computational Framework for Patient-Specific Analysis of Articular Cartilage Incorporating Structural Information from DT-MRI " GAMM-Mitt, 2, p. 20.

[51]   Pierce, D. M., Trobin, W., Trattnig, S., Bischof, H., and Holzapfel, G. A., 2009, "A phenomenological approach toward patient-specific computational modeling of articular cartilage including collagen fiber tracking," J Biomech Eng, 131(9), p. 091006.

[52]   Pierce, D. M., Trobin, W., Raya, J. G., Trattnig, S., Bischof, H., Glaser, C., and Holzapfel, G. A., 2010, "DT-MRI based computation of collagen fiber deformation in human articular cartilage: a feasibility study," Ann Biomed Eng, 38(7), pp. 2447-2463.

[53]   Federico, S., and Herzog, W., 2008, "Towards an analytical model of soft biological tissues," Journal of Biomechanics, 41, pp. 3309-3313.

[54]   Galle, B., Ouyang, H., Shi, R., and Nauman, E., 2007, "Correlations between tissue-level stresses and strains and cellular damage within the guinea pig spinal cord white matter," J Biomech, 40(13), pp. 3029-3033.

[55]   Julkunen, P., Wilson, W., Jurvelin, J. S., Rieppo, J., Qu, C., Lammi, M. J., and Korhonen, R. K., 2008, "Stress-relaxation of human patellar articular cartilage in unconfined compression: Prediction of mechanical response by tissue composition and structure," Journal of BIomechanics, 41, pp. 1978-1986.

[56]   Laksari, K., Shafieian, M., and Darvish, K., 2012, "Constitutive model for brain tissue under finite compression," J Biomech, 45(4), pp. 642-646.

[57]   Wong, B. L., Bae, W. C., Chun, J., Gratz, K. R., Lotz, M., and Sah, R. L., 2008, "Biomechanics of cartilage articulation: Effects of lubrication and degeneration on shear deformation," Arthritis & Rheumatism, 58(7), pp. 2065-2074.

[58]   Chin, H. C., Khayat, G., and Quinn, T. M., 2011, "Improved characterization of cartilage mechanical properties using a combination of stress relaxation and creep," Journal of Biomechanics, 44, pp. 198-201.

[59]   Anderson, A. E., Ellis, B. J., Maas, S. A., and Weiss, J. A., 2010, "Effects of idealized joint geometry on finite element predictions of cartilage contact stresses in the hip," Journal of Biomechanics, 43, pp. 1351-1357.

[60]   Mow, V. C., Kuei, S. C., Lai, W. M., and Armstrong, C. G., 1980, "Biphasic creep and stress relaxation of articular cartilage in compression? Theory and experiments," J Biomech Eng, 102(1), pp. 73-84.

[61]   Nagel, T., and Kelly, D. J., 2010, "The influence of fiber orientation on the equilibrium properties of neutral and charged biphasic tissues," J Biomech Eng, 132(11), p. 114506.

[62]   Lu, X. L., Miller, C., Chen, F. H., Guo, X. E., and Mow, V. C., 2007, "The generalized triphasic correspondence principle for simultaneous determination of the mechanical properties and proteoglycan content of articular cartilage by indentation," J Biomech, 40(11), pp. 2434-2441.

[63]   Niu, H., Wang, Q., Zheng, Y., and Fan, Y., 2010, "A new method for computing the uniaxial modulus of articular cartilages using modified inhomogeneous triphasic model," (1), pp. 121-126.

[64]   Lu, X. L., Wan, L. Q., Guo, X. E., and Mow, V. C., 2010, "A linearized formulation of triphasic mixture theory for articular cartilage, and its application to indentation analysis," J Biomech, 43(4), pp. 673-679.

[65]   Sun, D. D., Guo, X. E., Likhitpanichkul, M., Lai, W. M., and Mow, V. C., 2004, "The influence of the fixed negative charges on mechanical and electrical behaviors of articular cartilage under unconfined compression," J Biomech Eng, 126(1), pp. 6-16.

[66]   Bercoff, J., Tanter, M., and Fink, M., 2004, "Supersonic shear imaging: a new technique for soft tissue elasticity mapping," IEEE Trans Ultrason Ferroelectr Freq Control, 51(4), pp. 396-409.

[67]   Kwon, O. I., Park, C., Nam, H. S., Woo, E. J., Seo, J. K., Glaser, K. J., Manduca, A., and Ehman, R. L., 2009, "Shear modulus decomposition algorithm in magnetic resonance elastography," IEEE Trans Med Imaging, 28(10), pp. 1526-1533.

[68]   Kiviranta, P., Lammentausta, E., Toyras, J., Nieminen, H. J., Julkunen, P., Kiviranta, I., and Jurvelin, J. S., 2009, "Differences in acoustic properties of intact and degenerated human patellar cartilage during compression," Ultrasound Med Biol, 35(8), pp. 1367-1375.

[69]   Neu, C. P., Hull, M. L., and Walton, J. H., 2005, "Error optimization of a three-dimensional magnetic resonance imaging tagging-based cartilage deformation technique," Magn Reson Med, 54(5), pp. 1290-1294.

[70]   Shehata, M. L., Cheng, S., Osman, N. F., Bluemke, D. A., and Lima, J. A., 2009, "Myocardial tissue tagging with cardiovascular magnetic resonance," J Cardiovasc Magn Reson, 11, p. 55.

[71]   Veress, A. I., Weiss, J. A., Huesman, R. H., Reutter, B. W., Taylor, S. E., Sitek, A., Feng, B., Yang, Y., and Gullberg, G. T., 2008, "Measuring regional changes in the diastolic deformation of the left ventricle of SHR rats using microPET technology and hyperelastic warping," Ann Biomed Eng, 36(7), pp. 1104-1117.

[72]   Phatak, N. S., Maas, S. A., Veress, A. I., Pack, N. A., Di Bella, E. V., and Weiss, J. A., 2009, "Strain measurement in the left ventricle during systole with deformable image registration," Med Image Anal, 13(2), pp. 354-361.

[73]   Phatak, N. S., Sun, Q., Kim, S. E., Parker, D. L., Sanders, R. K., Veress, A. I., Ellis, B. J., and Weiss, J. A., 2007, "Noninvasive determination of ligament strain with deformable image registration," Ann Biomed Eng, 35(7), pp. 1175-1187.

[74]   Veress, A. I., Gullberg, G. T., and Weiss, J. A., 2005, "Measurement of strain in the left ventricle during diastole with cine-MRI and deformable image registration," J Biomech Eng, 127(7), pp. 1195-1207.

[75]   Feng, L., Donnino, R., Babb, J., Axel, L., and Kim, D., 2009, "Numerical and in vivo validation of fast cine displacement-encoded with stimulated echoes (DENSE) MRI for quantification of regional cardiac function," Magn Reson Med, 62(3), pp. 682-690.

[76]   Soellinger, M., Rutz, A. K., Kozerke, S., and Boesiger, P., 2009, "3D cine displacement-encoded MRI of pulsatile brain motion," Magn Reson Med, 61(1), pp. 153-162.

[77]   Chan, D. D., Neu, C. P., and Hull, M. L., 2009, "In situ deformation of cartilage in cyclically loaded tibeofemoral joints by displacement-encoded MRI," Osteoarthritis and Cartilage, 17(11), pp. 1461-1468.

[78]   Chan, D. D., Neu, C. P., and Hull, M. L., 2009, "Articular cartilage deformation determined in an intact tibiofemoral joint by displacement-encoded imaging," Magn Reson Med, 61(4), pp. 989-993.

[79]   Neu, C. P., and Walton, J. H., 2008, "Displacement encoding for the measurement of cartilage deformation," Magn Reson Med, 59(1), pp. 149-155.

[80]   Neu, C. P., and Hull, M. L., 2003, "Toward an MRI-based method to measure non-uniform cartilage deformation: an MRI-cyclic loading apparatus system and steady-state cyclic displacement of articular cartilage under compressive loading," Journal of Biomechanical Engineering, 125(2), pp. 180-188.

[81]   Neu, C. P., and Walton, J. H., 2008, "Displacement encoding for the measurement of cartilage deformation," Magnetic Resonance in Medicine, 59(1), pp. 149-155.

[82]   Jin, H., and Lewis, J. L., 2004, "Determination of Poisson's ratio of articular cartilage by indentation using different-sized indenters," J Biomech Eng, 126(2), pp. 138-145.

[83]   Nissi, M. J., Rieppo, J., Toyras, J., Laasanen, M. S., Kiviranta, I., Nieminen, M. T., and Jurvelin, J. S., 2007, "Estimation of mechanical properties of articular cartilage with MRI-dGEMRIC, T_2 and T_1 imaging in different species with variable stages of maturation," Osteoarthritis and Cartilage, 15(10), pp. 1141-1148.

[84]   Nagel, T., and Kelly, D. J., 2010, "The influence of fiber orientation on the equilibrium properties of neutral and charged biphasic tissues," Journal of Biomechanical Engineering, 132(November), p. 7.

[85]   Owen, J. R., and Wayne, J. S., 2010, "Contact models of repaired articular surfaces: Influence of loading conditions and the superficial tangential zone," Biomechanics and Modeling in Mechanobiology, August(August), p. 11.

[86]   Gorke, U., Gunther, H., Nagel, T., and Wimmer, M. A., 2010, "A large strain material model for soft tissues with functionally graded properties," Journal of Biomechanical Engineering, 132(July), p. 6.

[87]   Guess, T. M., Thiagarajan, G., Kia, M., and Mishra, M., 2010, "A subject specific multibody model of the knee with menisci," Medical Engineering & Physics, pp. 505-515.

[88]   Vaziri, A., Nayeb-Hashemi, H., Singh, A., and Tafti, B. A., 2008, "Influence of meniscectomy and meniscus replacement on the stress distribution in human knee joint," Annals of Biomedical Engineering, 36(8), pp. 1335-1344.

[89]   Nissi, M. J., Rieppo, J., Toyras, J., Laasanen, M. S., Kiviranta, I., Nieminen, M. T., and Jurvelin, J. S., 2007, "Estimation of mechanical properties of articular cartilage with MRI - dGEMRIC, T2 and T1 imaging in different species with variable stages of maturation," Osteoarthritis Cartilage, 15(10), pp. 1141-1148.

[90]   Nieminen, M. T., Toyras, J., Laasanen, M. S., Silvennoinen, J., Helminen, H. J., and Jurvelin, J. S., 2004, "Prediction of biomechanical properties of articular cartilage with quantitative magnetic resonance imaging," J Biomech, 37(3), pp. 321-328.

[91]   Johannessen, W., and Elliott, D. M., 2005, "Effects of degeneration on the biphasic material properties of human nucleus pulposus in confined compression," Spine (Phila Pa 1976)United States, pp. E724-729.

[92]   Chen, Q., Suki, B., and An, K. N., 2004, "Dynamic mechanical properties of agarose gels modeled by a fractional derivative model," J Biomech Eng, 126(5), pp. 666-671.

[93]   Saris, D. B., Mukherjee, N., Berglund, L. J., Schultz, F. M., An, K. N., and O'Driscoll, S. W., 2000, "Dynamic pressure transmission through agarose gels," Tissue Eng, 6(5), pp. 531-537.

[94]   Vardar, E., Vert, M., Coudane, J., Hasirci, V., and Hasirci, N., 2011, "Porous Agarose-Based Semi-IPN Hydrogels: Characterization and Cell Affinity Studies," J Biomater Sci Polym Ed.

[95]   Cloyd, J. M., Malhotra, N. R., Weng, L., Chen, W., Mauck, R. L., and Elliott, D. M., 2007, "Material properties in unconfined compression of human nucleus pulposus, injectable hyaluronic acid-based hydrogels and tissue engineering scaffolds," Eur Spine J, 16(11), pp. 1892-1898.

[96]   Le Bihan, D., Mangin, J. F., Poupon, C., Clark, C. A., Pappata, S., Molko, N., and Chabriat, H., 2001, "Diffusion tensor imaging: concepts and applications," J Magn Reson Imaging, 13(4), pp. 534-546.

[97]   Ogden, J. M. a. R. W., 2003, "Instabilities and loss of ellipticity in fiber-reinforced compressible non-linearly elastic solids under plane deformation," International Journal of Solids and Structures, 40, pp. 4707--4727.

[98]   Karajan, N., 2012, "Multiphasic Intervertebral Disc Mechanics: Theory and Application," Archives of Computational Methods in Engineering, 19, pp. 261-339.

[99]   McMillan, D. W., Garbutt, G., and Adams, M. A., 1996, "Effect of sustained loading on the water content of intervertebral discs: implications for disc metabolism," Ann Rheum Dis, 55(12), pp. 880-887.

[100]   Karajan, N., "Multiphasic Intervertebral Disc Mechanics: Theory and Application."

[101]   Adams, M. A., McNally, D. S., and Dolan, P., 1996, "'Stress' distributions inside intervertebral discs. The effects of age and degeneration," The Journal of Bone and Joint Surgery, 78(6), pp. 965-972.

[102]   McNally, D. S., and Adams, M. A., 1992, "Internal intervertebral disc mechanics as revealed by stress profilometry," Spine (Phila Pa 1976), 17(1), pp. 66-73.

APPENDIX

APPENDIX

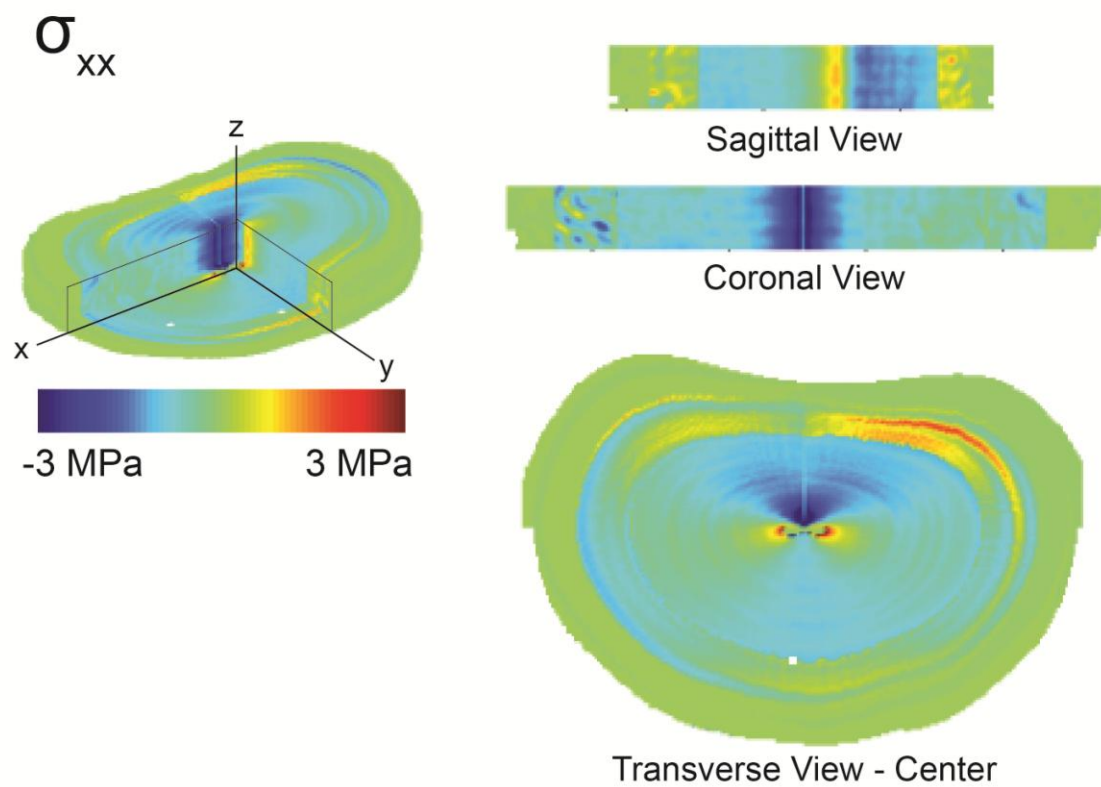Stress Results for a Human Intervertebral Disc during Applied Axial Loading

Figure A.1: Isometric, sagittal (*y-z* plane), coronal plane (*x-z*), and transverse (*x-y*) plane views of σ_{xx} for a representative disc.
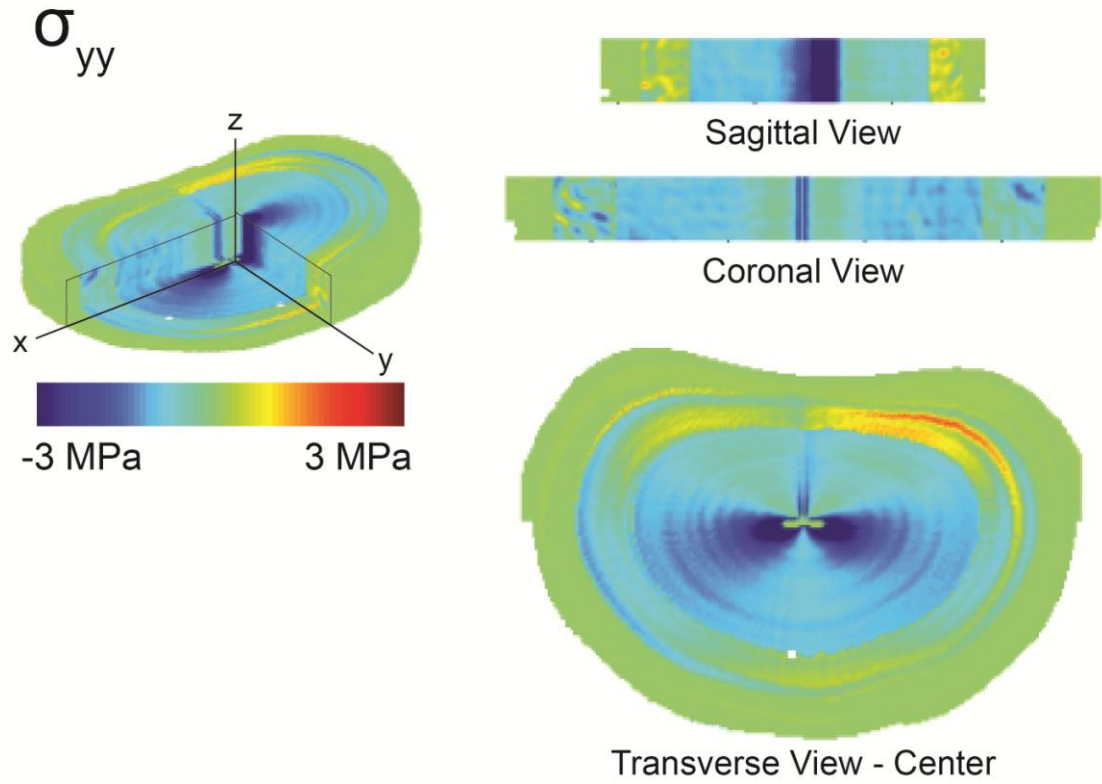
Figure A.2: Isometric, sagittal (*y-z* plane), coronal plane (*x-z*), and transverse (*x-y*) plane views of σ_{yy} for a representative disc.
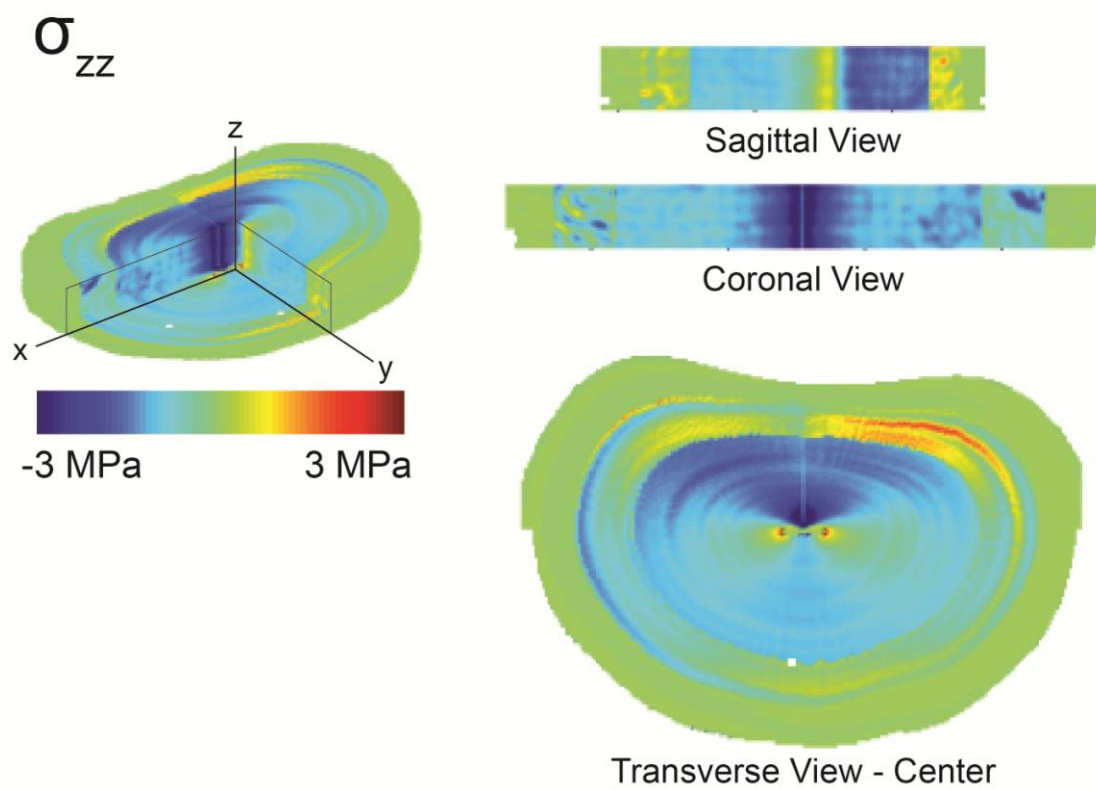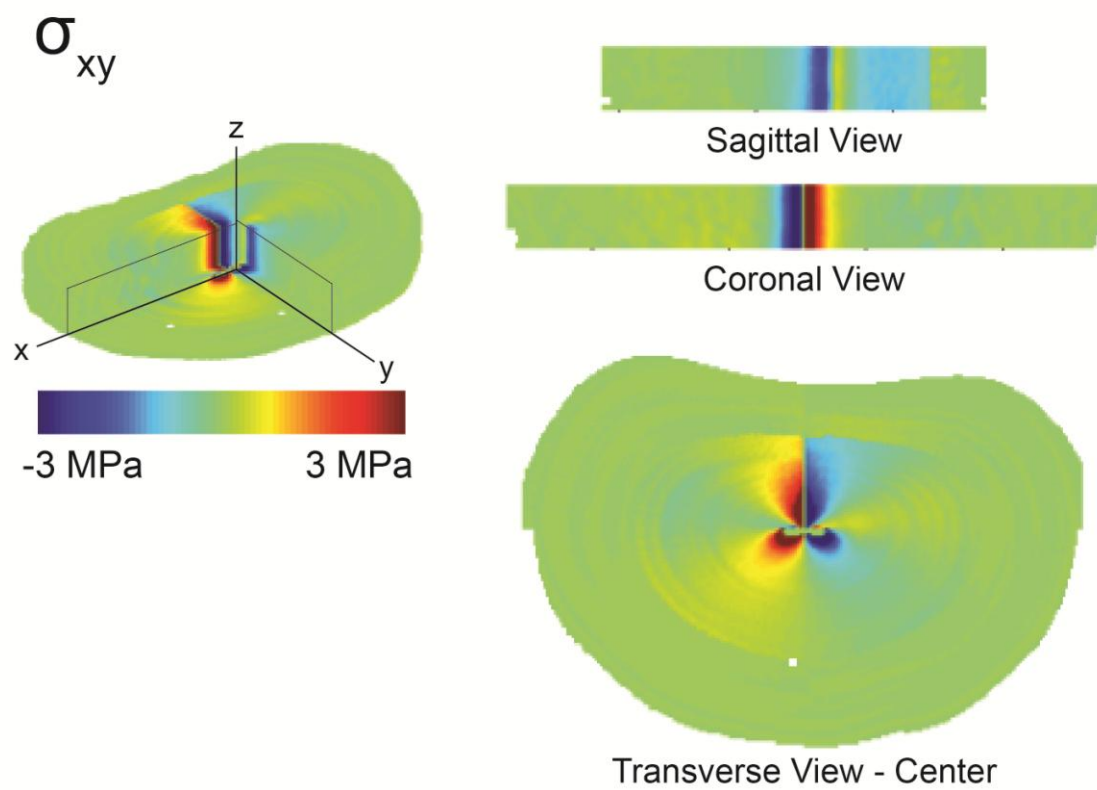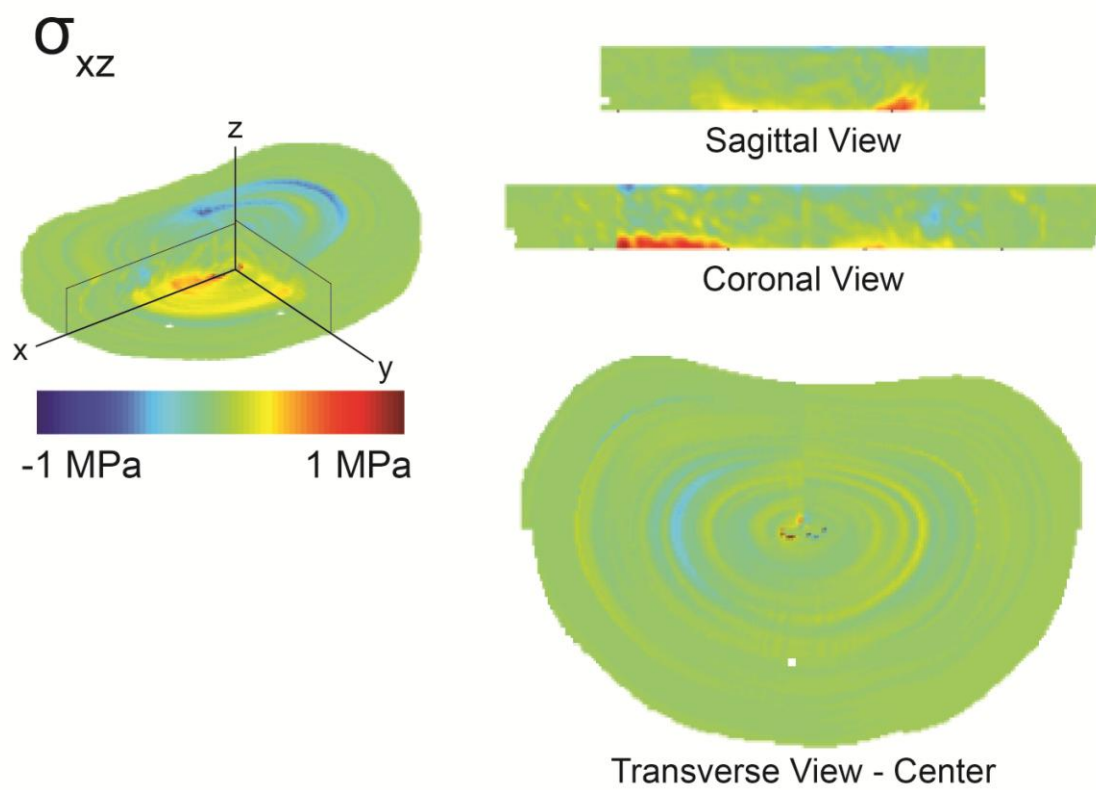
Figure A.3: Isometric, sagittal (*y-z* plane), coronal plane (*x-z*), and transverse (*x-y*) plane views of σ_{zz} for a representative disc.
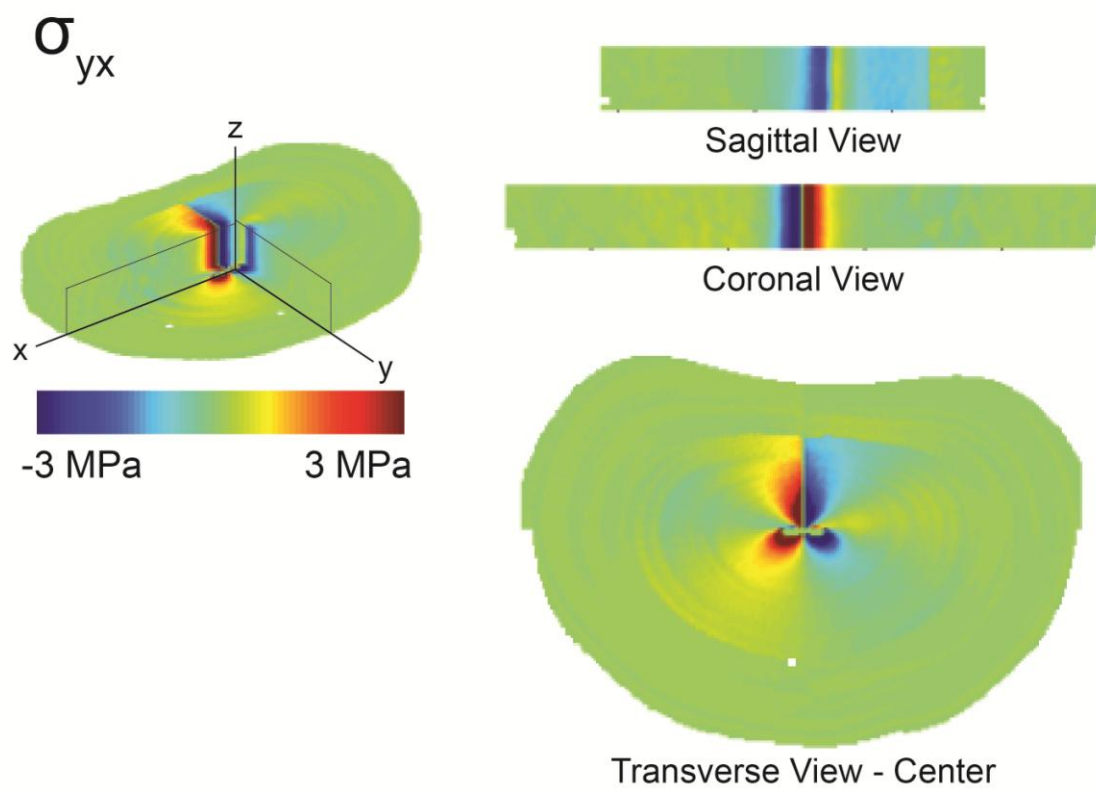
Figure A.4: Isometric, sagittal (*y-z* plane), coronal plane (*x-z*), and transverse (*x-y*) plane views of σ_{xy} for a representative disc.

Figure A.5 Isometric, sagittal (*y-z* plane), coronal plane (*x-z*), and transverse (*x-y*) plane views of σ_{xz} for a representative disc.

Figure A.6: Isometric, sagittal (*y-z* plane), coronal plane (*x-z*), and transverse (*x-y*) plane views of σ_{yx} for a representative disc.
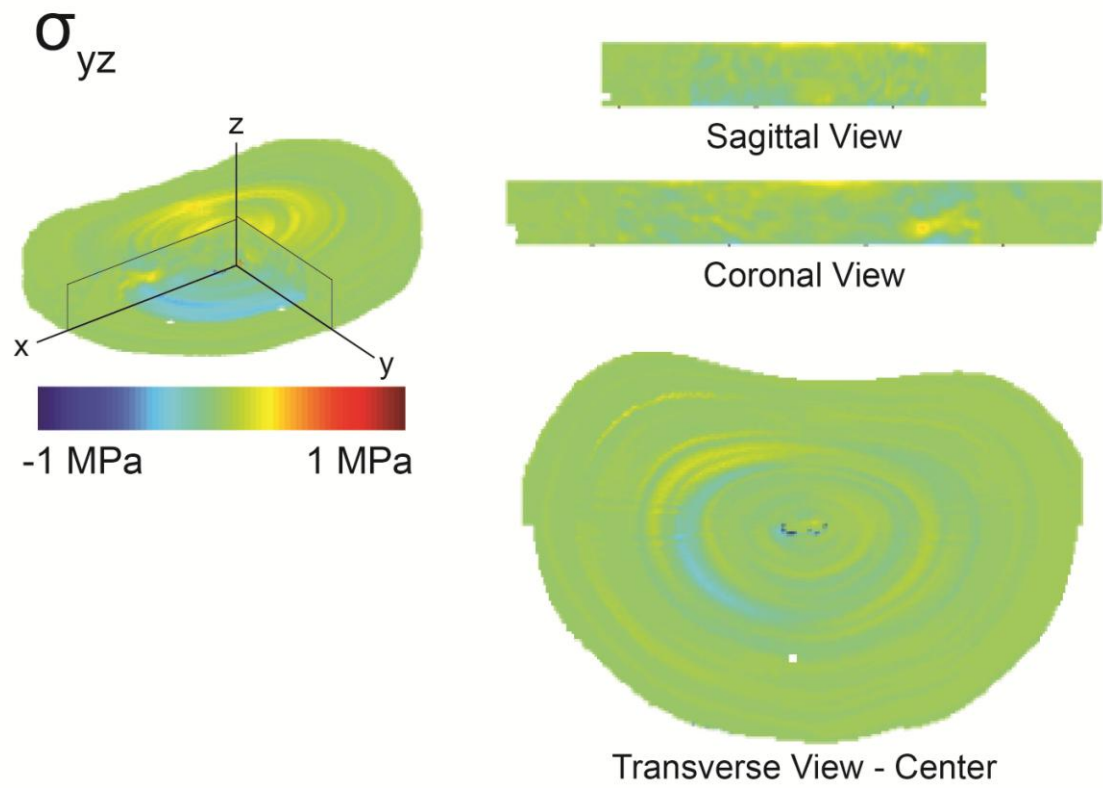
Figure A.7: Isometric, sagittal (*y-z* plane), coronal plane (*x-z*), and transverse (*x-y*) plane views of σ_{yz} for a representative disc.
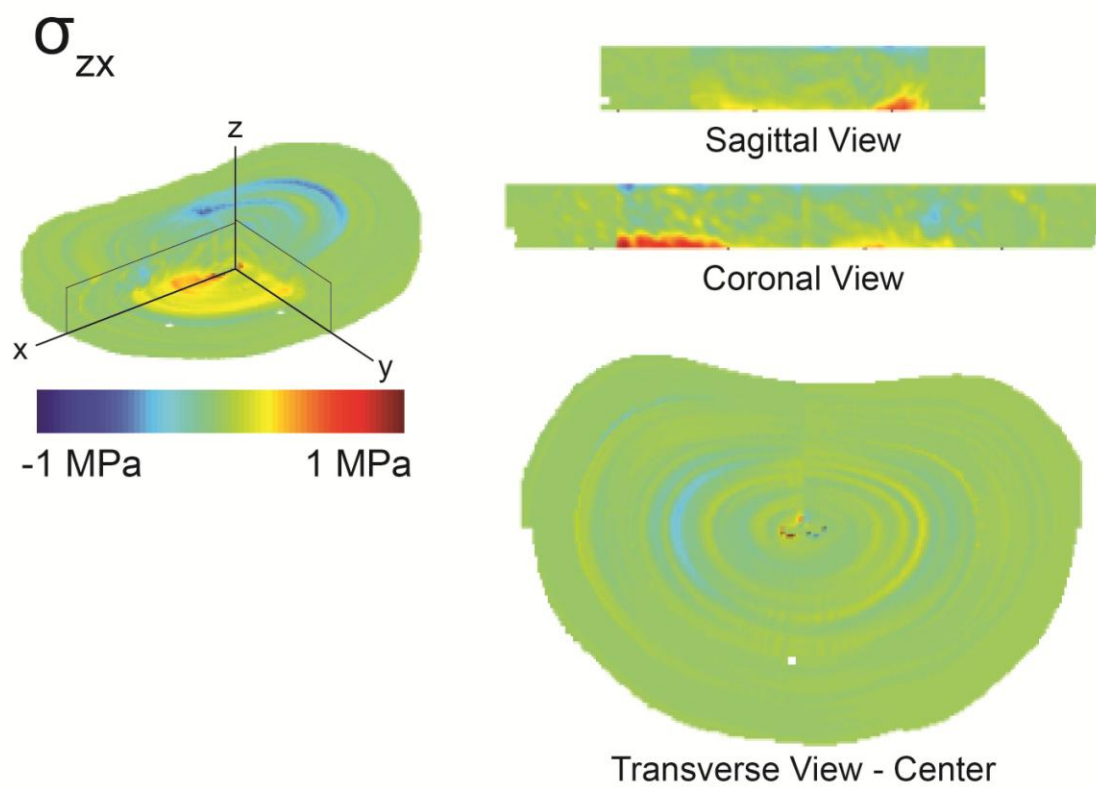
Figure A.8: Isometric, sagittal (*y-z* plane), coronal plane (*x-z*), and transverse (*x-y*) plane views of σ_{zx} for a representative disc.
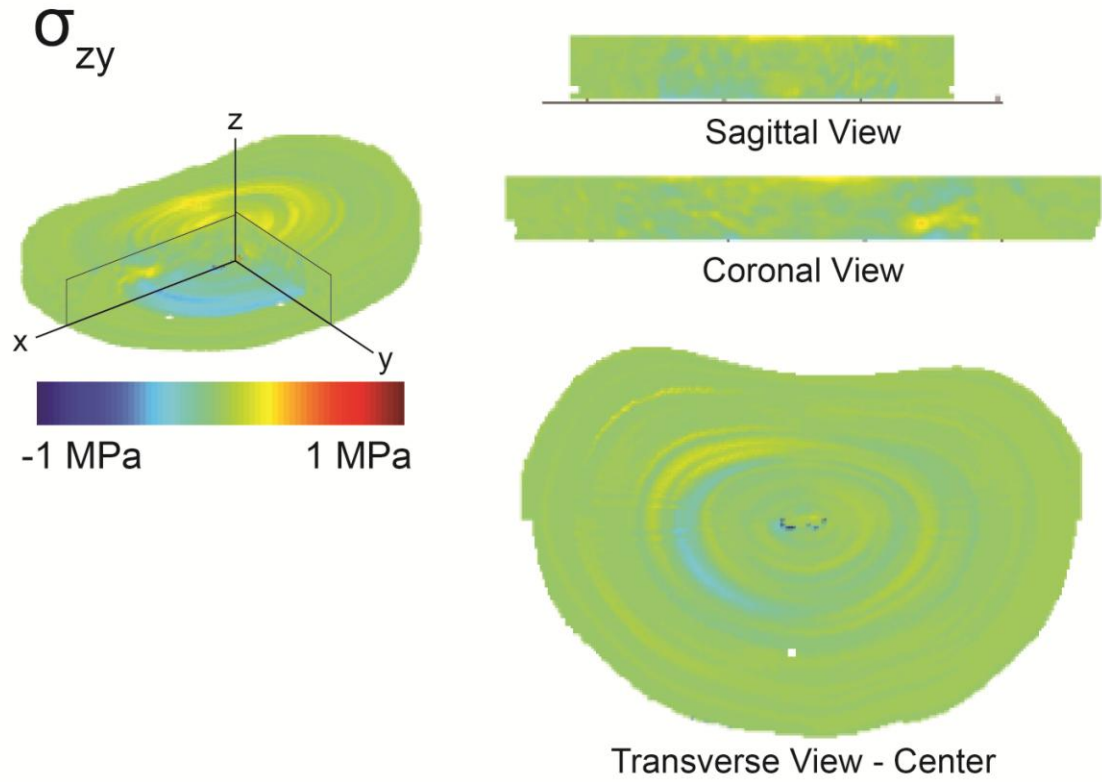
Figure A.9: Isometric, sagittal (*y-z* plane), coronal plane (*x-z*), and transverse (*x-y*) plane views of σ_{zy} for a representative disc.

VITA

VITA

Kent Butz received his BSME from Purdue University in 2006. In the following years he continued postgraduate studies at Purdue under the guidance of Prof. Eric A. Nauman, receiving his MSME in 2008 and is currently pursuing his Doctorate of Philosophy. His research has sought to characterize joint and soft tissue mechanics through the utilization of computational modeling techniques. As a master's student, he developed finite element models of joint and bone stresses experienced in the hand, and performed research into the development of a novel composite material aimed at reducing wear rates of finger joint replacements. His doctoral work focused on the creation of noninvasive modeling techniques for soft biomaterials through the integration of MRI-based measures of deformation and composition with numerical analysis methods. He has authored four journal publications, and has been selected for three conference poster presentations.